APPLICATION OF SOME METAL OXIDE NANOPARTICLES FOR THE REMOVAL OF HEAVY METALS FROM WASTEWATER

BY

IGWE PRINCE UCHE

B.Sc. Industrial Chemistry (Uniport), P.G.D. Chemical Engineering (RSUT), M. Tech, Chemical Engineering (RUST) Port Harcourt.

20134936918

A THESIS SUBMITTED TO THE DEPARTMENT OF ENVIRONMENTAL MANAGEMENT OF POSTGRADUATE SCHOOL

FEDERAL UNIVERSITY OF TECHNOLOGY, OWERRI

IN PARTIAL FULFILLMENT OF THE REQUIREMENT FOR THE AWARD OF DOCTOR OF PHILOSOPHY (Ph.D.) IN

ENVIRONMENTAL MANAGEMENT

DECEMBER, 2024

CERTIFICATION

This is to certify that this work " SYNTHESIS, CHARACTERIZATION AND APPLICATION OF SOME METAL OXIDE NANOPARTICLES FOR THE REMOVAL OF HEAVY METALS FROM WASTEWATER" was carried out by **Igwe, Prince Uche (Reg No. 2013493618)** in partial fulfillment for the award of Doctor of Philosophy (PhD) degree in Environmental Management in the department of Environmental Management of the Federal University of Technology, Owerri.

.....
Prof. E.E Oguzie
Supervisor

.....
Date

.....
Prof. A.P Uzoije
Co-supervisor

.....
Date

.....
Dr. (Mrs) T.E. Ebe
Co-supervisor

.....
Date

.....
Dr E.I. Emereibeole
(Head of Department)

.....
Date

.....
Prof. J.O. Njoku
(Dean of SOES)

.....
Date

.....
Prof. J. N. Nwosu
Dean, P.G. School

.....
Date

.....
Prof. F. I. Okpiliya
External Examiner

.....
Date

ii

DEDICATION

This work is dedicated to God almighty for his enablement.

ACKNOWLEDGEMENTS

All praise to God, Lord of creation ,I am very grateful to my supervisors Prof. E.E Oguzie, Prof. A.P Uzoije and Dr. (Mrs) T. E Ebe for their invaluable contributions and directions, without their support and guidance, this journey of PhD study would not have been completed.

My special thanks go to all the lecturers of the department in whom I owe a lot from their lecture notes to academic advise, Prof. Owuama, Prof. Mrs Stella, Prof. Nkwocha, Prof. P.C Njoku, Dr. Emereibeole, Dr. C. C Ejiogu Dr. Jonathan Anyanwu, Dr. Ihejirika, Dr. Umunnakwe, Dr. Amangabara, Dr. (Mrs.) K. Oguzie, Dr. J. J. Nwachukwu and so many others I say a big thank you.

I equally appreciate Prof. Joshua Konne for his advice and guidance on this journey.

I am highly thankful to my wife Florence Igwe and my children, Chinedu, Kelechi and Chibuike for sacrificing their time and enjoyment for my studies.

I am indebted to my parents Mr. and Mrs. Igwe Israel and Roseline who has taught me value and excellence which has enabled me to reach at this point of scholarship in life.

To my friends and colleagues Drs. Enize Edori and Onisogen Edori and also Miss. Yvette O., Mrs. Orjiaku, Mrs. Lilian Bosco and Mr. Ifeanyi, I say may God bless.

TABLE OF CONTENTS

LIST OF TABLES

LIST OF FIGURES

LIST OF PLATES

ABSTRACT

The present work involves the study of the removal of $As^{3+,}$ $Cd^{2+,}$ $Cr^{6+,}$ Ni^{2+} and Pb^{2+} from synthetic wastewater solutions using metal oxide nanoparticles. Laboratory experiments were used to investigate the efficiency of adsorbents in the uptake of heavy metals from industrial wastewater. These include equilibrium tests and kinetic studies. The physical and chemical characterization of the metal oxide nanoparticles was carried out using different analytical techniques such as Scanning Electron Microscopy (SEM), Energy Dispersive Spectroscopy (EDS), X – Ray Diffraction (XRD), X – Ray Fluorescence (XRF), and Fourier Transform Infrared (FT-IR) Spectroscopy. The kinetic study indicated the suitability of the modified nanoparticles for the removal of $As^{3+,}$ $Cd^{2+,}$ $Cr^{6+,}$ Ni^{2+} and Pb^{2+} ions from synthetic wastewater. Column experiments were used to identify the effect of parameters that affect the rate of adsorption such as the effect of contact time, the effect of adsorbent mass, effect of initial solution concentration, and the effect of temperature and evaluated their impact on the efficiency of modified and its control of the metal oxide nanoparticles in the removal of heavy metals from industrial wastewater. The kinetic studies showed that the capacity of the adsorbents for the removal of heavy metals increased with contact time, increased with a greater mass of absorbent, higher solution concentration as well as the solution temperature. The results from the equilibrium studies positively demonstrated that metal oxide nanoparticles synthesized modified and non-modified can be used as an excellent adsorbent for removing heavy metals from wastewater solutions. The equilibrium experiments indicated that the capacities of metal oxide nanoparticles for the uptake of heavy metals increased when the adsorbent mass increased. The results indicated that the maximum removal capacities Q were 67.11, 67.11, 54.05, 55.56 and 84.74 mg/g of modified and its control of the metal oxide nanoparticles for Arsenic, cadmium, chromium nickel and lead respectively. the Langmuir, Freundlich and Temkin isotherm models were used to characterize the experimental data and to assess the adsorption behaviour of modified and its control of the metal oxide nanoparticles for arsenic, cadmium, chromium nickel and lead. The experimental data were slightly better suited to the Langmuir isotherm than the Freundlich isotherm. The value of the correlation coefficients R^2 ranged from 0.93 to 0.99 for the Langmuir isotherm and from 0.90 to 0.99 for the Freundlich isotherm. The results indicate that starch modified metal oxide nano adsorbents showed higher adsorption. Therefore, starch modified nanoparticle or adsorbents should be incorporated in the synthesis of metal oxides used as adsorbents, due to its ability to improve the surface area and enhance greater adsorption of metal ions.

KEYWORDS

Adsorption, Heavy Metals, Synthesis, Isotherms, Kinetics

CHAPTER ONE

INTRODUCTION

1.1 Background Information

Though water has an important part used for the processes of different manufacturing or mining activities, still the wastewater that is released into the environment during the process is associated with contaminants. The treatment of the discharged effluents or wastewater from these processes has not been given the required attention. The producers and the consumers of products from industrial processes are only concerned with the quality of the product without proper understanding or expertise in wastewater treatment. In addition to the non-concern of wastewater treatment by end-users, it is vital for dropping the hazard in the manufacturing processes (Chen, et al., 2010). Nevertheless, the management and controlling of water in production has turned out to be more extremely accepted in the past few years as a notable subject in line for the growing pressure on water resorts and low value feed water, because fresh water is becoming increasingly challenging to be found (Qu et al., 2013; Teh et al., 2014).

Accordingly, industrial products manufacturers are doubling their efforts to reduce the wastewater influence on freshwater resources. This is achieved through the method of treatment of used water before discharge into the environment. Excess of wastewater and absence of clean water drives government and residents to spend more on drinkable water and its rational applications. Water treatment expertise has helped to decrease and totally remove the detrimental effect on the environs, and assist in the maintenance of equilibrium in natural water systems (Isidorov, 1997).

Poisonous heavy metal contamination is very important in environmental and occupational considerations due to the propensity of heavy metals to be integrated into the food chain

(Sikder et al., 2014). Numerous conservative methods such as chemical precipitation, filtration, chemical oxidation or reduction, electrochemical treatment, reverse osmosis, ion exchange and evaporation have been used to remove heavy metals from weak solutions (Das, 2015). Although, these methods regularly are associated with the problem of not being able to remove contaminants to acceptable discharge limits. The main issue connected with these methods involve very high operational cost and the production of other chemicals as by-products, which also might constitute environmental hazard (Wang & Chen, 2014). So, there is a need to search for a cost effective and eco- friendly alternative technique for removal of heavy metals from aqueous environment. The contamination of aquatic environment is one of the most serious worldwide human health threat due to its extremely toxic effects on animals and plants. Various treatment technologies such as coagulation and precipitation, adsorption, membrane filtration, ion exchange, reverse osmosis and phytoremediation, have been developed for the removal of toxic metals and other deleterious components or chemicals from drinking water and wastewater.

Sources of water pollution are both natural and man-made sources. Hence, the type of treatment suitable for wastewater becomes a very important issue that is associated with the types of wastewaters generated. Generally, wastewater is classified according to the domination of either organic based compounds or inorganic material it contains. The presence of toxic metals in the environment play a very negative role which is very unsafe for the environment and can cause death for man and animals. Manufacturing and prospecting industries are the most notable sources of anthropogenic poisonous metals. Generally, anthropogenic input sources of toxic heavy metals include the fuel industry, machinery, traffic, ferrous metallurgy, non-ferrous metallurgy, mining industry, chemical industry, electroplating.

1.2 Problem Statement

The contamination of wastewater by heavy metals is of great importance to the world, because they are known to persist in the environment due to their non-degradable nature, Heavy metals have the tendency to accumulate in the human system (EPA, 2016). Examples of these heavy metals include cadmium, iron, chromium, zinc and arsenic. These heavy metals may affect aquatic organisms due to their toxic nature and accumulation in the food chain process and pose harmful effect to man and his environment (Sabri & Tuzen, 2008).

Several technologies have been used to treat metal containing aqueous solution for the last few decades (Wang and Chen, 2009).

New and effective technology for the treatment of wastewater is an essential area of research in this period of social, economic and industrial development (Kulkarni & Kaware, 2013). Nano technology is one of such new methods that helps in the purification of wastewater. Nanomaterials are effective in removing contaminants even at low levels of concentration and usually produce low level of wastewater after treatment. This will eventually reduce the level of challenges experienced with the use of other conventional methods.

1.3 Objectives of the Study

The main objective of this work is to synthesize and characterize some metals oxide (ZnO, Fe_3O_4, MnO) nanoparticles for the removal of heavy metals in wastewater.

The specific objectives are.

i. To synthesize ZnO, MnO and Fe_3O_4 nanoparticles using sol-Gel (Starch coated) techniques.
ii. To Characterize the metal oxides nanoparticles using XRD, SEM, X-RF and FT-IR.
iii. To assess the heavy metal removal abilities of the metal oxides using column packed bed.

iv. To determine the effect of process variables like, Adsorbent dose, Concentration of effluent and time on the heavy metal removal efficiency.
v. To apply a mathematical model for approximation of removal efficiency under specific conditions with time.

1.4 Justification

During production processes in the industries, effluents are being released into the water bodies. These effluents are sources or population to the water bodies. Heavy metals are also present in the effluents discharged into the water bodies by industries during production processes and some of these heavy metals are toxic. These heavy metals can cause serious health effects with varied symptoms depending on the nature and quantity that are exposed to humans through contacts and injections. These heavy metals move through the environment through different pathways into the food chains and could accumulate in the body of plants, animals and even humans that make use of the water body. The presence of heavy metals in the water above the required limit is detrimental to human health. Hence the purpose of this study is to synthesize and characterize metal oxides of nanoparticles, which will be used in adsorption studies on the removal of heavy metals from wastewater. This will help to provide a more convenient and assessable method of wastewater treatment.

1.5 Scope of the Study

The study involved the synthesis of nanoparticles of metal oxides of Zn^{2+}, Fe^{3+} and Mn^{2+}. The synthesized nanoparticles were characterized using SEM, XRD, X-RF and FT-IR methods. The synthesized particles were used for adsorption studies on the removal of heavy metals (As, Cd, Cr, Ni, and Pb) in wastewater. Column bed techniques containing the adsorbent were used. The rate of removal of the metals from the wastewater were further determined by measuring the concentrations of the metals in the wastewater before and after treatment using atomic absorption spectrophotometer (AAS). The removal rate was then determined based on the initial and final results.

CHAPTER TWO

LITERATURE REVIEW

2.1 Types of Nanoparticles

2.1.1 Inorganic Nanoparticles

Nowadays in the investigation of new material science Inorganic nanoparticle has stayed advanced the role placed upon their characteristic physical properties and mainly in biotechnology. Based upon these two factors of inorganic nanoparticles they have certain physical properties that mainly include size dependent optical, magnetic, electronic, and catalytic properties. Bio related application are involved for the preparation of these interesting nanoparticles like iron oxides, gold, silver, silica, quantum dots etc (Wang & Wang, 2007). Novel physical properties mainly related because of their size approaches nanometer scale dimension (Mark et al., 2007).

2.1.2 Polymeric Nanoparticles

Polymeric nanoparticle is also a type of nanoparticle. In the recent year polymeric nanoparticle has a great advance in the field of research. The spreading of preformed polymers and the polymerization of monomers are two strong schemes chiefly involved for research (Prasad et al., 2008). 10 -1000nm is the range of size involved with solid particles (Nagavarma et al., 2012).

2.1.3 Solid Lipid Nanoparticles

This is aimed at leading the drug delivery in 1990`s Solid lipid nanoparticles played an important part. Here occur definite substitute carrier methods to emulsions, liposomes and polymeric nanoparticles as a colloidal Carrier system (Abhilash, 2010).

2.1.4 Liposomes

Liposomes are one of the methods based upon the different types of nanoparticles. Structure of liposomes consists of one or more phospholipid bilayers, and they are sphere-shaped vesicles to carry compound of interest. Today liposomes have been useful in the field of reagent and tool in various scientific disciplines. Since many features involved in liposome, they made their own way in the market. Cosmetic and pharmaceutical industries numerous molecules act as a carrier, and in the field of Food and farming industries liposomes involved in encapsulation to grow delivery system that can entrap unstable compounds (Abolfazl et al., 2013).

2.1.5 Nanocrystal

A nanocrystal is a type based upon material particle having at least one dimension smaller than 100 nanometer's and mainly composed of atoms in either a single or poly-crystalline arrangement. Nanocrystals are aggregates of around hundreds or thousands of molecules that combine in a crystalline form, composed of pure drug with only a thin coating comprised of surfactant or combination of surfactants.

2.1.6 Nanotube

A nanotube is a nanometer scale tube like structure. Nanotubes are members of the fullerene structural family. Their name is derived from their long, hollow structure with the walls formed by one-atom-thick sheets of carbon called graphene. These sheets are rolled at specific and discrete ("chiral") angles and the combination of the rolling angle and radius decides the nanotube properties; for example, whether the individual nanotube shell is a metal or semiconductor. Nanotubes are categorized as single-walled nanotubes (SWNTs) and multi-walled nanotubes.

2.1.7 Dendrimers

Dendrimers arise from two Greek words: Dendron meaning tree and Mero's meaning part.

Structure of dendrimers has a well-defined size, shape and defined molecular weight and also Dendrimers are hyper-branched, globular, monodisperse, three dimensional nanoscales synthetic Polymers. Molecular chemistry and polymer chemistry both exhibit well-defined characteristics features of Dendrites (Anirudha et al., 2012).

2.2 Nanoparticle Synthesis- Physical and Chemical Methods

Sol-gel technique: In Sol-gel technique discrete particles are integrated network precursor involved in chemical solution that mainly used for the fabrication of metal oxides hence it is a chemical technique. The precursor sol can be either deposited on the substrate to form a film or used to synthesize powders.

2.2.1 Solvothermal Synthesis

In Solvothermal synthesis process the polar solvents are involved in different condition like at temperatures above their boiling points and in the condition of under pressure at versatile low temperature. Hence the reaction does not involve in lower temperature because the solubility of reaction get significantly increases in Solvothermal condition.

2.2.2 Chemical Reduction

Sodium borohydride, hydrazine hydrate and sodium citrate are some of the commonly used reducing agents in which the ionic salts get involved in reduction process by an appropriate medium in the presence of surfactant were involved using reducing agents are used.

2.3 Characterization of Nanoparticles

The following techniques SEM, TEM, XRD, FTIR, EXD, Purification and its application. There are basic steps involved in the biosynthesis of nanoparticles (Kavitha et al., 2013; Jitendra et al., 2014).

2.3.1 UV-Visible Absorption Spectroscopy

Absorbance spectroscopy is used to determine the optical properties of a solution. A Light is sent through the sample solution and the amount of absorbed light is measured. When the wavelength is varied, and the absorbance is measured at each wavelength. The absorbance can be used to measure the concentration of a solution by using Beer-Lamberts Law. The optical measurement of UV-visible spectrophotometer has different absorbance peak like 410nm when treated with the Nerium Obander plant extract after addition of aqueous 1mM Silver nitrate solution (Sing et al., 2006). In case of *Azadirachta indica gel* synthesized with Iron nanoparticles by the indication of suitable surface Plasmon resonance with high band intensities and peaks was found through UV-visible spectroscopy at the range of 216265 nm.

2.3.2 X-ray Diffraction (X-RD) Analysis

X-ray diffraction is a conventional technique for determination of crystallographic structure and morphology. There is increase or decrease in intensity with the amount of constituent.

This Technique is used to establish the metallic nature of particles gives information on translational symmetry size and shape of the unit cell from peak positions and information on electron density inside the unit cell, namely where the atoms are located from peak intensities.

XRD patterns were calculated using X per Rota flex diffraction meter using Cu K radiation and =1.5406 Å. Crystallite size is calculated using Scherrer equation CS= K/ cos

Where CS is the crystallite size Constant [K] = 0.94 is the full width at half maximum [FWHM] Full width at half maximum in radius [ ]?

= FWHM x /180

= 1.5406 x 10^{-10}, Cos

= Bragg angle. Xray diffraction analysis with various nanoparticles has been studied by various research workers to find the high crystallinity of the prepared sample.

2.3.3 Fourier Transform Infrared [FTIR] Spectroscopy

Measures infrared intensity vs. wavelength of light, it is used to determine the nature of associated functional groups and structural features of biological extracts with nanoparticles. The calculated spectra clearly reflect the well-known dependence of nanoparticle optical properties. The green synthesized silver nanoparticle by employing various leaf extract was analysed using Fourier Transform Infrared [FTIR] Spectroscopy showed characteristic peaks. (Amudha et al., 2014).

2.3.4 Microscopic Techniques

These techniques namely SEM and TEM Mainly used for morphological studies of nanoparticles. Many researchers used these techniques to show that the synthesized nanoparticles were more or less uniform in size and shape (Shobha et al., 2014).

2.3.5 Transmission Electron Microscopy (TEM)

Transmission electron microscopy is a microscopy technique in which a beam of electrons is transmitted through an ultra-thin specimen, interacting with the specimen as it passes through. An image is formed from the interaction of the electrons transmitted through the specimen; the image is magnified and focused onto an imaging device, such as a fluorescent screen, on a layer of photographic film, or to be detected by a sensor such as a CCD camera.

TEM forms a major analysis method in a range of scientific fields, in both physical and biological sciences. TEMs find application in cancer research, virology, materials science as well as pollution, nanotechnology, and semiconductor research.

2.3.6 Scanning Electron Microscope

The characterization of Scanning electron microscope analysis is employed to determine the size, shape & morphologies of formed nanoparticle SEM gives high resolution images of the surface of a sample is desired. The scanning electron microscope works as same principle as an optical microscope, but it

Shaoyou et al., (2014), used a simple solid-state procedure to produce Ca with a low charge mass fixed TiO_2 (Ca-TiO_2) mesoporous nanomaterials with which has very high surface area. They examined the structural properties of the synthesized nanoparticles. The nanoparticles were characterized using different techniques such as X-ray diffraction (XRD), small angle X-ray scattering (SAXS), scanning electron microscopy (SEM), energy dispersive spectroscopy (EDS), N_2 absorption-desorption, ultraviolet visible light spectroscopy (UV-Vis) and infrared spectrum (IR). The results indicated that the surface area of the prepared materials was 101.4m^2/g and the spherical nano size was 9~16 nm. The structure of anatase TiO_2, and the doped Ca^{2+} ion remained amalgamated into the matrix or located on an interstitial framework position of TiO_2 by gradually changing the quantities of calcium. Remarkably, the IR showed vibrational peaks at ~1630cm^{-1}which corresponded to red shift of -OH bond arising due to the effect of the increased quantity of the doped calcium and the adsorption capability of thiophene. The Ca-TiO_2 nanoparticle was observed to show more excellent photocatalytic properties than the non-doped titanium.

2.4 Adsorption Studies of Cadmium

Al-Saad et al., (2012) observed that as a result of the very tiny or minute size of nanoparticles, it has very large surface area, therefore, their sorption (absorption or adsorption) and reaction with different heavy metals is very high. The sorption characteristics of iron oxide (α-Fe_2O_3) nanoparticles and its application to decontaminate water from the aluminum (Al III), arsenic (As III), cadmium (Cd II), cobalt (Cd II), copper (Cu II), and nickel (Ni II) was examined. A static experiment was conducted where water solutions of the metal ions were readily prepared. The adsorption characteristics of the iron oxide nanoparticles to the metal ions were examined at different physical and chemical conditions such as contact time, pH, temperature, dosage of α-Fe_2O_3 and the concentration of the metal. A known volume of 10 mL aqueous solutions which were previously contaminated with the individual metal were prepared in the laboratory artificially and treated with the iron oxide nanoparticles. The rate of removal of the metals was achieved by variation of one parameter at each time, while others remain fixed. The fixed conditions were concentration of the adsorbate (1 ppm), adsorbent dosage (0.35 g), contact time (30 minutes), temperature (21.1^{o}C and pH (7). The results showed highest percentage removal for all the examined metals were achieved within an interval of 5 minutes. For metals of Cu (II) and As (II), 95% removal was achieved within the 5-minute time interval, while 35% and 65% removal were achieved for the other metals. All the metals were removed more efficiently at increasing values of pH except those of Al metal whose maximum percentage removal was achieved at a pH of 5 and thereafter remained constant, but further increase lead to a decrease in removal efficiency.

A carbon bound nanoparticles was used to examine it adsorption potentials and a narcotic drug tramadol. The adsorption potentials of the nanoparticle were examined by measuring the concentrations of the narcotic tramadol in a spectrophotometer. The kinetics of adsorption was tested using different isotherms and the isotherms were compared. The different isotherms used to explain the adsorption coefficient were Langmuir, Freundlich and Temkin

at a temperature of 296 ± 2 K. The Temkin isotherm was able to interpret the adsorption coefficient better than the other isotherms (Mehdi et al., 2013).

The investigation of the combined efficiency of powder activated carbon (PAC) and Fe_3O_4 magnetite nanoparticles (MNPs) on the removal of amoxicillin (AMX) in aqueous mixture was done. The physicochemical characteristics of the combined (composite) nanoparticles (MNPs-PAC) were determined by using scanning electron microscopy, transmission electron microscopy, X-ray diffraction, Brunaeur, Emmett and Teller and vibrating sample magnetometer. The operation conditions or factors for adsorption namely pH, contact time, adsorbent dosage, initial AMX concentration and temperature were examined critically. The synthesized adsorbent had a high surface area of 671.2 m^2 per gramme of the nanoparticle and saturation magnetization was 6.94 emu/g respectively. The equipoise time of the adsorption process was observed within 90 min. it was observed that the kinetics adsorption equilibrium and kinetic models for the absorption of AMX onto MNPs-PAC followed was best explained with the Freundlich and Langmuir isotherms and pseudo-second-order kinetic models. The values calculated for the thermodynamic parameters ($\Delta G°$, $\Delta H°$ and $\Delta S°$) of AMX showed endothermic adsorption pattern which was spontaneous in nature. Finally, the authors concluded that the combined MNPs-PAC nanoparticles have a strong possibility or capacity for the removal of antibiotic from aquatic environment (Kakavandi et al., 2014).

Due to the presence of arsenic in groundwater in some parts of the ecosphere, which may have originated from either natural or human discharges, cause negative health conditions on humans. Groundwater serves a useful source of water for domestic water supply to many people; thus, the pollution of groundwater has a long way to limit its application in the general structural development of any urban community. Due to the toxicological effects of arsenic, different adsorption methods have been applied to remove it from water. The used of absorption methods has been proven to be the most proven method in the removal process of

Arsenic contamination in water. The nature of the adsorbents is a major determinant factor in the removal efficiency of contaminants. The use of nanoparticles and nanostructured composites has proven to be one of the most efficient alternatives in the removal of metals from water. Nanoparticles or composites possess very small size, large surface area, and a relative high ratio of surface area to volume. The absorption efficiency of nanoparticles is based on these characteristics and thus makes them most suitable for wastewater purification processes, since it requires greater efficiency of mater removal. Magnetite nanoparticles of size 9 nm were produced in the laboratory and were found to have a high removal rate, definite adsorption capability when equilibrium was established at 8.25 [mg As/g ads]. The adsorption potentials were investigated using different kinetic models and kinetic examinations. The results obtained was compared with those of commercially available adsorbents and was found the magnetite nanoparticles was very effective in the removal of arsenic from water (Chiavola et al., 2016).

Sadeghi *et al.,* (2017), observed that Nanomaterials have remained one of the widely studied approach for the removal of heavy metal ions and dye from wastewater. The part of nanomaterials as operational adsorbents for discharged effluents or wastewater purification have proven beneficial. New nanocomposite adsorbents are being developed daily in modern years, with the intent to utilize them (due to their effectiveness) as adsorbents in wastewater treatment schemes, since they possess the capabilities to remove contaminants from wastewater. Nanoparticle have been found to be cost-effective and environmentally friendly for water treatment. The positive capacities of nanoparticles in water purification processes are achieved because of the properties of the nanoparticles such as the morphological and physical properties.

The preparation of magnetite materials of combined Fe^{2+} and Fe^{3+} with a combination ratio of (Fe^{2+} / Fe^{3+} = 0.5) was done for the purpose of environmental uses as adsorbents. The

obtained nanoparticles were characterized using different techniques such as X-ray diffraction, transmission and scanning electron microscopy, Fourier transform infrared and Raman spectroscopy, and BET adsorption method. The subsequent magnetite obtained was observed to have wide specific surface area of 100 m^2 $g^{-1}$and the particle size was about 10 nm, which were lesser than those of well-crystallized commercial ones which were valued at 80 nm with a surface area of 6.8 m^2 g^{-1}. The adsorption characteristics of the prepared magnetite nanoparticles were compared to commercially produced equivalents in their capacity to absorb arsenic and copper from wastewater. The equilibration kinetics of the adsorption isotherms were properly explained by the Langmuir and Freundlich isotherms. The highest adsorption capability for the solid phase, achieved for the adsorption of arsenic onto synthetic magnetite (nFe_3O_4) was increased to the value of 69.46% when compared to the value observed for the adsorption of arsenic on the commercial magnetite (cFe_3O_4). The observed results indicated that the iron oxide nanoparticles prepared in the laboratory showed absolute potential for the removal and/or immobilization of trace elements from contaminated water.

A quantity of effective adsorbents has been synthesized by using carbon and oxide-based nanoparticles for improving the adsorption ability and removal capability of harmful contaminants from aqueous media. The selective surface morphological, textural and structural properties of nanoparticles demonstrated the capability and tremendous adsorbent qualities that proved potentially useful in the eradication of a few harmful environmental problems and evils. Numerous oxide and carbon centered nanomaterials remained reported as adsorbents frequently in the literature for the elimination of harmful metal ions such as Ni^{2+}, Cr^{3+}, Cr^{6+} Cu^{2+}, Cd^{2+}, Co^{2+}, Hg^{2+}, Pb^{2+}, As^{3+}, As^{5+}, Th^{4+}, Eu^{3+}, Sr^{2+}, $Zn^{2+}$and U^{6+} from polluted aquatic sources (Gupta et al., 2015). The aim of this study is to evaluate the effect of Fe_3O_4 nanoparticle, stabilized with polyacrylic acid on cadmium removal from the contaminated soils. To investigate the effect of important parameters, including nanoparticle

concentration, pH, contact time, and the ratio of contaminated soil mass to nanofluid volume, several batch tests were performed. The maximum removal rate (100%) of cadmium was obtained in the following conditions: nanofluid concentration = 500 ppm, pH = 6.5, contact time = 24 hr and the ratio of contaminated soil mass (gr) to nanofluid volume (mL) = 1:150. Results of selective sequential extraction tests showed that the distribution of cadmium in different fractions of the soil was carbonates, oxides and hydroxides, residual fraction, exchangeable, and organic matter respectively. The tendency of nanoparticles for removal of Cd^{2+} from the soil fractions was in the order of exchangeable > carbonates > oxides and hydroxides > organic matter > residual (Mohamadiun et al., 2018).

2.4.1 Adsorption Studies of Chromium

Ahmed et al., (2015), synthesized ZnO nanoparticles and applied it on the removal of Cr (VI) ions. Experiments were performed using Batch process to examine the effects of Cr (VI) concentration, pH of solution, adsorbent dose, solution temperature, and variation of the contact time on the elimination effectiveness of Cr (VI). ZnO nanoparticle was synthesized using a simple method of heating polyethylene glycol (PEG). The particle size and characterization of the formed nanomaterial was achieved by FTIR analysis and TEM microscopy determination. The authors observed that the effectiveness of the removal of Cr (VI) by the ZnO nanoparticles decreased with increased concentration of Cr (VI), and pH of solution, while increased adsorbent dosage and increased contact time led to more efficient removal of the chromium compound. The optimal solution temperature that gave the maximum percentage removal of Cr (VI) was 60 ^{o}C.

2.4.2 Adsorption Studies of other Heavy Metals

Taman et al., (2015), investigated the adsorption process performance and was assessed using metal oxide nanoparticles for wastewater treatment containing heavy metals in a laboratory scale reactor. Copper oxide nanoparticles were prepared and fully characterized considering their adsorption properties (surface area and pore size distribution) as well as their chemical structure and morphology. The adsorption of heavy metals, including Fe^{3+} and Cd^{2+} was studied in batch experiments. Various physico-chemical parameters such as pH, initial metal ion concentration, and adsorbent dosage level and equilibrium contact time were studied. The adsorption of Cd^{2+} and Fe^{3+} ions increased with an increase in pH. The optimum solution pH for adsorption of both metals from aqueous solutions was 6. Adsorption was rapid and occurred within the first 20 min for both metals within different solution concentrations (250, 100, 50 and 25 mg/L). The kinetic of Cd^{2+} and Fe^{3+} adsorption onto copper oxide nanoparticles was well fitted by the pseudo-second-order rate equation. The equilibrium adsorption data for Cd^{2+} was best fitted by the Langmuir adsorption isotherm model, but for Fe^{3+} adsorption, it was found that Freundlich adsorption isotherm model is the best model to describe it. The selectivity order of the adsorbent is $Fe^{3+>}Cd^{2+.}$ From these results, it can be concluded that the CuO nanoparticles is a promising adsorbent for the removal of heavy metals from aqueous solutions.

The polluted wastewater using the Fenton's reagent with nano metal oxide has been systematically studied using experimental design technique. Experiments were conducted to examine the effects of pH, amounts of ferrous sulfate ($FeSO_4$), hydrogen peroxide (H_2O_2), temperature and the concentration of nano-metal oxide on the removal of heavy metal ions. A second order kinetic model was adopted to represent the Fenton oxidation of wastewater. The relation between the reaction rate coefficient and Fenton was experimentally established as efficient in the removal of heavy metals. (Anusa et al., 2017).

2.5 Synthesis of Zinc Oxide Nanoparticles

Kumar, (2012), in his research work applied a very simple but effective technique precipitation method to synthesize zinc oxide (ZnO) nano particles using zinc nitrate and potassium hydroxide (KOH) in aqueous solution. The precipitated amalgam was dried, calcined, grinded and characterized by UV-vis spectroscopy, transmission electron microscopy (TEM) and dynamic light scattering (DLS). The ZnO nanoparticles displayed characteristic surface plasmon resonance peak at around 372 nm. Particles-size distribution by dynamic light scattering technique showed that the particles were found in the range of 15-45 nanometer (nm) for the purpose of advance applications. Zinc oxide nanoparticles were effectively synthesized by direct precipitation method in this chemical synthesis using zinc nitrate as primary zinc source and KOH as precipitating agent in aqueous solution. The effects of concentration of the precursor, temperature and time of growth on the structure, and grain size were investigated. The sizes-range of the produced nano ZnO particles was approximately 15-45 nm. The particle size increases with growth temperature and decreases with increasing concentration of the precursors. By summing up successfully designed a simplistic and fast synthesis route to produce ZnO nanoparticles and ended with characterization of ZnO nanoparticles by UV-visible, TEM and DLS analysis.

Jianfeng et al., (2014), further investigated morphology of ZnO prepared by sol-gel technology at different (pH) value. By XRD analysis, ZnO particles were high purity under different pH value. In addition, the particles size of ZnO were minimum and uniform dispersion when the pH value was 8.5, and the mass ratio of polyethylene glycol (PEG) and zinc acetate was 1:2 by TEM analysis. Within the limits of this study, ZnO nanoparticles were prepared via sol-gel method, and dispersed uniformly.

The results of XRD showed that ZnO powder was high purity. And the results of TEM showed that ZnO nanoparticles had different particle size in different pH values. ZnO

nanoparticles were dispersed and uniformity when pH value was 8.5 and the mass ratio of PEG and zinc acetate was 1:2. PEG6000 played an important role.

Zahoora et al., (2019). synthesized ZnO nanoparticles by aqueous solution method, sol-gel method and hydrothermal method. The synthesized particles were characterized by XRD, SEM, EDX and UV. The X-ray diffraction studies reveals that the synthesized ZnO nanoparticles have wurtzite structure, and the particle size varies from 13 to 18 nm. Scanning Electron Microscopic investigation reveals that the surface morphology of ZnO nanoparticle is spherical in hydrothermal process and varies to flower like arrangement in aqueous solution and sol-gel process. The UV-Visible spectrum of the nanoparticles shows a blue shift compared to that of the bulk sample. The diffraction peaks are at 2θ values of 31.68110, 34.35960, 36.17690, 47.48350, 56.52690, 62.81150 and 67.91300 were identified to originate from (100), (002), (101), (102), (110), (103) and (112) planes. Based on the Scherrer equation the average crystallite size of the nanoparticles were observed as 13 nm. The main diffraction peak is observed at 2θ value of 36.17690. The value of (β) observed for ZnO is 0.70730. This peak is identified to originate from (101) planes of the ZnO. All the peaks are indexed and found to be well matched to wurtzite.

Muhammad and Farhat, (2018), This study investigated purification and refining methods for producing a nanometer size zinc oxide (ZnO) from low-grade ZnO commercial powder using low-cost ammonium carbonate solution as a leaching agent. The atomic absorption spectroscopy results show that the concentration of lead, cadmium and iron can be significantly reduced by ammonium carbonate leaching and washing. X-ray diffraction and scanning electron microscope results show that structural properties can improve the degree of the preferential c-axis orientation, grain size, and surface morphology of ZnO by solvent evaporation. All physical and chemical results are of particular significance for the

preparation of purified ZnO for device fabrication in photovoltaic industry, functional ZnO coatings, and polymer nanocomposite applications.

2.6 Synthesis of Magnetite Nanoparticles

Wang et al., (2005) Magnetite (Fe_3O_4) nanoparticles was prepared by oxidation-precipitation method using Monoethanolamine (MEA) as precipitation agent and by modified co-precipitation method using the mixture of isomeric-branched primary alcohol (A1416) and kerosene as stabilizing agent, respectively. X-Ray Diffraction (XRD) patterns and Transmission Electron Microscopy (TEM) images indicate the formation of magnetite with cubic phase consisting of crystalline, near-to-spherical particles with sizes around 10 nm. At high pH values or elevated temperature, the precipitated particles possess larger crystallite sizes. Magnetic diameters are obtained by using Chantrell's equations from the magnetic hysteresis loops. The proportion of spin disorder layer in nano-crystalline diameter decreases with an increase in crystallite size.

Papageorgiou et al., (2006) carried out the synthesis of Fe_3O_4 (magnetite) nanoparticles by chemical co-precipitation method. The structure, morphology and magnetic properties of as-prepared were characterized by X Ray Diffraction (XRD), Scanning Electron Microscope-Energy Dispersive X Ray Spectrometry (SEM-EDS), Transmission Electron Microscope (TEM) and Vibrating Sample Magnetometer (VSM). The result of XRD characterization was indicated Fe_3O_4 as the product. SEM and TEM image of the Fe_3O_4 showed nanoparticles Fe_3O_4 have the mean diameter 5-20 nm. The EDS spectra showed strong peaks of Fe and O. Magnetic characteristic of Fe_3O_4 nanoparticles was indicated super paramagnetic properties. The saturation magnetic was 89.46 emu g-1. Therefore, the nanoparticles Fe_3O_4 is suitable to remove dye in the water by a simple magnetic separation process. The optimum adsorption occurred at initial concentration of procion dye 100 mg L-1, pH solution 6, dosage of Fe_3O_4

0.8 g L-1 and contact time 30 minutes under room temperature with color removal 24.40 % and adsorption capacity was 30.503 mg g-1.

Magnetite nanopowder was synthesized by co-deposition of iron salts in the presence of ethylenediaminetetraacetic acid (EDTA) using sodium hydroxide as a precipitating agent. The iron chloride underwent complex formation reaction with (EDTA) followed by co-precipitation of the iron complex by boiling to produce the magnetite powder. The prepared powders were investigated by high magnification SEM and XRD to identify the particle shape and size of the obtained magnetite nanoparticles and its chemical composition. It was observed that the produced magnetite powder has spherical like particle shape with ~30 nm particle sizes and face centered cubic crystal structure. The magnetic properties of the obtained powder were measured using vibrating sample magnetometry (VSM). It was revealed that the obtained nano magnetite particles have super magnetic character which of saturation magnet. (Daoush, 2017).

Magnetite (Fe_3O_4) nanoparticles have been synthesized from iron sands with both co-precipitation and co-precipitation—ultrasonic irradiation methods. X-ray diffraction (XRD) patterns showed that Fe_3O_4 samples generated by these two synthesis methods are in a single phase with a cubic spinel structure. and investigates the influence of ultrasonic irradiation in the synthesis process including size, morphology, composition and magnetic properties. The morphology of Fe_3O_4 was characterized by a transmission electron microscopy (TEM) instrument. The TEM image of Fe_3O_4 synthesized using the ultrasonic irradiation method showed a reduction of the agglomeration of the Fe_3O_4 particles. Moreover, the TEM images also showed that the primary particles of Fe_3O_4 prepared by the co-precipitation method tend to agglomerate as the particles cluster, with the particle size ranging from 9 to 33 nm. Meanwhile, Fe_3O_4 synthesized using the ultrasonic irradiation method tends to construct a primary particle sized about 25 to 37 nm. The magnetic properties that were characterized by

vibrating sample magnetometer (VSM) measurement showed that Fe_3O_4 exhibited superparamagnetic behavior at room temperature. (Rahmawati et.al., 2017)

The magnetite (Fe_3O_4) nanoparticles were successfully synthesized and annealed under vacuum at different temperature. The Fe_3O_4 nanoparticles prepared via sol-gel assisted method and annealed at 200-400ºC were characterized by Fourier Transformation Infrared Spectroscopy (FTIR), X-ray Diffraction spectra (XRD), Field Emission Scanning Electron Microscope (FESEM) and Atomic Force Microscopy (AFM). The XRD result indicate the presence of Fe_3O_4 nanoparticles, and the Scherer`s Formula calculated the mean particles size in range of 2-25 nm. The FESEM result shows that the morphologies of the particles annealed at 400ºC are more spherical and partially agglomerated, while the EDS result indicates the presence of Fe_3O_4 by showing Fe-O group of elements. AFM analyzed the 3D and roughness of the sample; the Fe_3O_4 nanoparticles have a minimum diameter of 79.04 nm, which agrees with FESEM result. In many cases, the synthesis of Fe_3O_4 nanoparticles using $FeCl_3$ and $FeCl_2$ has not been achieved, according to some literatures, but this research was able to obtain Fe_3O_4 nanoparticles base on the characterization results (Zakiyyu et al., 2019).

Fe_2O_3 nanoparticles of different sizes ranging from 22 to 56nm were synthesized chemically by a modified sol-gel method. Pure alpha phase particles as well as particles with admixture of alpha and gamma phase were obtained and identified by x-ray and Mössbauer measurements. Different size and phase controlling parameters have been identified. The average size of the particles decreases with increased annealing temperature of the gel and decreases with the increase in the concentrations of the (citric acid). The annealing temperature affects the relative fractions of the two phases and consequently the magnetization of the particles. The magnetization of the particles (Ms) and coercively (Hc) increase consistently with the increase in the annealing temperature. For the same relative amount of the two phases, the coercivity (Hc) and the moment of the particles increase with

the decrease in the size of the particles, indicating the role of surface effects in the magnetic behaviour. (Shakeel et al., 2001)

In this study magnetite (Fe_3O_4) nanoparticles were successfully synthesized by sol-gel method with the purpose of removing Cr (VI) from wastewater. The phase structures, morphologies, particle sizes, chemical composition, and magnetic properties of magnetite nanoparticles have been characterized by X-ray diffraction, scanning electron microscopy, energy –dispersive analysis by X-ray spectrometer and vibrating sample magnetometer. Synthesized magnetite nanoparticles demonstrated high capacity of hexavalent chromium adsorption. The maximum adsorption of Cr (VI) by Fe_3O_4 nanoparticles occurred at pH 8.2. The adsorption efficiency of Cr (VI) was explained in terms of Freundlich and Langmuir equations. (Adeleh et al., 2015).

Hydrous Manganese Oxides Nano powders as nano adsorbent (MONs) was synthesized and characterized by X-ray diffraction (XRD), scanning electron microscopy (SEM), and transform infrared spectroscopy (FT-IR). The adsorption of Ni (II) ions from aqueous solution on the MONs was investigated with variations in contact time, pH, initial Ni (II) concentration and adsorbent dosage. The results showed that the adsorption of Ni (II) onto MONs increased within 25 min and reached equilibrium gradually and removal percentage were 83%, 57%, 42% and 35% for 25 ppm, 50 ppm, 75 ppm and 100 ppm Ni (II), respectively, by using 1g/l MONs for 90 min at pH 6. The adsorption behavior of Ni (II) onto MONs was best described by the pseudo-second-order model and Freundlich isotherm. The results also indicated that the type of adsorption involved in this study is physisorption (physical sorption) which usually takes place at low temperature. The results also revealed that MONs was a promising adsorbent for removal of Ni ions from industrial wastewater (Ghaniem et al., *2017*).

MnO_2 nanoparticles were synthesized by co-precipitation method using green chemistry. The size, structure and morphology of MnO_2 nanoparticles were characterized by UV-Visible, X-

Ray diffraction (XRD), FTIR techniques. The average particle size of manganese oxide nanoparticles was calculated from the XRD study. The average particle size of MnO nanoparticles was 25-30 nm. MnO_2 nanoparticles thus synthesized have large number of potential applications in the field of pharmaceutical industries, sensors, piezoelectric crystals, fuel cell electrodes and catalysis. (Kumar et al., 2013).

This work by (Al-Duaij, 2018). investigated the removal of cadmium metal ions from synthetic solutions employing zinc oxide nanoparticles prepared by sol-gel method. The structural characterization of the prepared ZnO powder revealed mesoporous particles with hexagonal wurtzite and 109. $7m2.g^{-1}$ surface area. Closed reactor experiments were accomplished to evaluate kinetics, equilibrium, and thermodynamic parameters of the adsorption process. The adsorption process of the removal of cadmium ions was highly initial concentration dependent. A fast equilibrium was attained to achieve a maximum adsorption capacity and the experimental data suited well Langmuir and Freundlich adsorption models. The kinetics pseudo-second-order rate law was found to be in good agreement with the experimental data of the removal (Al-Duaij, 2018).

Nayar (2019), The harmful content of E –waste poses a threat to human health and environment. Its toxicity mixed with our environment courses harmful effects in health of living things. Materials such as carcinogenic chemicals concentrated acids toxic metals found in E-waste affects in our daily life. E-waste if improperly disposed can leach toxic ions like lead cadmium, chromium, mercury and other harmful substances into soil, surface and groundwater. A representative sample off E-waste was chosen for the removal of some heavy metals using ZnO as a nano adsorbent. In the present study investigated the removal of toxic metals [Pb (II), Cd (II), and Hg (II)] from aqueous e waste sample solution by nano adsorbent zinc oxide (ZnO). The values show that adsorption capacity of toxic metals increases with concentration, contact time and solution of pH and then decreases with dosage of adsorbent

[ZnO]. The equilibrium time was attained after 30 min for cadmium and mercury. Maximum removal percentage was achieved at an adsorbent loading weight of 0.3 mg/l for Cd (II) and 0.25 mg/l for Hg (II). Equilibrium conditions were found to be at pH 4 and 6 for Cd (II) and Hg (II) while the greatest rate of adsorption of Pb (II) ions was observed at the pH = 4, with adsorbent dosage 0.3 mg/l and equilibrium time one hour on ZnO. Adsorption is an effective purification and separation process used in especially wastewater treatment. Freundlich adsorption isotherm model was applied to analyze adsorption data and found to be applicable to these adsorption processes. Experiment was applied for toxic metal ions by Batch adsorption. The adsorption isotherm was determined using Freundlich equation.

We utilized gas-phase diffusion flame synthesis, which has potential for large-scale production of metal oxide nanoparticles, to produce iron oxide nanoparticles (IONPs) with variable oxidation states. The efficacy of these materials in removal of arsenate (As(V) from water was assessed. Two different flame configurations, a diffusion flame (DF) and an inverse diffusion flame (IDF), were employed to synthesize six different IONPs by controlling flame conditions. The IONPs produced in the IDF configuration (IDF-IONPs) had smaller particle diameters (4.8 – 8.2 nm) and larger surface areas (141–213 m2/g) than the IONPs produced in the DF configuration (29 nm, 36 m2/g), which resulted in their higher adsorption capacities. As (V) adsorption capacities of the IDF-IONPs increased when the IONPs were synthesized in more oxidizing conditions. The fully oxidized IDF-IONPs, maghemite (γ-Fe2O3), showed the highest As (V) adsorption capacity, comparable to that of magnetite nanocrystals synthesized by thermal decomposition of iron pentacarbonyl and equivalent to three to four times higher capacity than that of a commonly used goethite-based adsorbent. All IONPs were magnetically responsive, which is of great importance for solid−liquid separation. This study demonstrates that the IONPs synthesized in gas-phase flame, particularly IDF-IONPs, are excellent adsorbents because of their high As (V) sorption capacity, potential for large-scale production, and useful magnetic property (Aamir et al., 2013).

2.7 Adsorption Studies of Arsenic

The application of newly synthesized $Fe_3O_4/TiO_2–SiO_2$ that is modified with zinc (FTSZ) as a sorbent, for the removal of arsenic from contaminated water has been investigated in the present study. SEM, FTIR, XRD, BET, Zeta potential sizer (ξ) analyses are used to determine the sorbent characterization. The effect of the operational parameters such as initial pH, initial concentration, and the contact time were studied. In addition, the equilibrium behavior of FTSZ in As (III) removal was investigated in the temperature range of 20–40 °C. The results showed that the equilibrium data were fitted well with Langmuir than Freundlich isotherm model. The maximum monolayer adsorption capacity estimated by Langmuir isotherm was 24.010 mg g^{-1}. Thermodynamic parameters, ΔH°, ΔS° and ΔG° were also calculated from graphical interpretation of the experimental data. Standard heats of sorption (ΔH°) were found to be endothermic and ΔS° values were calculated to be positive for the sorption of As (III) onto the adsorbent (Sadeghi et al., 2017).

Mixed matrix membranes prepared by varying compositions of Cellulose acetate, acetone and formamide for the synthesis of ultrafiltration/nanofiltration membranes with and without nanoparticles for the removal of arsenic from synthetic solution. Zinc oxide nanoparticles were synthesized by an in situ ultrasonic technique and characterization done using XRD and SEM. In the current study, batch experiments were conducted to characterize the maximum removal efficiency of arsenic by cellulose acetate–ZnO mixed matrix membrane. It was found that 58.77% of arsenic removal was obtained for the feed concentration of 1000 mg/L and pH range 6.8 ± 0.6. The nanoparticle-embedded membranes show higher removal efficiency, high flux and permeation rate than cellulose acetate membranes without embedded nanoparticles (Durthi *et al.,* 2018).

Egirania et al., (2018), This study was intended at providing proof that the presence of synthetic zinc oxide-montmorillonite composite, enhanced the adsorption of arsenite by

ACOR montmorillonite. The batch mode systems were used to test the adsorption of arsenite on zinc oxide-ACOR montmorillonite composite. The experimental data involved the synthesis of zinc oxide-ACOR montmorillonite composite. The presence of zinc oxide coating on ACOR montmorillonite enhanced the adsorption of arsenite in aqueous solution. This was because the zinc oxide coating enhanced reorganization of active sites. The mechanism of the reaction indicated less than one proton coefficient of 0.51, < 1. The intraparticle diffusion with a slope of 13.90 (mgg-1) min0.5 and intercept 250.33, ≠ 0 was controlled by the boundary layer. The mass transfer rates were 1.654^-4 cm-2 hr-1, 5.593^-5 cm-2 hr-1 and 3.345^-5 cm-2 hr-1. There was an enhancement of mass transfer of adsorbate to the external layer of the adsorbent.

Advances in nanoscale science and engineering encourage resolving various recent problems associated with water quality using nano sorbents and nanoparticles resulting from the development of nanotechnology. The resulting products involving nanotechnology helps to decrease the concentration of harmful toxic compounds to tolerable level. This can assist to achieve standard water quality as per health advisories. Present article summarized about the application of Iron Oxide nanoparticles (ION) in water purification by adsorption of heavy metals on its surface. To limit the spread of the heavy metals within water sources, Iron oxide nanoparticles (ION) adsorbents were used as nano adsorbents with the aim of removal of heavy elements namely Fe, Cr ions. Affinity and efficiency of Iron Oxide Nanomaterials (ION) at different sorption factors like pH, contact time, initial concentration of Fe and Cr metal ions, the dosage of ION and temperature were observed. The obtained data showed good linear relationship with a correlation coefficient (R^2) larger than 0.9.

Mercury is one of the persistent pollutants in wastewater; it is becoming a severe environmental and public health problem; this is why nowadays its removal is an obligation. Iron oxide nanoparticles are receiving much attention due to their properties, such as: great

biocompatibility, ease of separation, high relation of surface-area to volume, surface modifiability, reusability, excellent magnetic properties and relative low cost. In this experiment, Fe_3O_4 and γ-Fe_2O_3 nanoparticles were synthesized using iron salts and NaOH as precipitation agents, and Aloe Vera as stabilizing agent; then these nanoparticles were characterized by three different measurements: first, using a Zetasizer Nano ZS for their size estimation, secondly UV−visible spectroscopy which showed the existence of resonance of plasmon at λmax~360 nm, and lastly by Scanning Electron Microscopy (SEM) to determine nanoparticles form. The results of this characterization showed that the obtained Iron oxides nanoparticles have a narrow size distribution (~100nm). Mercury removal of 70% approximately was confirmed by atomic absorption spectroscopy measurements (Zhang et al., 2016).

In the present study, ZnO nanoparticles (NPs) were synthesized in zerumbone solution by a green approach and appraised for their ability to absorb Pb (II) ions from aqueous solution. The formation of as-synthesized NPs was established by X-ray diffraction (XRD), Transmission Electron Microscopy (TEM), and UV–visible studies. The XRD and TEM analyses revealed high purity and wurtzite hexagonal structure of ZnO NPs with a mean size of 10.01 ± 2.6 nm. Batch experiments were performed to investigate the impact of process parameters viz. Pb (II) concentration, pH of solution, adsorbent mass, solution temperature, and contact time variations on the removal efficiency of Pb (II). The adsorption isotherm data provided that the adsorption process was mainly monolayer on ZnO NPs. The adsorption process follows pseudo-second-order reaction kinetic. The maximum removal efficiencies were 93% at pH 5. Thermodynamic parameters such as enthalpy change ($\Delta H0$), free energy change ($\Delta G0$), and entropy change ($\Delta S0$) were calculated; the adsorption process was spontaneous and endothermic. The good efficiency of the as-synthesized NPs makes them

attractive for applications in water treatment, for removal of heavy metals from aqueous system (Azizi et al., 2017).

2.8 Heavy Metals and their Oxidation State

2.8.1 Chromium (Cr)

This transition metal is found at a degree of oxidation from –II to +VI. The most common oxidation levels of Cr are +6, +3 and +2. In nature, Cr is found in the form of complex cubic isomorphic minerals called Spinel. The most stable state of Cr is the

+3 valence state which is common for its existence (Wang et al, 2009). Cr is a rare industrial metal which is grayish white in colour, very hard and has a high resistance to corrosion. An invisible oxide coating on the surface of Cr helps it to maintain brightness. This property allows Cr to become a protective and a decorative coating for other metals such as brass, bronze and steel. Chrome plate is used in the automobile parts such as bumpers, but Cr is applied electrolytically (Peric et al, 2006). Stainless steel is an alloy of iron with typically containing 18% Cr, 8% Ni with or without small amounts of silicon and molybdenum. Chrome steel contains a higher concentration of chromium but no nickel, with possibly small amounts of manganese, carbon, phosphorus, sulphur and silicon depending on the alloy. Chrome steel alloys provide high corrosion resistance and good hardenability (Ozacar & Sengil 2005). Cr^{+3} has not been found with any hazardous effects however, Cr^{+6} is counted as lethal for any dose higher than 3g for adult human body. Cr^{+6} with H_2SO_4 form a powerful oxidizing medium that is utilized as cleaning solutions.

2.8.2 Lead (Pb)

Lead is one of the most common heavy elements. Out of several stable isotopes, it is the most abundant. Lead occurs as Galena (PbS). Early use of lead was in water pipes and pipe joints. Pb is a very heavy, soft, highly malleable, bluish – grey colour metal 49 and contains two oxidation states, +2 and +4. Pb resists corrosion and has a low melting point of 327° C. Solid

and liquid sludge wastes contribute more than half of the Pb contamination into environment, mainly through the landfills. The other major lead pollutant is exhaust fumes of cars which cause atmospheric pollution (Naja & Volesky, 2009).

Lead pollution is typical example of anthropogenic metal pollution. Over 2700 years, lead pollution increased during the industrial age and has risen rapidly since it was added to gasoline fuel of vehicles (Mohan & Pittman, 2006). Worldwide lead production is approx. 3 million tons per year of which 40% is consumed by electrical accumulators and batteries, 20% in alkyl additives in gasoline, 12% in construction, 6% in cable coatings, 5% in ammunition and 17% in the miscellaneous usage. Approximately 20% of total mined lead is lost as wastage in manufacturing processes. Pb is used to make batteries, solders and gasoline octane boosters.

However, due to environmental hazards many countries have stopped lead additive usage in gasoline (Naja & Volesky, 2009). Lead due to its common use in plumbing can be found in tap water; and amount of Pb depends on factors such as pH, softness and standing time of water in the piping system. Pb is toxic to the human nervous system and children are more susceptible to its effects. Lead can go to the central nervous system directly from the intestinal tract by absorption (Abia et al., 2003; Naja & Volesky, 2009). Sources of Pb contamination are Pb containing paint, air, soil, dust, food and drinking water. Pb presence in the body can be measured in the blood levels as micrograms of Pb per decilitre of blood 50 (microgram/dl). More than 10 microgram/dl can cause severe health effects (Cicchella et al, 2008). Due to regulatory control on the use of lead in gasoline, paint and food cans, exposure to lead has declined from the 1980s. Pb can be absorbed by human subjects in the different modes such as inhaling, ingestion, dermal contact or through the placenta. Young children absorb more Pb from ingestion through food compared to adults through the habit of eating clay (pica). Once lead is absorbed in the soft tissues of blood, lung, liver, spleen, kidney or bone marrow, it gets rapidly spread as poison in the body at faster rate as compared in hard tissues of bones

or skeleton where Pb is slow to spread. The biological half-life of Pb in blood is approximately. 16 to 40 days and in bones about 17 to 27 years (EPA, 1990). Inorganic Pb is considered as a general poison and enzyme inhibitor whereas organic lead is more poisonous than inorganic Pb. The usual symptoms are psychological for example, excitement, depression and irritability. Young children can develop mental retardation and brain damage. The most insidious characteristic of Pb is the ability to replace the calcium in the bones and to form a semi-permanent reservoir for long term release after the initial absorption of Pb. This can be measured by blood tests and radiography.

2.9 Treatment Methods for Heavy Metal-Bearing Wastewater

There exist numerous techniques for the removal of heavy metals from wastewater and these include chemical precipitation, ion exchange, adsorption, electrolytic recovery, electro dialysis, solvent extraction, reverse osmosis, membrane separation, ultrafiltration, ozonation, foam floatation, vapor recovery, gamma irradiation, freeze crystallization, and photochemical methods. (Patterson, 1987). Although some of these treatment methods can be successfully used for treating most wastewaters, others are quite limited in use. The application of chemical precipitation to dilute solutions (low concentration) an be difficult unless the addition of flocculating agents such as lime, caustic and sodium carbonate is employed However a bulky sludge is produced, and the disposal constitutes a problem (Thackston et al, 1980). Ion exchange and activated carbon adsorption are quite expensive and require recharge of resin or spent activated carbon as well as the disposal of substantial volume of used regeneration solution.

In addition to the fact that membrane technology is expensive, membranes are susceptible to attack by microorganisms, likewise other methods mentioned require elaborate and considerably hi& operation costs In general, factors to be considered in the choice of a method to be adopted for the treatment of heavy metal-bearing wastewater should include: high rate

of removal, economic feasibility in terms of labor, materials, equipment and energy, applicability to small, intermediate and large scales, low productivity of highly enriched spent materials and capability of reducing heavy metal ion concentration to levels below established regulatory standards. Adsorption process is an effective process and adoption of economic and easily available adsorbents such as iron nanoparticle will make the process a considerably promising option by meeting the criteria stated above. (Das, 2015).

2.9.1 Conventional Methods of Heavy Metals Removal

Several technologies have been used to treat metal containing aqueous solution for the last few decades (Wang & Chen, 2009). Commonly used methods for removing metal ions from aqueous streams include chemical precipitation, lime coagulation, ion exchange, reverse osmosis and solvent extraction. However, these methods proved either inefficient or expensive in case of low concentration (1-100 mg/l) of heavy metals prevailing in the environment and generate huge amount of sludge which are difficult to dispose.

2.9.2 Electro Dialysis

In this process, the ionic components (heavy metals) are separated by semipermeable ion selective membranes. Application of an electrical potential between the two electrodes causes a migration of cations and anions towards respective electrodes. Because of the alternate spacing of cation and anion permeable membranes, cells of concentrated and dilute salts are formed. The disadvantage is the formation of metal hydroxides, which clog the membrane.

2.9.3 Reverse Osmosis

It is a process in which heavy metals are separated by a semi-permeable membrane at a pressure greater than osmotic pressure caused by the dissolved solids in wastewater. The disadvantage of this method is that it is expensive.

2.9.4 Ultra-Filtration

They are pressure driven membrane operations that use porous membranes for the removal of heavy metals. The main disadvantage of this process is the generation of sludge.

2.9.5 Ion-Exchange

In this process, metal ions from dilute solutions are exchanged with ions held by electrostatic forces on the exchange resin. The disadvantages include high cost and partial removal of certain ions.

2.9.6 Chemical Precipitation

Precipitation of metals is achieved by the addition of coagulants such as alum, lime, iron salts and other organic polymers. The large amount of sludge containing toxic compounds produced during the process is the main disadvantage. the demerits in the above-mentioned techniques like incomplete metal removal, high reagent and energy requirements, generation of toxic sludge or other waste products that require careful disposal has led to look for cost effective treatment method that can remove heavy metals from aqueous effluents.

2.10 Adsorption of Heavy Metals

Adsorption was discovered from the 1700's by C.W. Scheele for gases, while Lowitz in the late 1700's discovered adsorption for other media (Zhang, et al., 2011). Now adsorption is a significant phenomenon in many applications. Adsorption on solids is commonly used for purification in water and wastewater, most often by using activated carbon. However, many other adsorbents are being used effectively such as silica gel, treated acid clay, agricultural wastes and metal oxides. For example, Das (2015) used recycled iron to remove metals from aqueous solutions. The triple layer surface complexation model was used to characterize the equilibrium of lead, cadmium, and zinc adsorption by using a recycled iron-bearing material. The experiments were conducted using fixed bed and batch reactor systems. The uptake

capacity of the recycled iron adsorbent was favourable relative to some commercial adsorbents.

Adsorption is one of the major unit operations used for removal of various pollutants from wastewater. The basic feature of a good adsorbent is a large specific surface area. The bigger the surface area, the more molecules are trapped on its surface. Generally, this means that a good adsorbent is very porous. The specific area of an adsorbent is the surface area available for adsorption per gram of the adsorbent. It offers flexibility in terms of selection of contacting devices and adsorbent material depending on the time, space and funds available for treatment of the wastewater. "Adsorption" may be defined as the process of accumulation of any substance giving higher concentration of molecular species on the surface of another substance as compared to that in the bulk. When a solid surface is exposed to a gas or a liquid, molecules from the gas or the solution phase accumulate or concentrate at the surface. The phenomenon of concentration of molecules of a gas or liquid at a solid surface is called adsorption. "Adsorption" is a well-established and powerful technique for treating domestic and industrial effluents.

2.10.1 Type of Adsorptions

Depending on the type of attractions between adsorbate and adsorbent, the adsorption can be divided into two types. Forces of attraction exist between adsorbate and adsorbent. These forces of attraction can be due to Vander Waal forces of attraction which are weak forces or due to chemical bond which are strong forces of attraction. Since type of forces of attraction existing between adsorbate and adsorbent, adsorption can be classified into two types: Physical Adsorption or Chemical Adsorption.

2.10.2 Physical Adsorption

When the force of attraction existing between adsorbate and adsorbent are weak Vander Waal forces of attraction, the process is called Physical Adsorption. Physical Adsorption takes place with formation of multilayer of adsorbate on adsorbent. It has low enthalpy of adsorption i.e. H is 20-40KJ/mol (Habish, 2017). takes place at low temperature below boiling point of adsorbate. As the temperature increases the process of Physisorption decreases.

2.10.3 Characteristics of Physisorption Energetics and Kinetics

Physisorption is an exothermic process however it is characterized by low enthalpy values (20–40 kJ mol-1), due to weak van der Waals forces of attraction. The activation energy for physisorption is also very low and hence it is practically a reversible process.

Effect of temperature: Since physical adsorption is an exothermic process, it occurs more readily at lower temperatures and decreases with increase in temperature. Effect of pressure: In case of physisorption of gases over solids, the extent of adsorption increases with increase in pressure as the volume of the gases decrease during adsorption.

Specificity: Since the van der Waals' forces are universal, a given surface of an adsorbent does not show any preference for an adsorbate in physisorption i.e., it is not specific with respect to adsorbent.

2.10.4 Chemical Adsorption or Chemisorption

When the force of attraction existing between adsorbate and adsorbent are chemical forces of attraction or chemical bond, the process is called Chemical Adsorption or Chemisorption. Chemisorption takes place with formation of unilayer of adsorbate on adsorbent. It has high enthalpy of adsorption. With an increment of temperature, chemisorption first increases and then decreases.

2.10.5 Characteristics of Chemisorption Energetics and Kinetics

Chemisorption is also an exothermic process, and the enthalpy values are higher (80-240 kJ mol-1) (Habish, 2017). As it involves formation of chemical bonds. However, the activation energy for chemisorption is high and occurs slowly. Hence it is also called activated adsorption. It is practically irreversible.

2.10.6 Effect of Temperature

Even though chemical adsorption is an exothermic process, it does not occur slowly at lower temperature due to high kinetic energy barrier. Hence, like most chemical changes, the extent of chemisorption increases with increase in temperature up to certain limit and then after that it starts decreasing. It is also observed that, in some cases, physisorption of a gas adsorbed at low temperature may change into chemisorption at high temperatures. **2.10.7 Effect of Pressure**

The chemisorption is not appreciably affected by small changes in pressure. However, very high pressures are favourable for chemisorption.

2.10.8 High Specificity

Chemisorption is highly specific and occurs only if there is some possibility of chemical bonding between adsorbent and adsorbate.

2.11 Adsorption Kinetics

The kinetic study of adsorption in wastewater plays an important role because it affords important insight into the reaction pathways and into the mechanism of the reaction. Kinetic models have been proposed to explain the mechanism of a solute sorption from aqueous solution onto an adsorbent:

- Pseudo first order kinetic model.
- Pseudo second order kinetic model.

2.11.1 Pseudo-First Order Model

The pseudo first-order kinetic model has been widely used to predict the metal adsorption kinetics. The metal adsorption kinetics following the pseudo first-order model is given by (Ho and McKay, 1999):

$$qt = qe\ (1\text{-}e^{-k1t}) \qquad (2.1)$$

Where k_1(min^{-1}) is the rate constant of the pseudo-first-order adsorption, q_t (mg/g) denotes the amount of adsorption at time t(min) and q_e (mg/g) is the amount of adsorption at equilibrium.

After definite integration by application of the condition's q_t =0 at t= 0 and $q_t = q_t$ at t= t**,** Eq. (13) becomes.

$$log(qe - qt) = log(qe) - \frac{kt}{2.303} \qquad (2.2)$$

By plotting $log\ (q_e - q_t)$ versus t, the adsorption rate can be calculated.

2.11.2 Pseudo-Second Order Model

The adsorption kinetic data can be further analyzed using Ho's pseudo second-order kinetics (Ho & McKay, 1999). This is represented by:

$$\frac{t}{qt} = \frac{1}{K!.q^2e} + \frac{1}{qe}.t \qquad 2.3$$

Integration of Eq. (2.3) and application of the conditions q_t, $=0$ *at* $t = 0$ and $q_t = q_t$ at $t = t$, gives

$\frac{t}{qt}$ vs t should give a straight-line graph of slope 1/qe if equation 2.3 is applied.

Where K_2 (g/ (mg mm)) is the rate constant, K_2 and q_e can be obtained from the intercept and slope.

2.12 Adsorption Isotherm

Adsorption equilibrium is established when the amount of solute being adsorbed onto the adsorbent is equal to the amount being desorbed (Abia et al., 2003). The equilibrium adsorption isotherms were depicted by plotting spud phase concentration (*qe*) against liquid phase concentration *(Ce)* of solute Adsorption isotherm explains the interaction between adsorbate and adsorbent and is critical for design of adsorption process. The Langmuir, Freundlich and Temkin isotherms are the most frequently used models to describe the experimental data of adsorption. In the present work these three isotherms were applied to investigate the adsorption process of Cu (II) and Zn (II) on chitosan at different conditions of process parameters. The adsorption equilibrium study was carried out for metal concentrations varying from 10 to 1 20mgL1.

2.12.1 Langmuir Isotherm Model

The Langmuir adsorption is the best model among the entire isotherm model and it is successfully applied in many adsorption processes. The Langmuir equation is given by:

$$\mathrm{qe} = \frac{q_m K_l C_e}{1 + K_l C_e} \tag{2.4}$$

The linearization of it gives the following form:

$$\frac{C_e}{q_e} = \frac{1}{q_m K_l} + \frac{\mathrm{C_e}}{q_m} \tag{2.5}$$

Where C_e, equilibrium metal concentration, q_m and K_L are the Langmuir constants related to maximum adsorption capacity (mg/g), and the relative energy of adsorption (1/mg), respectively.

2.12.2 Freundlich Isotherm Model

Freundlich isotherm model is one of the most widely used mathematical models which fit the experimental data over a wide range of concentration. This isotherm model is based on heterogeneous surface, distribution of active sites and their energies and enthalpy changes logarithmically.

The Freundlich equation is given by (Singh et al., 2011):

$$qe = K_F C_e^{1/n} \quad (2.6)$$

The logarithmic form of equation:

$$\ln q_e = \ln K_F + \frac{1}{n} \ln C_e \quad (2.7)$$

Where q_e is the amount of metal ion adsorbed after adsorption per specific amount of adsorbent (mg/g), *Ce* is equilibrium concentration (mg/L), K_F and *n* are Freundlich equilibrium constants.

2.12.3 Temkin Isotherm Model

Temkin isotherm contains a factor that clearly taking into the account of adsorbent-adsorbate interactions. The model assumes that heat of adsorption (function of temperature) of all molecules in the layer would decrease linearly rather than logarithmic with coverage on ignoring the extremely low and large value of concentration. Temkin isotherm is given by the following equation (Temkin and Pyzhev, 1940):

$$q_e = \frac{RT}{b} ln\ (aC_e) \quad (2.8)$$

Linear form of this model is given by the following equation:

$$q_e = a + b\ ln\ C_e \quad (2.9)$$

Where q_e is the amount of metal ion adsorbed per specific amount of adsorbent (mg/g), C_e is equilibrium concentration (mg/L), *a* is equilibrium binding constant (g^{-1}) and *b* is related to heat of adsorption (J/ mol) which are Temkin constants.

2.13 Thermodynamic Parameters

K is equilibrium constant that's why its dependence with temperature can be used to predict thermodynamic parameters including change in the free energy *(G°)*, enthalpy (H^0) and entropy *(S°)* associated to the adsorption process and were determined by using following equations (Ozacar & Sengil, 2005):

$$AG° = -RT\ 1n\ K \qquad (2.10)$$

Where K= Langmuir constant

T = absolute temperature (°K)

R = universal gas constant (8.314 $Jmol^{-1}\ K^{-1}$)

$$\text{In } K = \frac{\Delta S^0}{R} - \frac{\Delta H^0}{RT} \qquad (2.11)$$

The plot of in *K* as a function of 1/*T* yields a straight line from which $H^0$and *S°* can be calculated from the slope and intercept, respectively.

CHAPTER THREE

MATERIALS AND METHODS

3.1 Preparation of Materials

3.1.1 Chemicals

The chemicals used for the synthesis of the metal oxide nanoparticles includes ferric chloride (anhydrous.) ($FeCl_2.4H_2O$), Ferrous Chloride (anhydrous) ($FeCl_3.6H_2O$) sodium hydroxide (NaOH), Zinc nitrate (anhydrous) ($Zn\ (NO_3)_2\ .6H_2O$), and manganese chloride (anhydrous) ($MnCl_2.4H_2O$) were of analytical grade. Lead nitrate and iron (III)chloride were products of Avi-chem industries (Mumbai, India) and Lobachemie industries, (Mumbai, India) respectively. All the solutions were prepared with deionized water.

3.1.2 Preparation of Nanoparticles

3.1.3 Preparation of Magnetic Nanoparticle

The preparation was carried in line with work of Zhang et al., (2011) with slight modifications of starch stabilization. 4.4g of $FeCl_3.6H_2O$ and 1.98g of $FeCl_2.4H_2O$ were dissolved in 61ml or de-aerated water to precipitate the iron oxide. The solution was purged for 30mins with nitrogen gas in order to create the inert environment to prevent the oxidation of Fe^{2+} species. 143ml of 0.7M NaOH was also added to the mixture in dropwise with the aid of a syringe to increased the pH to 11 in order to maintain the alkaline environment necessary for magnetite formation. Further influx of Nitrogen gas allowed for additional 20mins before continuous shaking for 1 hour. The mixture was allowed to stand for 24hrs for the particle content to settle. The colour of the mixture change from brown to dark brown and finally to black during the first 7hrs. The ionic equation below summarizes the reaction process

$$2Fe^{3+}_{(aq)} + Fe^{2+}_{(aq)} + 80H^{-}(aq) \longrightarrow 2Fe_3OH_{(s)} + 4H_2O_{(L)} \qquad 3.01$$

The supernatant of the solution was decanted for the magnetization test on the bottom black portion with a bar magnetic. The resultant precipitates (black magnetic iron oxide particles) were allowed to stay in contact with the mother liguor in capped bottles in order to minimize further oxidation of the product.

3.1.4 Preparation of Fe_3OH + SS (Starch Stabilized Magnetite)

The Fe_3OH + SS were prepared by the dissolution of 0.2grams dried starch powder in 100ml of de-aerated deionized water with vigorous shirring until a uniform mixture was obtained. 61ml of the mixture was used as the solvent for the preparation of the starch stabilized magnetite nano-particle. Following the same method described for the magnetic iron oxide particles, the samples were dried at 120°C in the laboratory oven.

3.1.5 Preparation of Manganese Oxide Nanoparticles

The manganese (11) oxide (MnO) nanoparticle were synthesized by a wet chemical method. It involves the precipitation of hydrated manganese (11) chloride $MnCl_24H_2O$ with sodium

hydroxide (NaOH) solutions. 13.21g of $MnCl_2$ dissolved in deionized water and was reacted in 20.0g of NaOH at 1:1 ratio. The $Mn(OH)_2$ was filtered and dried until a golden yellow precipitate appeared. It was dried at 80°C to produce a dark brownish crystal of MnO.

$$MnCl_2 + 2NaOH \rightarrow Mn(OH)_2 + 2NaCl \quad 3.02$$

3.1.6 Preparation of Manganese + SS (Starch Stabilized Magnetite)

The Manganese + SS were prepared by the dissolution of 0.2grams dried starch powder in 100ml of de-aerated water. Thereafter the solution was mixed with already synthesized manganese (11) oxide (MnO) nanoparticle to produces a starched modified MnO nanoparticle.

$$MnO + SS \rightarrow MnO\text{-}SS \quad 3.03$$

3.1.7 Preparation of ZnO Nanoparticles

ZnO nanoparticles were synthesized by a wet chemical method involving the precipitation of zinc nitrate and 0.2mol sodium hydroxide solution followed by overnight drying of the precipitates at 80°C to form Zinc oxide. A wet chemical process involving the dissolution of the reacting precursors of Zinc nitrate ($Zn(NO_3)_2$ and sodium hydroxide (NaOH) into a 100-mil deionized water to precipitate $Zn(OH)_2$ was adopted as shown in equation 3.4. The produced $Zn(OH)_2$ was filtered and dried at 80°C to form white particles of ZnO. Equation of Reaction is expressed as follows;

$$Zn(NO_3). + NaOH \longrightarrow Zn(OH)_2 + NaNO_3 \quad 3.04$$

3.1.8 Production of ZnO Nanoparticle Modified with Starch (ZnO-SS)

0.2grams of starch were weighed and dissolve in 500ml of deionized water. The solution was boiled at 100C, cooled and used in the dissolution of the precursor before reaction the zinc oxide nanoparticle with starch were synthesizes via wet chemical process involving in zinc

hydroxide Zn $(OH)_2$ from the reaction of 0.1 mol of Zinc nitrate and 0.2mol of sodium hydroxide. The supernatant was decanted and followed by overnight drying of the precipitates of 80°C.

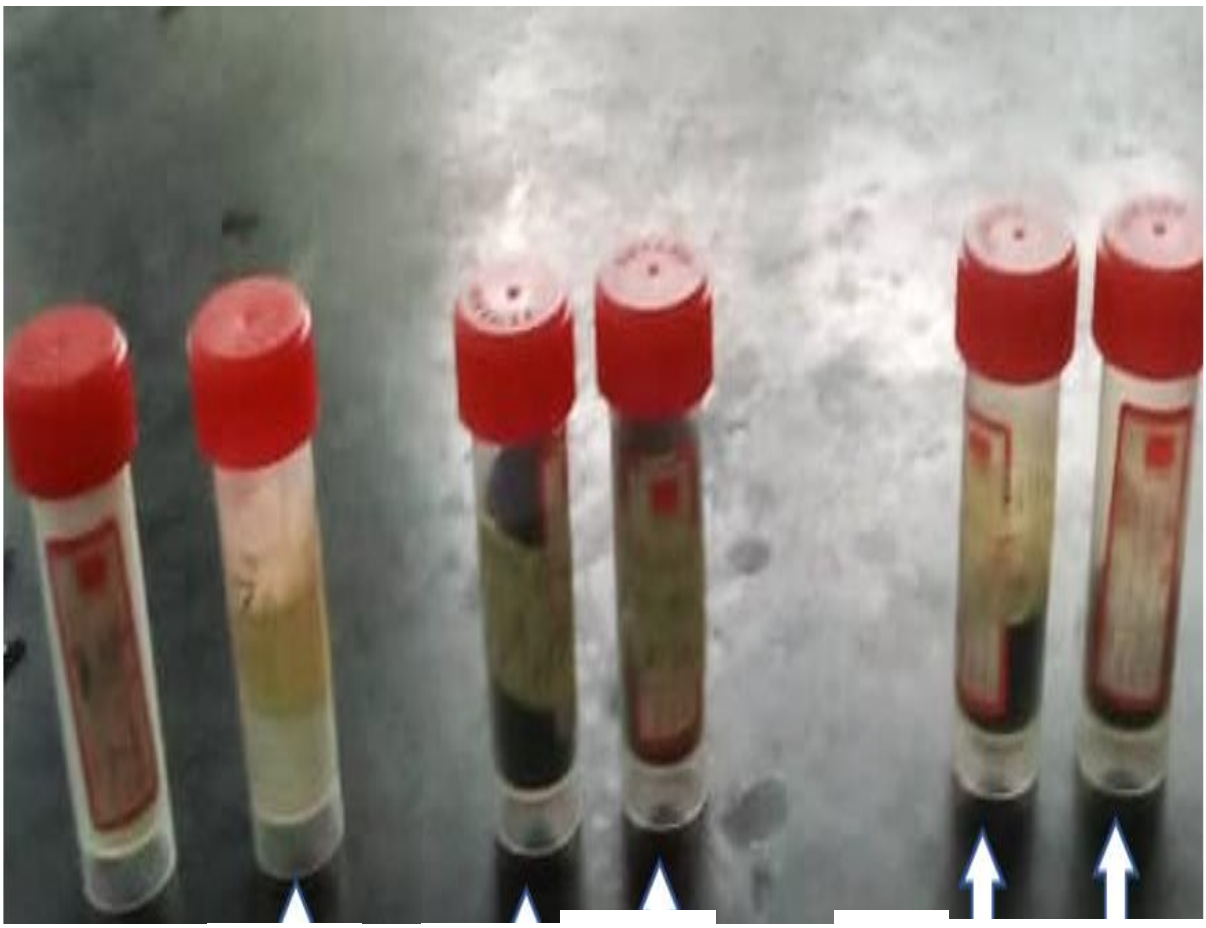

Plate 3.1 Synthesized Nanoparticles of ZnO+SS, ZnO/Fe_3O_4+SS/Fe_3O_4 and MnO+SS, MnO.

3.1.9 Characterization of Nanoparticles.

Characterization is carried out to study different characteristics of the synthesized adsorbent. It is a pertinent exercise when a new material is produced as an adsorbent for the removal of pollutants. The characterization technique provides the elemental composition of the material in weight percent.

. The six synthesized nanoparticles SS-ZnO, SS-Fe_3O_4, SS-MnO and ZnO, Fe_3O_4 & MnO are characterized using;

(a) the Scanning electron microscope, which captures various images by focusing a very high beam of electrons on the surface of the nanoparticles.

(b) X ray Diffraction Spectroscopy. X-ray diffraction is a convenient method for determining the mean size of single-crystal nanoparticles or crystallites in nano crystalline bulk materials (Holzwarth & Gibson, 2011). The grain size calculation was carried out using Scherer's Formula which can be expressed by the following relationship. The (XRD) X-ray diffraction technique was used to detect the specific elements present in the test material. The XRD of the synthesized metal oxide nanoparticles were characterized using (XRD model ARL' XTRA SN: 197492086). The XRD patterns of the Fe3O4-SS and Fe_3O_4, MnO-SS and MnO; and ZnO-SS and ZnO nanoparticles as shown in Figure 4.1,4.2 and 4.3 all Fe_3O_4-SS and Fe_3O_4, MnO-SS and MnO; and ZnO-SS and ZnO reflections were indexed largely to the powder phase.

3.2 Principle of the X-ray Diffractometer

In which the diffraction angle 2θ is the angle between the incident and diffracted X-rays. A typical diffraction spectrum consists of a plot of reflected intensities versus the detected angle 2θ. The 2θ values of the peak depend on the wavelength of the anode material of the X-ray tube. By choosing the right anode and energy of accelerated electrons, a known wavelength and therefore a known energy of X-rays will be generated. Copper X-ray tubes are most used for X-ray diffraction of inorganic materials. For practical applications of X-ray diffraction, we typically want to use x-rays of a single wavelength, i.e., monochromatic radiation to improve experimental results. In general, K radiation is used for analytical work while all other radiation (K, etc.) are removed by means of a nickel filter.

The lattice planes in the simple crystal in Figure 4 are separated by a distance d. The Bragg's law relates the wavelength (Q) of the reflected X-ray, the spacing between the atomic planes (d) and the angle of diffraction (M) as follows: 2d sin M = n Q (1) The angle between the transmitted and diffracted beams will always be equal to 2M. This angle can be obtained readily in experimental situations and the results of X-ray diffraction are therefore given in terms of 2M. It is however very important to remember that the angle that is used in the Bragg's equation must correspond to the angle between the incident radiation and the diffracting plane,

For the first order diffraction, n=1, and knowing M and Q, one can calculate the interplanar spacing d–value for a particular plane.

The first step of X-ray diffraction pattern involves the indexing of XRD peaks. The indexing means assigning the correct Miller indices to each peak of the diffraction pattern. There are three main methods for indexing a diffraction pattern, (i) comparing the measured XRD pattern with the standard data base (JCPDS-cards)

(ii) analytical methods (iii) graphical methods. The intensity of the diffraction signal is usually plotted against the diffraction angle 2θ [°], but d [nm] or 1/d [nm ^{1}] may also be used. The most common wavelength used in XRD is 1.54 A (Cu, K;).

3.3 Preparation of Stock Solution

The 1000mgL^{-1} of stock solutions were prepared by dissolving the specific amount of the respective metal complex salts in the distilled water and the volume of the solution is made up to 1000ml. The details of salt and the amount used are being tabulated in Table 3.1.

Table 3.1 Different Salts and their respective Amount used to prepare 1000mg/l metal stock.

Metal	Complex salt	Formulae	Mol. Weight	Amount used
As	Disodium Arsenate (Heptahydrate)	H_{15} Na_2 As O_{11}	312.01	4.16 (g)
Cd	Cadmium chloride	CdC_{l2}	183.32	1.63g
Cr	Potassium chromate	K_2CrO_4	194.1869	3.73g
Ni	Nickel chloride	$NiCl_2$	129.5994	2.21g
Pb	Lead (11) chloride	$PbCl_2$	278.1	1.348g

3.3.1 Experimental Procedure

Experiments were carried out for the removal of the contaminant ions (As^{2+}, Cd^{2+}, Cr^{2+}, Ni^{2+} and Pb^{2+}) from aqueous solutions using the three nanoparticles of ordinary and starch modified materials respectively as adsorbent materials ($Fe4O_3$: MnO and ZnO ; Fe_4O_3--SS, MnO-SS and ZnO-SS) in a column experiment. The schematic drawing of the experimental set-up is as shown in Figure 3.2

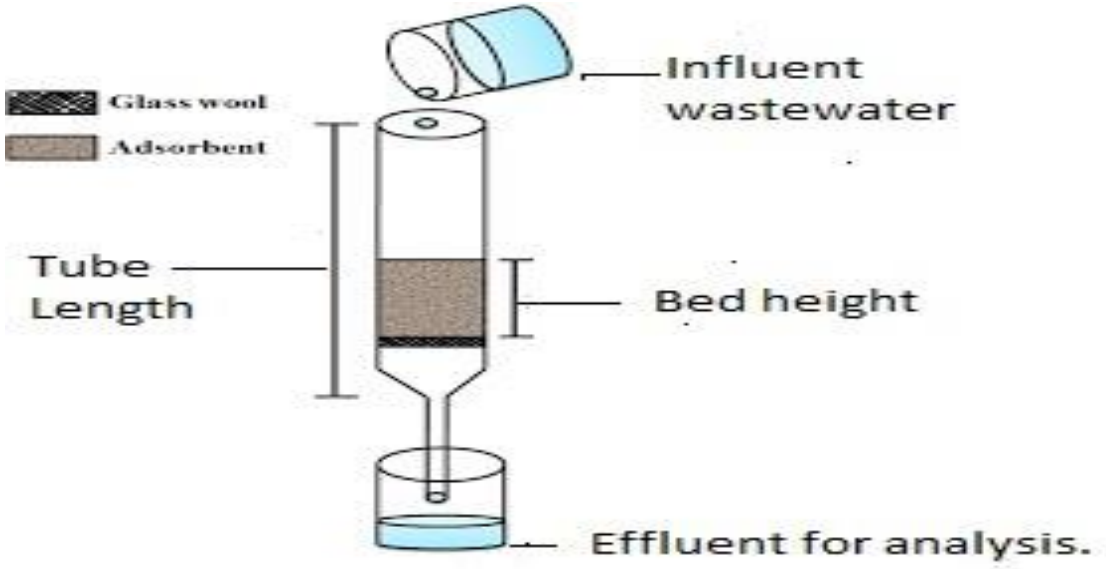

Figure 3.2; A schematic drawing showing the experimental set-up

3.3.2 Adsorption Experiments

The adsorption experiments were performed for the removal of heavy metals from aqueous solutions using the metal based nano-particles (Fe_3O_4; MnO; and ZnO) and starch modified metal based nano-particles (Fe_3O_4-SS MnO-SS and ZnO-SS) as adsorbents. The stock solutions of complex salts of As2+, Cd2+, Cr2+, Ni2+ and Pb2+ ion derivatives were used as adsorbates. The sketch in Figure 3.2 shows the experimental set-up where three glass column of 45.0cm^3 in height and a cross-sectional area of 1.2cm^2 and an inner diameter of 0.6cm3 radius was used as a column. Each of the glass columns was packed with 0.1g of adsorbents (Fe_3O_4; MnO; and ZnO nano-particles respectively) at varied weight between 0.1 to 0.5g. Thereafter, 1000ml of the aqueous solution(adsorbate) of 10ppm initial concentration of different metals was passed through the column in the down flow mode and the entire system was shaken for a while. The aqueous solution was allowed to infiltrate through the packed glass column and effluent collected at the exit end of the column for analysis of As^{3+},

Cd^{2+}, Cr^{6+} Ni^{2+} and Pb^{2+}ions to determine the amount of contaminant ions adsorbed or retain ed by the nanoparticle and the ones exited with the effluent.

To determine the equilibrium parameters, collection and analysis of the metal contaminants were carried out at various initial concentrations (10, 20, 30, 40 and 50mg/l) and adsorbent mass of 0,5g until equilibrium was achieved. Effluent collections were done at time intervals of 5 mins up to 25mins to determine the kinetic parameters.

The same process was replicated for the starch modified metal nano-particles (Fe_4O_3-SS, MnO-SS and ZnO-SS).

3.3.3 Effects of Different Parameters on the Adsorption Processes;

Effects of different parameters on adsorption processes of the metal ions (As^{3+}, Cd^{2+}, Cr^{6+}, Ni^{2+} and Pb^{2+}) on various Nano materials of ordinary Fe_4O_3, MnO and ZnO) and the starch modified Nano- material (Fe_4O_3-SS, MnO-SS and ZnO-SS) were carried out in relation to varying quantities of mass of adsorbent, contact time, initial metal concentrations, temperature of the solution, and pH.

3.3.4 Effects of Initial Concentrations;

The effects of initial concentrations(mg/l) of the metal ions were observed at concentration values of 10, 20, 30, 40, and 50 mg/l and at constant values of pH (4), adsorbent mass (0.5g), contact time(25mins) and temperature(40^oC).

3.3.5 Effects of Adsorbent Mass

Effects of adsorbent mass were carried out at varying weights of 0.1, 0.2, 0.3, 0.4 and 0.5g with constant values of metal ion concentration(50mg/l), contact time (25mins), pH (4), and temperature (40^oC).

3.3.6 Effects of Contact Time

Contact time effects were studied at different time intervals of 5, 10,15, 20 and 25mins) with constant values of 50mg/l, 4, 40^{o}C, 0.5g for, initial metal ion concentration, pH, temperature and adsorbent mass respectively.

3.3.7 Effects of Temperature

Effects of varying temperature at 40, 50, 60, 70 and 80^{o}C were also studied at constant parameter values of 50mg/l 25mins and 0.5g, for pH 4, metal ions concentration and adsorbent mass respectively

3.4 Analysis of Metal Ions.

The concentration of the metal ions remaining in the effluent (liquid phase) at equilibruim was determined using the atomic absorption spectrophotometer (AAS) subsequently the amount of metal ions adsorbed by the nanoparticles at equilibrium was calculated using the following equations. (Babu and Gupta, 2008b; 2009a).

$$q_e = \frac{(Co - Ce)V}{w} \qquad 3.05$$

$$q_e = \frac{(Co - Ce)V}{m} \qquad 3.06$$

Similarly, concentrations of the metal ion contaminants remaining in the effluent collected at time intervals were analyzed with AAS and amounts of metal ion adsorbed onto various adsorbents at each time interval is expressed as follows;

$$q_t = \frac{(C_O - C_t)V}{m} \qquad 3.07$$

Where *m* is the mass of adsorbent (g), *V* is the volume of the solution (ml), *Co* is the initial concentration of metal (mg L^{-1}), C_e is the equilibrium metal concentration (mg L^{-1}) and q_e is the metal quantity adsorbed at equilibrium (mg/g), C_t represents the metal ion concentration in solution after each time interval while q_t is the amount of metal ions adsorbed on the various

nanoparticles (adsorbents). The percent removal of metals from the solution was calculated by the following equation.

$$\% \text{ removal} = \frac{(Co-Ce)}{co} \text{ x}\frac{100}{1} \qquad 3.08$$

Where C_0 (mg/L) is the initial metal ion concentration and C_i (mg/L) is the final metal ion concentration in the solution.

3.5 Analysis of Data

Mathematical based model approach was adopted to analysis the data obtained from various experiments. The models are as follows;

- Isotherm models
- Kinetic models
- Diffusion models
- Thermodynamic models.

3.5.1 Isotherm Models;

Isotherm models were applied to describe and to determine the levels of adsorption of contaminant (metal ions of As^{3+}, Cd^{2+}, Cr^{6+}, Ni^{2+} and Pb^{2+}) from aqueous phase onto solid phase (adsorbents of both ordinary and starch modified Nano materials) at equilibrium

3.5.2 Langmuir Adsorption Isotherm

The Langmuir equation (1918) makes the assumption that the maximum adsorption corresponds to a saturated mono-layer of adsorbate molecules into the adsorbent surface.

Langmuir adsorption isotherm is based on a number of assumptions, including:

(a)Monolayer coverage of the adsorbent surface.

(b) Molecules are adsorbed at stable sites and do not transmigrate over the surface.

(c) All adsorption sites are energetically identical and the energy of adsorption is constant (Almaraz *et al*., 2003; Richardson & Harker, 2002; Tien, 1994, Gunay et al., 2007; Motsi *et al*., 2009). The equilibrium data for heavy metal cations over the different concentration range of metal ions will be fitted with the Langmuir Isotherm (for solid – liquid systems) and use the following equation:

$$\frac{C_e}{q_e} = \frac{1}{K_L q_m} + \frac{C_e}{q_m} \qquad 3.09$$

Where,

q_e is the amount of solute adsorbed per unit mass of adsorbent at equilibrium (mg/g)?

Ce is the residual liquid phase concentration at equilibrium (mg/L), K_L and q_m are Langmuir constants. $K_L$relates to the energy of adsorption which shows the affinity between the Nano materials and the contaminant ions under study and q_m is the maximum monolayer adsorption capacity of the Nanomaterials sorption capacity and sorption energy, respectively. The langumir constants were determined graphically by reading off the gradients and intercepts of the linear curve produced by a plot of $\frac{C_e}{q_e}$ against $C_e$for various adsorption processes.

3.5.3 Freundlich Adsorption Isotherm

The Freundlich adsorption isotherm was developed by Freundlich in 1926.This model is one of the most widely used isotherms. Freundlich adsorption model usually describes the multi-layer adsorption and non-uniformity of heat of adsorption and affinity on heterogeneous surface. It can correlate to the experimental data over a wide range of concentration (Motsi et al., 2009). This isotherm gives an expression surrounding the surface heterogeneity and this model assumes that all adsorption sites are energetically unequal and that the energy of adsorption is irregular (Prasad et al., 2008; Gunay et al., 2007). It is a more realistic

assumption than the Langmuir isotherm. The Freundlich isotherm describes equilibrium on heterogeneous surfaces that are more often seen in natural systems (Inglezakis et al., 2002; Alvarez-Ayuso et al., 2003; Gunay et al., 2007) and can be written as follows:

$$q_e = KC_e^{1/n} \qquad 3.10$$

Where,

q_e is the amount of solute absorbed per unit mass of adsorbent at equilibrium (mg/g)?

Ce is the residual liquid phase concentration at equilibrium (mg/L),

K and n are empirical Freundlich constants that are dependent on experimental conditions.

K is an indicator of adsorption capacity while **n** is related to the adsorption intensity or binding strength. The linear form of the Freundlich adsorption isotherm is expressed as follows:

$$\log q_e = \log K + \frac{1}{n}\log C_e \qquad 3.11$$

Values of K and n were determined by the intercept and gradient respectively of a linear curve produced by $\log q_e$ versus $\log C_e$. As stated by Papageorgiou et al., (2006) values of 1/n <1 indicate heterogeneous adsorbents, while values closer to or equal to 1 indicate a material with relatively homogeneous binding sites due to its porosity.

3.5.4 Temkin Isotherm

Temkin isotherm is based on a factor that unambiguously describes the adsorbent-adsorbate interactions. Temkin and Pyzhey (1940) assumed that the heat of adsorption of all the molecules in the layer would decrease linearly with coverage. The adsorption is characterized by a Standard distribution or biding energies, up to some maximum binding energy (Wasewar et al 2008a). The Temkin model as expressed as:

$$q_e = \left(RT/_b\right) In\ (K_T C_e) \quad 3.12$$

The linear form of Temkin Isotherm is

$$q_e = B_i lnK_T + B_i lnC_e \quad 3.13$$

B_i represents temkin isotherm constant which describes the heat of adsorption. B_i is dependent on temperature values in a manner that the heat of adsorption increases with increase in temperature, K_T is the maximum binding energy of the respective contaminant metal ions on the Nano materials, K_T equally decreases with increase in temperature. The heat of adsorption is related to temperature as follows;

$$B_i = \frac{RT}{b} \quad 3.14$$

where R is the gas constant (8.314 J/mol k), T is the absolute temperature (K)

A plot of q_e versus lnC_e yields a linear curve with B_i as the slope and $B_i lnK_T$ as the intercept.

Note that low B value indicates weak interaction between adsorbate and adsorbent. Temkin isotherm also assumes the heat of adsorption of the molecules in the layer decreases linearly due to increase in surface coverage.

3.6 Kinetic Models

Adsorption kinetic models are governed by the rate of contaminant adsorption onto adsorbents). kinetic models are time dependent while measuring the efficiency of the adsorbents in the course of adsorption process. Hameed et al., (2013) described the kinetic model as the rate controlling processes of chemisorption, physisorption, bulk and intraparticle diffusion which act in series or in parallel with the kinetic process of adsorption.

In this study, pseudo-first-order, pseudo-second-order, Intraparticle diffusion, Ritchie, and sticking probability models were used to determine the best fit kinetic model for adsorption of heavy metals onto the Nano adsorbent of ZnO, MnO Fe_4O_3 and the starch modified versions of the Nano adsorbents (ZnO-SS MnO-SS and Fe_4O_3-SS .The models also described the degree of adsorption mechanisms in which adsorption capacities of various Nano adsorbents, levels of contaminant migration from aqueous(contaminant solution) onto the solid phase(adsorbents) and within the adsorbents, and physical and chemical states of adsorption process were determined.

3.6.1 Pseudo-First-Order Kinetic Model

The Pseudo-First –order kinetic model has been widely used to predict sorption kinetics (Wang et al., 2005). This model is defined by Langergren and Svenska, (1898) as

$$\frac{dq}{dt} = K_1(q_e - q_t) \qquad 3.15$$

Integrating equation 3.15 with respect to the boundary conditions q=0 at t=0 and q=qt at t=t, yields the following equation

$$\log(q_e - q_t) = \log q_e - \frac{K_1}{2.303}t \qquad 3.16$$

Where qe and qt are the amounts of contaminant metal ions adsorbed (mg/g) onto the Nano materials at equilibrium and at time t (minutes) respectively, and k_1 (1/min) is the adsorption rate constant. Values of k_1 and $\ln q_e$ were determined by reading off the slope and intercept respectively of the plot of ln (qe –qt) versus t. according to (Ho and McKay, 1999), the pseudo-first-order equation was found not fit well with the complete range of contact time the model was commonly relevant for the initial stage of the sorption process.

3.6.2 Pseudo-Second- Order Kinetic Model

The pseudo-second- order equation predicts the behavior over the whole range of the adsorption process and appears to be controlled by the chemical sorption mechanism as the rate controlling step. The pseudo-second-order equation based on equilibrium adsorption was expressed by Ho & McKay 1998:

$$\frac{dq}{dt} = k_2[q_e - q_t]^2 \qquad 3.17$$

Separation of variables and integration of equation with respect to boundary conditions of q =0 at t =0 and q =qt at t = t, produced the following equation.

$$\frac{t}{q} = \frac{1}{K_2 {q_e}^2} + \frac{1}{q_e}\,\mathrm{t} \qquad 3.18$$

$$\left(\frac{dq}{dt}\right)_{initial} = K_2 {q_e}^2 \qquad 3.19$$

Equation…can as well be written as

$$h_o = K_2 {q_e}^2 \qquad 3.20$$

Where, $\mathbf{K_2}$ (g/mg h) is the rate constant of second-order adsorption and **ho** (mg/g- min) is the initial rate of sorption. The linear plot of $\frac{t}{q}$ versus **t** gives $\frac{1}{q_e}$ as the slope and $\frac{1}{K_2 {q_e}^2}$ as the intercept.

3.6.3 Elovich Equation

Elovich equation is one of the most frequently used for describing chemisorption (Tseng, 2006; Wu & Tseng, 2006). Elovich equation was given as: (Ozacar and Sengil,2005):

$$\frac{dq}{dt} = \alpha \exp(-\beta dq) \qquad 3.21$$

The integration of the rate equation with the same boundary conditions as the pseudo-first and second-order equations produces a linearized version of Elovich equation as:

$$qt = \frac{1}{\beta}\ln\alpha\beta + \frac{1}{\beta}\ln t \quad 3.22$$

Where, α(mg/g h) is the initial sorption rate and β (g/mg) is related to the extent of surface coverage and activation energy for chemisorption. The parameters $\frac{1}{\beta}$and $\frac{1}{\beta}\ln\alpha\beta$ can be obtained respectively from the slope and intercept of the linear plots of qt versus lnt. The value of $\frac{1}{\beta}$is indicative of the number of sites available for adsorption while the $\frac{1}{\beta}\ln\alpha\beta$ is the adsorption quantity.

3.6.4 Ritchie Model

The model as presented by Ho (2006), predicts the efficiency of adsorbents in adsorbing the contaminants. This is achieved by determining the degree of coverage of contaminants in aqueous phase on the adsorbent. The model is expressed as follows;

$$\frac{d\theta}{dt} = K(1-\theta)^n \quad 3.23$$

θ represents the degree of coverage of the contaminants (adsorbates) in the liquid phase on various solid phases (adsorbents),

K is rate constant, while n is order of reaction. If the first order reaction that is n=1 is assumed, the equation reduces to;

$$-\ln(1-\theta) = K_1 t \quad 3.24$$

after variable separable and integration operations.

With n =2, that is, second order reaction, the equation becomes

$$\frac{\theta}{1-\theta} = K_2 t. \quad 3.25$$

This research work will operate within the realm of n =1 to model the obtained results. In that case a plot of $-\ln(1-\theta)$ vs t was made to produce a linear curve with the rate constant (K_1) as slope

3.6.5 Sticking Probability

This model describes the potentials of contaminants to stick or remain onto the adsorbents during and after adsorption process. The model is expressed as;

$$S^* = (1-\theta)exp - \frac{E_a}{RT} \quad 3.26$$

Where the terms are defined as follows;

S^*=sticking probability or sticking coefficient.

$\theta=\frac{a}{a_e}$; θ represents degree of coverage of the contaminants onto the adsorbents which is expressed as the ratio of the amount of contaminants adsorbed on the solid phase(adsorbent) (a) to that adsorbed on the solid phase at equilibrium (a_e)

E_a=activation energy

R= Ideal gas constant

T= absolute temperature.

Sticking probability could as well be expressed as sticking coefficient which is expressed as the ratio of the contaminant particles likely to bind to the adsorbent surface to the ones hitting the adsorbent surface.

The model describes the various degree of adsorption as follows;

S^* >1 represents no significant adsorption. This expresses the failure of the adsorbing contaminant to stick or remain on the adsorbent.

S^*=1 suggests significant adsorption of contaminant onto the adsorbent. This scenario also expresses linear sticking relationship between the contaminants and the adsorbent and confirms the existence of the mixture of physisorption and chemisorption process (Largitte & pasquier 2016).

S^*<1 gives impression of physiosorption adsorption process.

Sticking probability model could be rearranged as follows

$$\ln(1-\theta)=\ln S^* + \frac{E_a}{RT} \qquad 3.27$$

to make for a curve plot of $\ln(1-\theta)$ Vs $\frac{1}{\mathrm{T}}$, where $\frac{E_a}{R}$ represents the slope while $\ln S^*$ is the intercept. Values of E_a can be obtained from the slope for each adsorption process by multiplying the slope by the Ideal gas constant. The sticking coefficient, S^* was obtained from the intercept.

3.6.6 Thermodynamic Model;

The thermodynamic behavoir of adsorption of the contaminants onto various adsorbents is determined by evaluating the thermodynamic parameters such as Gibbs free energy change (ΔG), enthalpy (ΔH), and entropy (ΔS) using the following equations:

Gibb free energy is directly related to adsorption equilibrium constant $(\mathrm{K_0})$ expressed as;

$$\Delta \mathrm{G^0} = \mathrm{RTlinK_0} \qquad 3.29$$

Where $\mathrm{K_0}$ is the equilibrium constant, R and T are gas constant (8.314J/molK) and absolute temperature respectively, $\mathrm{K_0}$ is expressed as follows;

$$\mathrm{K_0}=\frac{q_e}{C_e} \qquad 3.30$$

Where q_e and C_e representing ratio of amounts of contaminants adsorbed onto the adsorbent and the amount remaining in solution at equilibrium

Values of enthapy of adsorption (ΔH^0) and adsorption enthropy (ΔS^0) were obtained at varying temperature with Van't Hoff equation where;

$$\ln \mathrm{K_0} = \frac{-\Delta \mathrm{H^0}}{\mathrm{RT}} + \frac{\Delta \mathrm{S^0}}{\mathrm{R}} \qquad 3.31$$

At varying temperature values a plot of (lnK_0) versus $\left(\frac{1}{T}\right)$. was made to obtain a linear curve in which the slope and intercept of the curve were read-off to get ΔH^0 and ΔS^0 respectively.

3.6.7 Diffusion Models;

In adsorption process, solute in aqueous solution (liquid phase) gets to the adsorbent (solid phase) through the following rate determinate steps which include; the external mass transfer and intra-particle diffusion.

3.6.8 External Mass Transfer

In the external mass transfer step, that is, transport of solute molecules (contaminants) from liquid phase (solution) to the solid phase(adsorbent), a model known as liquid diffusion model was applied to access the rate of migration of contaminants to the adsorbing body (adsorbent). the equation Is expressed as

$$\ln(1-\alpha) = \mathrm{K_{t1}}\,\mathrm{t} \qquad 3.32$$

Where α is the fractional attainment to equilibrium (FATE) and is expressed as;

$$\propto = \frac{\mathrm{M_\infty}}{\mathrm{M_t}} \qquad 3.33$$

$\mathrm{M_\infty}$ is the contaminant concentration at infinity or equilibrium while $\mathrm{M_t}$ represents the concentration of contaminant at time, t, $\mathrm{K_t}$ describes the adsorption capacity of the adsorbent? high α implies quick attainment of adsorption process to equilibrium. A plot of $\ln(1-\alpha)$ versus t gives a straight curve with $\mathrm{K_{t1}}$ as the slope. if the linear curve deviates from origin, it suggests that the contaminants diffused into the adsorbent through external particle diffusion mechanism, it also implies that diffusion of the contaminant ions through the liquid film boundary surrounding the adsorbent precedes and predominate the intra-particle diffusion.

3.6.9 Intra-particle Diffusion Model

Intra-particle diffusion measures the quantity of contaminant ions diffused within the adsorbent at a specified period of time (q_t). intra-diffusion model model as developed by weber and Morris was applied to predict the rate controlling step and the model is expressed as follows;

$$q_t = K_{t2} t^{0.5} + \mathrm{C} \qquad 3.34$$

Where $\mathrm{K_{t2}}$ is the adsorption capacity of the adsorbent and relates linearly with adsorption equilibrium and the intra-particle diffusion, C is the intercept and represent the boundary layer effect? Studies have shown that high C value implies significant contribution of surface adsorption to the rate determing step (Wasewar et al 2008a, Uzoije et al 2015).

A plot of q_t versus $t^{0.5}$ produces a linear curve with $\mathrm{K_t}$ as slope. If the curve passes through the origin it means that intra-diffusion controls the process. with the curve deviating from the origin, it earns that intra-diffusion is not the only rate determining step.

CHAPTER FOUR

RESULTS AND DISCUSSIONS

4.1 Results

The results of the Characterization of the synthesized nanoparticles (Fe_3O_4+SS, Fe_3O_4/ MnO+SS, MnO/ZnO+SS, ZnO) showing the XRD pattern, surface morphology (SEM) and XRD analysis are presented in Figures 4.1 to 4.8, while the effects of different parameters on the adsorption of metal ions using the nanoparticles are in presented in Figure 4.1 to 4.3.

4.1.1 The Synthesis of Fe_3O_4, MnO and ZnO Nanoparticles

Plate 4.1 showed the powder obtained from Iron, manganese and zinc oxides nanoparticles synthesized with their different precursors. The Magnetite synthesized with starch was labelled as Fe_3O_4+SS; the manganese oxide synthesized with starch labelled as MnO+SS; and the Zinc oxide synthesized with starch labelled as ZnO+SS and the oxides without starch were labelled as Fe_3O_4, MnO and ZnO respectively.

4.1.2 Adsorbents` Characterization

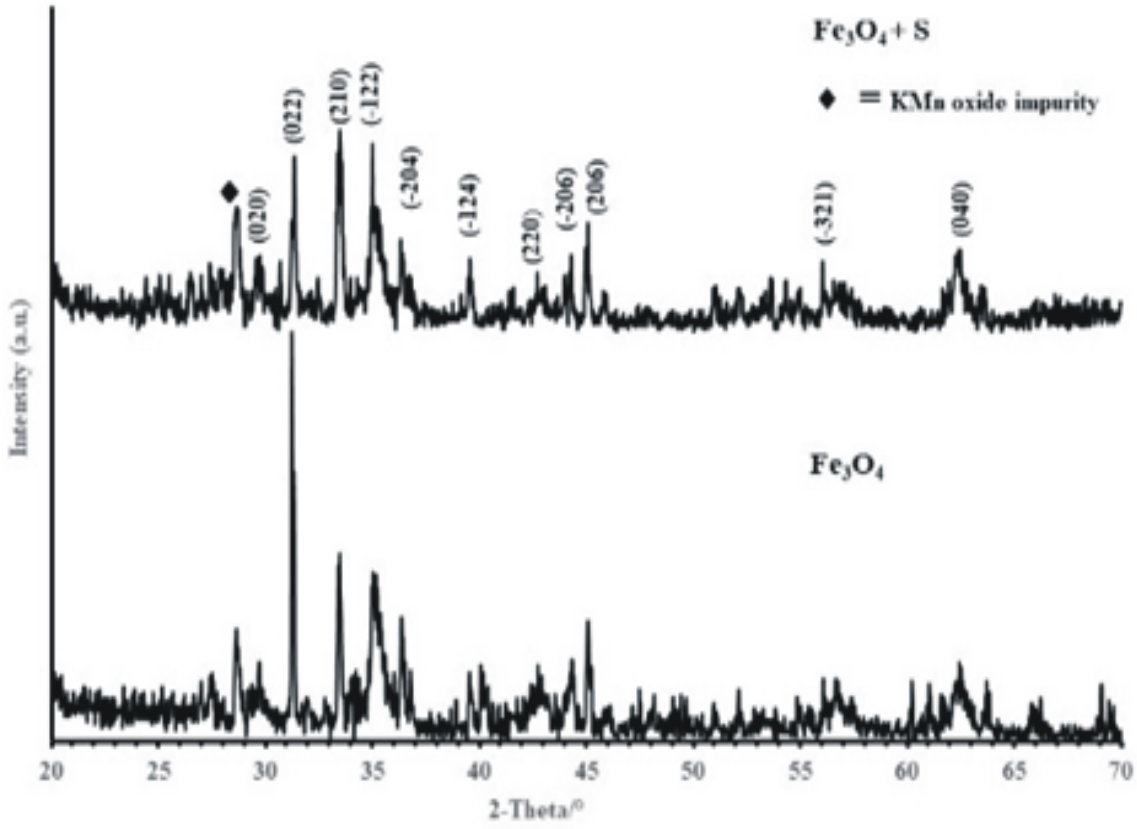

Figure 4.1: The XRD of Magnetite (Fe_3O_4),

The estimated sizes of the samples from sherrer`s formula in equation 4.1 was given as 27.259 and 20.420. These results agreed with the boarder background for $Fe_3O_4$, nano-particles signifying smaller sized materials as compared to the $Fe_3O_4$+s Boarder peaks gives smaller particle sizes according to the sherrer`s particle size,

$$S = k\lambda/\beta \cos\theta \qquad 4.1$$

Where S is the mean particle size, λ is KαI radiation and β is full width at half maximum (FWHM), a property of peak sizes. From the above relation the larger the β, the smaller then S. The XRD patterns also indicated the presence of fewer impurities of KMn oxide. The structural characterization of the synthesized Magnetite, nanoparticles determined by X-ray powder diffractometer (ARL`XTRA SN: 197492086), showed the reflections of Fe_3O_4+SS and Fe_3O_4 respectively with indexed peaks the highest peak with intensity (022).

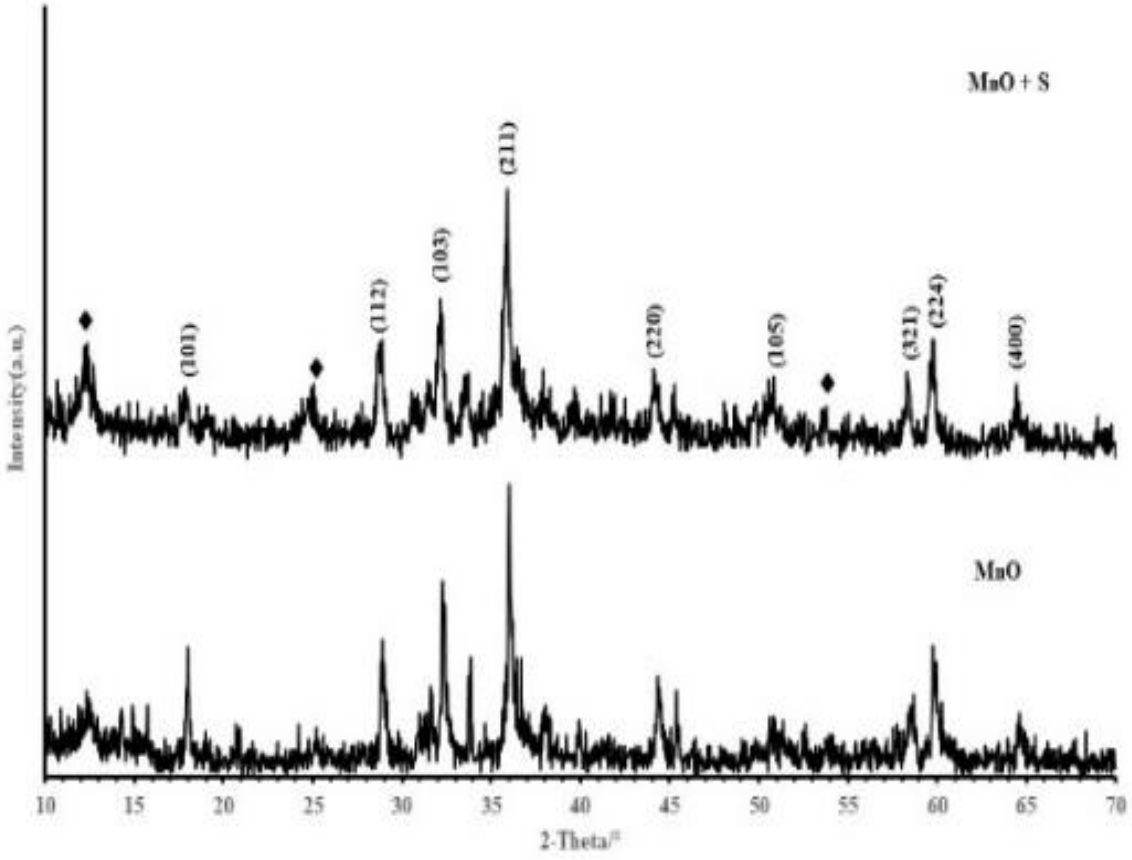

Figure 4.2: The XRD of Manganese Oxide (MnO)

The results of X-Ray Diffraction Analysis of MnO+SS and MnO were shown in Figure 4.2. The XRD pattern as indexed with PC-APD diffraction software is a plot of intensity against 2-theta.

The XRD patterns showed sharper peaks with fewer impurities for the MnO+S compared to that of the control MnO. However, there were more MnO peaks in the MnO+S patterns than in the control. This implied that the presence of starch allowed for the formation of more of the dioxide impurity phases. starch also supported the formation of larger particle sized MnO+S nanoparticles. The estimated particle sizes of the MnO indexed peaks gave 51.984 and 34.083nm for the MnO+S and MnO respectively. The MnO showed more affinity for starch. This agreed with the broader peaks pattern observed in the MnO compared to the MnO+S broad peaks.

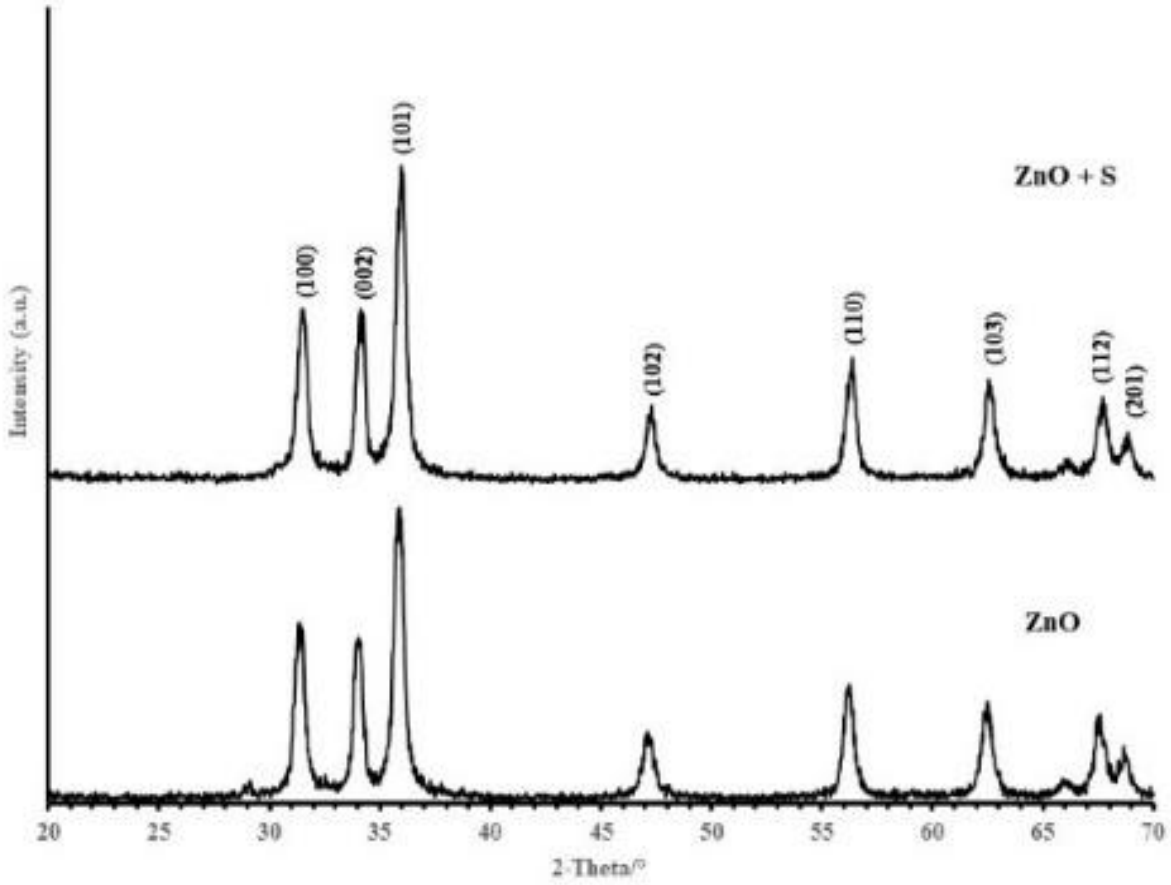

Figure 4.3: The XRD of Zinc Oxide (ZnO)

The results of X-Ray Diffraction Analysis of ZnO+SS and ZnO were shown in Figure 4.3. The XRD pattern as indexed with PC-APD diffraction software is a plot of intensity against 2-theta.

The XRD patterns show sharper peaks with no impurities for the ZnO+S compared to that of the control ZnO. However, there were more ZnO_2 peaks in the ZnO+S patterns than in the control. This implied that the presence of starch allowed for the formation of more of the dioxide impurity phases. The starch also supported the formation of smaller particle sized ZnO+S

The ZnO+S showed small particle size than its control; 59.75 and 62.01 respectively from sharer's equation unlike in the XRD results for Fe4O3 and MnO Nanomaterals.

4.2 Scanning Electron Microscopy (SEM) and Energy Dispersive Spectroscopy (EDS)

Characterization and elemental analysis of the morphology of the synthesized Fe_3O_4; MnO and ZnO with and without starch were made by scanning electron microscopy analysis (SEM, PRO:X: 800-07334Phenom, SN. MVE 01570775). The SEM facility is integrated with energy dispersive spectroscopy (EDS) devise. The results were shown in Figures 4.4; 4.5 and 4.6 for both morphology of ordinary nanomaterials and starch modified nanomaterials (samples and controls) and morphologies with EDS respectively. Figures 4.4a; 4.5a and 4.6a showed the morphologies of the sample with starch while controls without starch were shown in Figures 4.4b; 4.5b and 4.6b respectively. The EDS of the three samples are shown in Figures 4.4c; 4.5c and 4.6c for the samples with starch, while of their controls are shown in Figures 4.4d; 4.5d and 4.6d respectively. The EDS results confirmed the Fe, Mn and Zn contents of the samples and controls as expected.

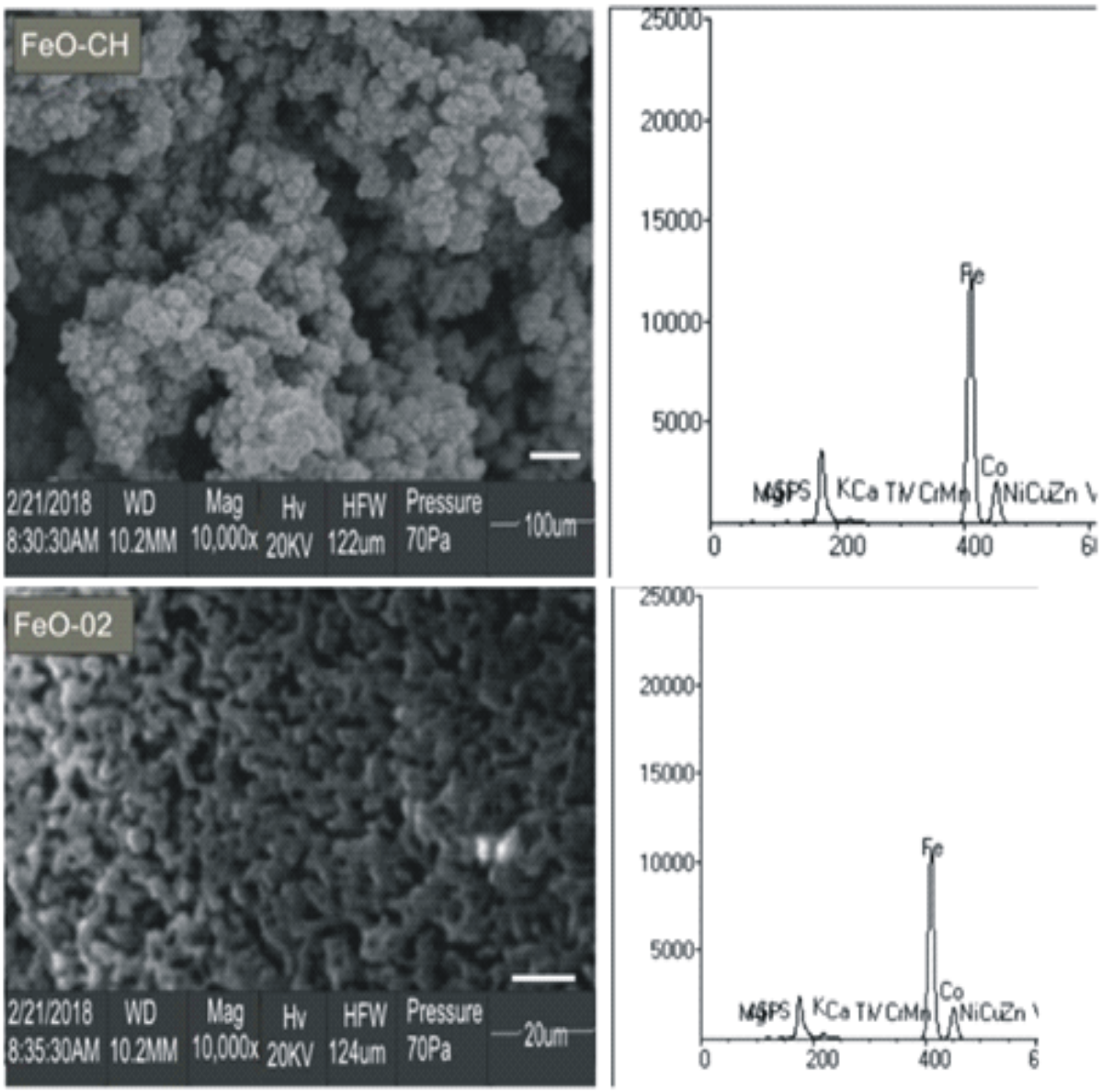

Plate 4.4 Details of surface morphology of the synthesized Fe_3O_4+SS and Fe_3O_4 alone obtained from scanning electron microscopy (a/b) with their energy dispersive spectroscopy (EDS) C/D respectively.

The SEM showed the following characteristics of Fe_3O_4+SS; (a) There were granular clustered polycrystallite with open spaces between clusters, (b) there was Polycrystalite porous network. (c) SEM for Fe_3O_4+SS also showed larger polycrystallite compared to the smaller edged vertical polycrystalite plates of the Fe_3O_4.

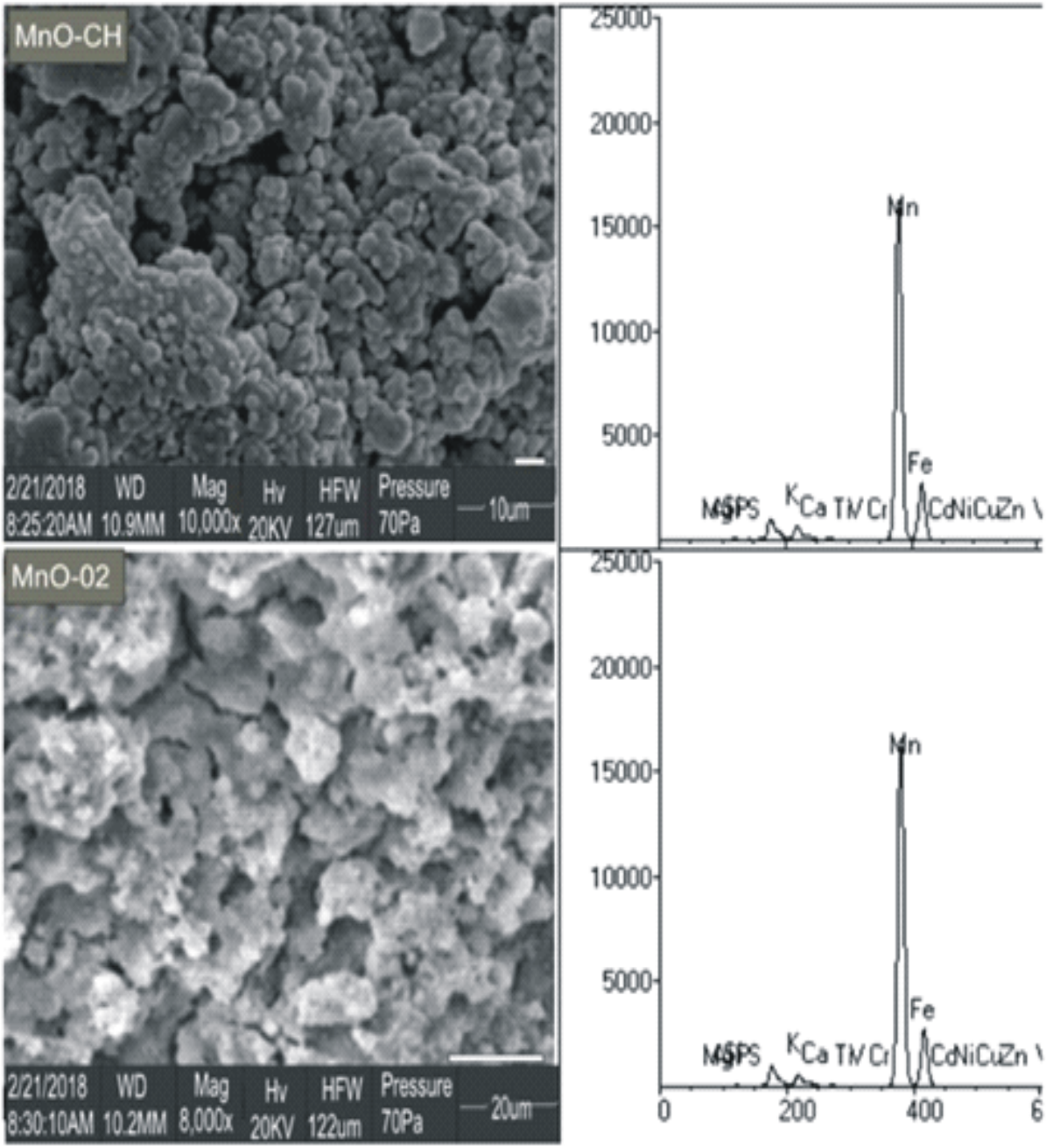

Plate 4.5 The details of surface morphology of the synthesized MnO+SS and MnO obtained from scanning electron microscopy (a/b) with their energy dispersive spectroscopy (EDS) C/D respectively.

The surface of the control sample (MnO) revealed a rough, porous plate-like polycrystalline, while that of the sample with (MnO-SS) appeared as platy but with more organized net-like pores.

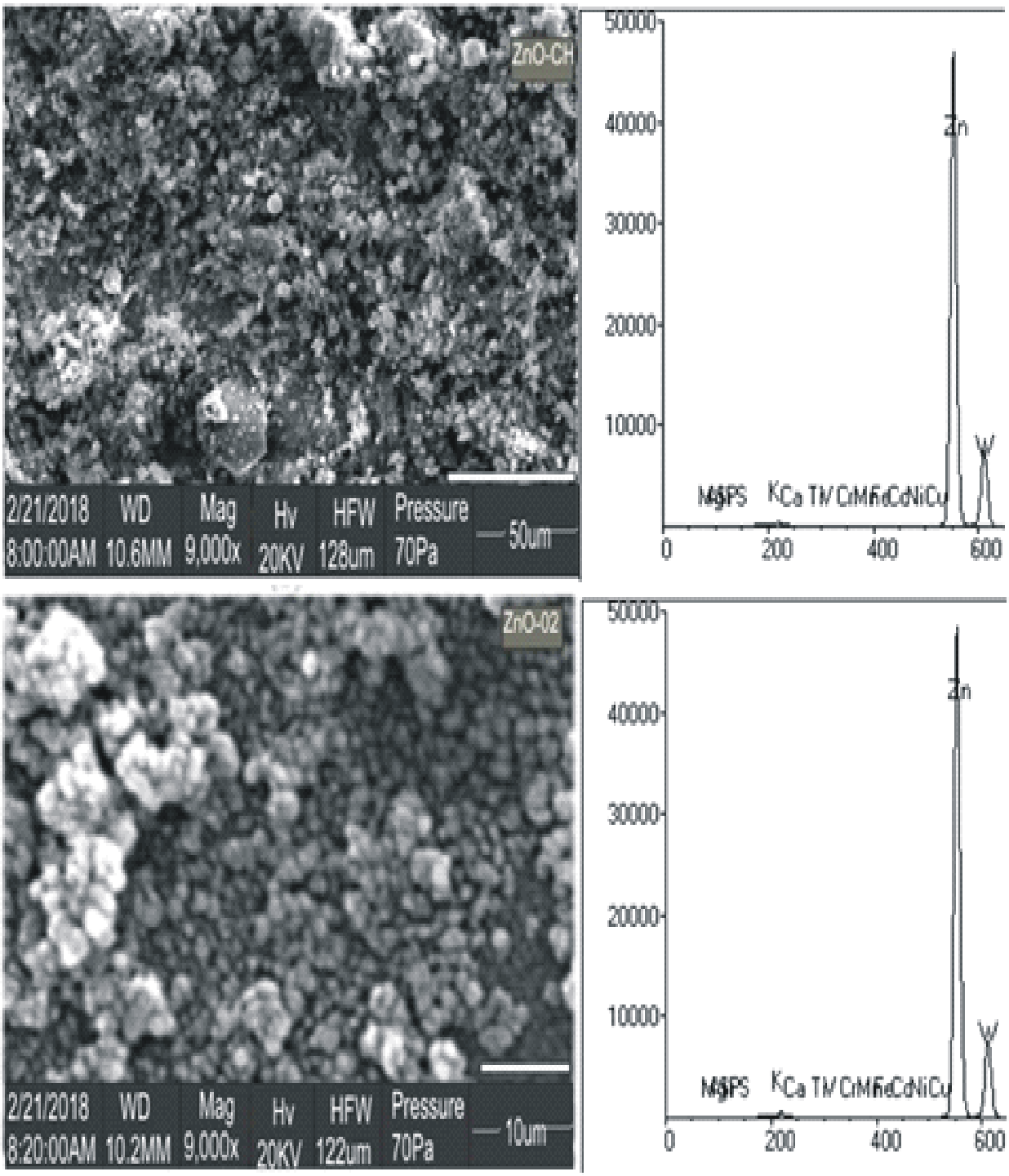

Plate 4.6 The details of surface morphology of the synthesized ZnO+SS and ZnO alone obtained from scanning electron microscopy (a/b) with their energy dispersive spectroscopy (EDS) C/D respectively.

The SEM of ZnO+SS showed a fine like polycristallite, with porous and spongy surface while that of ZnO is spaced with clustered grains**.** Previous studies have proven that surface morhpology of adsorbent materials play determinant roles in uptake capacity of contaminants in solution during adsorption processes (Hameed, et al 2013, Zahoor 2019). Adsorbents of large surface area possess higher adsorption capacity.

4.3 The Fourier Transform Infra-red (FTIR)

The synthesized metal oxide nanoparticles were characterized using the FTIR (Perkin Elmer Spectrum two C-92485) to show the functional groups with the metal oxides synthesize with starch and their controls.

The FTIR characterized Nano particles are shown in Figures 4.4 (a and b) for Fe_4O_3 and Fe_4O_3-SS, figs 4.5 (a and b) for MnO and MnO-SS and figs 4.6 (a and b) for ZnO and ZnO-SS.

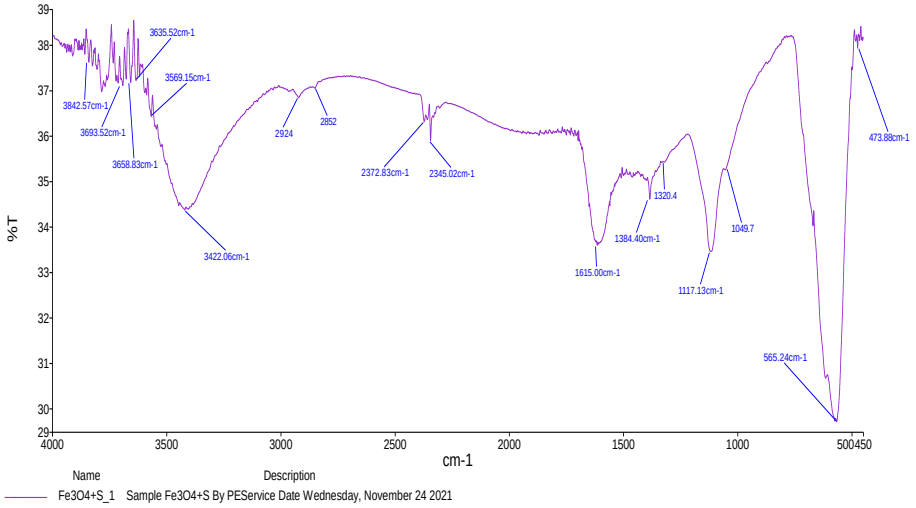

(a)

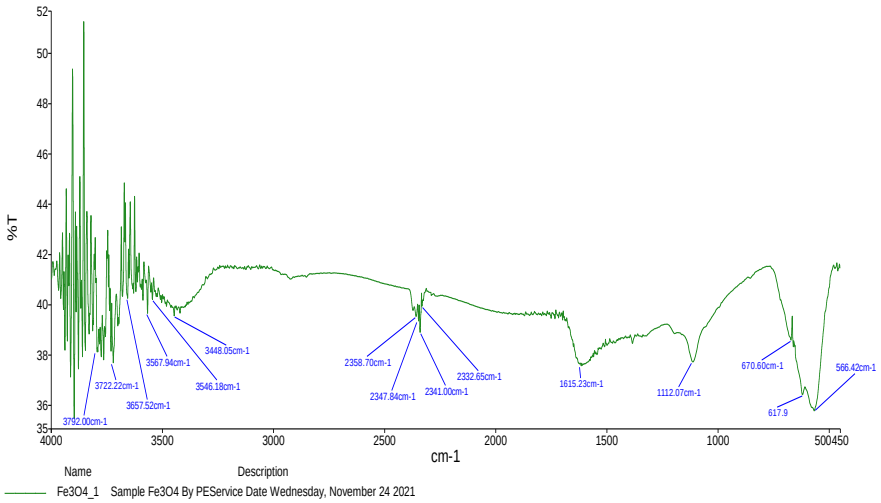

(b)

Figure **4.4 The FT-IR spectra of the magnetite (Fe_3O_4) nanoparticles synthesised with and without starch respectively (a, b) in wave number range 450-4000cm^{-1}**

It was observed from Figures 4.4a and 4.4b that the starch modified Fe_3O_4 (Fe_3O_4-SS) was showing two peaks in comparison to ordinary Fe_3O_4 (control) which had three peaks. The absorption bands of Fe_3O_4+S at 473.88 and 565.24 cm^{-1} indicated the metal-oxygen bond Fe-O, the bands at 3422.06, 2924,2852,2372.83 and 2345.02 cm^{-1} indicated the presence of stretching O-H vibrations. The peaks at 1615,1384.40,1320.4 and 1117.13cm^{-1} corresponded to C=O, $(CH_2)_n$

Absorption bands at 566.42, 617.90 and 670.60 cm^{-1} were observed in FT-IR spectra for **Fe**$_3O_4$ (control) as shown on fig4.4b. These bands indicate Fe -oxygen bond (Fe-O).

The bands at 3546.18, 3448.05,2358.70, 2347.84,2341 and 2332.65 cm^{-1} indicate the stretching O-H vibrations. The peaks at 1615.23 and 112.07cm^{-1} were due to C=O, $(CH_2)_n$ and C-O.

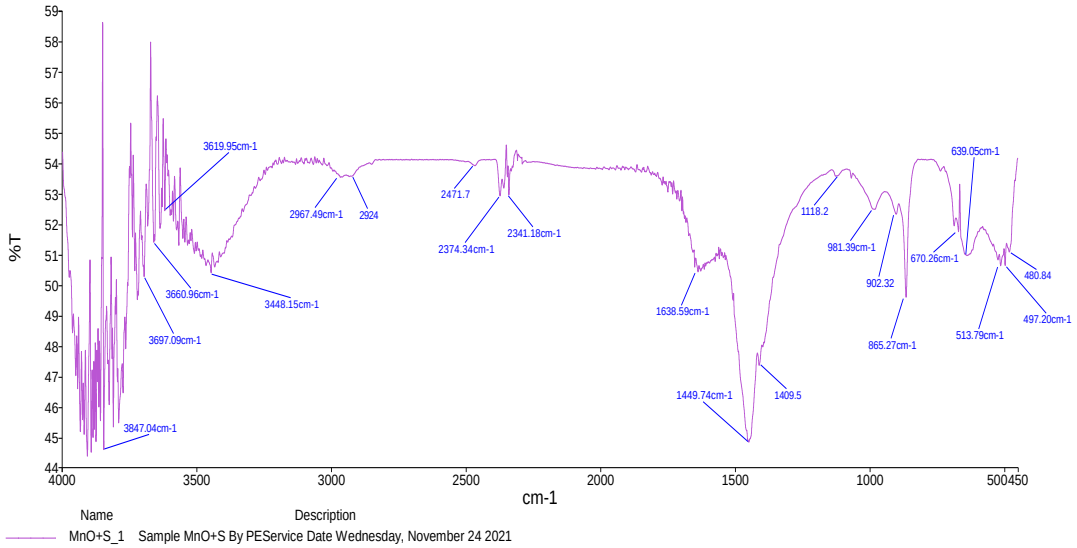

(a)

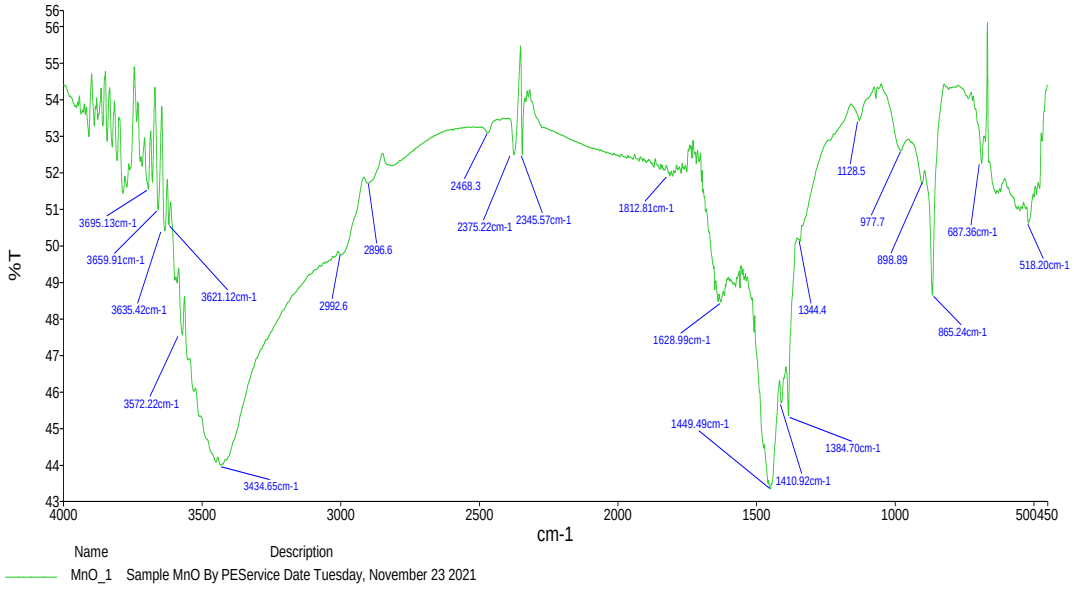

(b)

Figure 4.5 The FT-IR spectra of the Manganese Oxide (MnO) nanoparticles synthesised with and without starch respectively (a, b) in wave number range 450-4000cm^{-1}

The synthesized MnO were characterized using FTIR and the analysis was shown in Figures 4.8 (a and b). It was observed that the MnO with starch showed bands at 480.84,497.20 and 513.79 cm^{-1} which indicated the vibration of the metal-Oxygen bond (Mn-O)

Absorption peaks observed at 2967.49 and 2924.00 cm^{-1} were due to $-CH_3$ stretching vibrations. The absorption peaks at 2471.7,2374.34,2341.18,1449.74 and 1409.5 may be due to $-CH_2$ stretching, = C-H stretching and -C-H stretching vibrations.

For MnO without starch, the following bands waves observed at 518.20, 687.36, 898.89 and 977.7 cm^{-1} indicating the vibration of the Mn-Oxygen bond (Mn-O).

Absorption peaks observed at 2992.6 may be due to $-CH_3$ stretching vibrations.

The absorption peaks at 2896.6,2468.3,2345.57,1812.81,1628.99,1449.49 and 1384.70 cm^{-1} may be due to $-CH_2$ stretching, =C-H stretching and -C-H stretching vibrations.

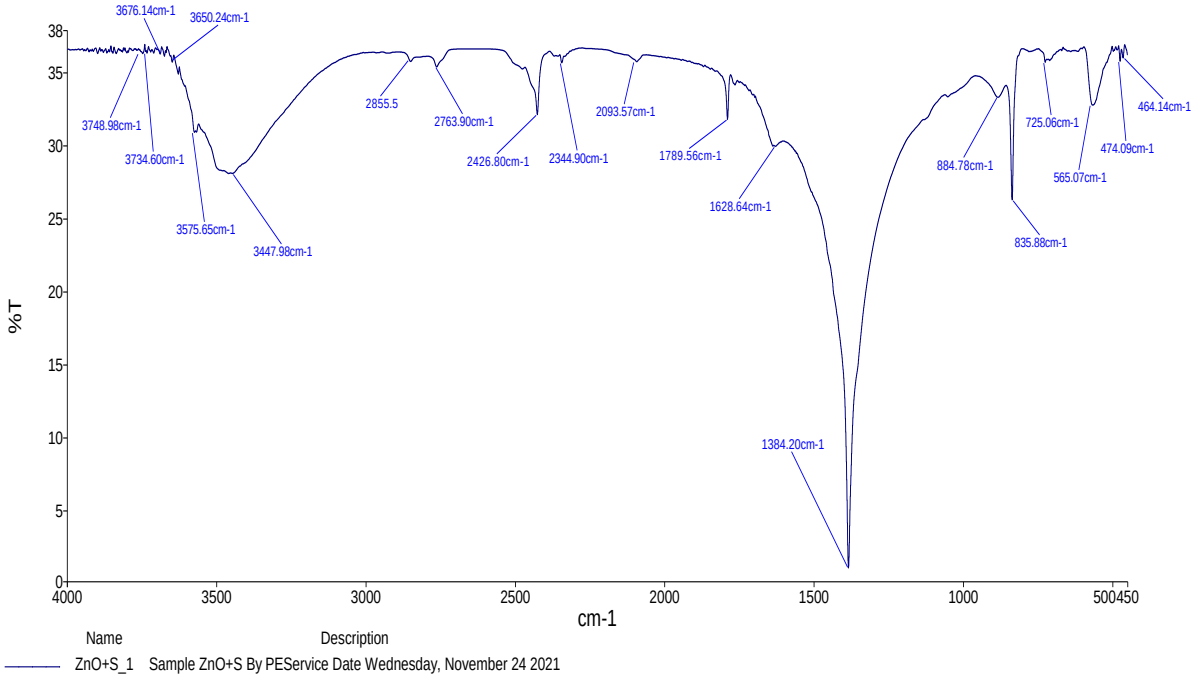

(a)

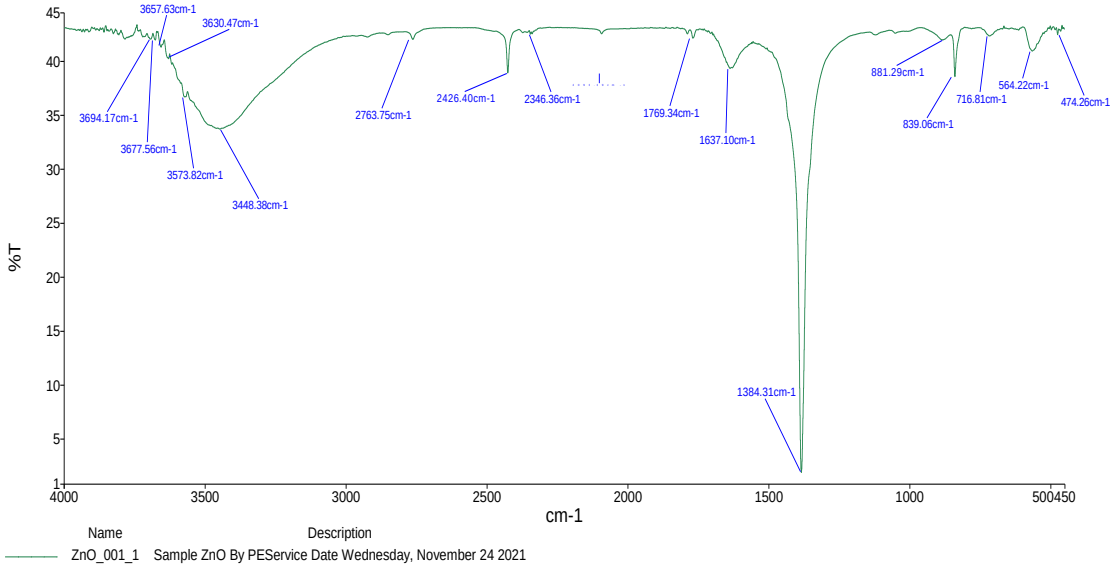

(b)

Figures 4.6: The FT-IR spectra of the Zinc Oxide (ZnO) nanoparticles synthesised with and without starch respectively (a, b) in wave number range 450-4000cm^{-1}

The synthesized ZnO were characterized using FTIR and the analysis was shown in Figures 4.9 (a and b). It was observed that the ZnO with starch showed bands at 464.14 and 474.09 cm^{-1} which indicated the vibration of the metal-Oxygen bond (Zn-O)

The broad band peak at 3447.98 cm^{-1} can be attributed to the characteristic's absorption of hydroxyl.

While the, ZnO without starch had the following characteristics, the band at 474.26 cm^{-1} indicated the vibration of the metal-Oxygen bond (Zn-O).

The broad band peak at 3448.38 cm^{-1} can be attributed to the characteristic's absorption of hydroxyl.

Table 4.1: The elemental composition analysis of the magnetite (Fe_3O_4) synthesized with and without starch through the sol-gel method using the X-RF (a and b) respectively.

Element	Fe_3O_4	SO_3	SnO_2	Cl	La_2O_3	MnO	Al_2O_3	SiO_2	CaO	K_2O
Wt(%)	56.630	0.921	1.127	4.035	1.375	0.405	0.412	0.261	0.023	0.10

(a)

Element	Fe_3O_4	SO_3	SnO_2	Cl	La_2O_3	MnO	Al_2O_3	SiO_2	CaO	K_2O
Wt(%)	55.789	1.093	1.0	3.323	1.485	0.556	0.50	0.514	0.10	0.10

(b)

The chemical composition (wt.%) of Magnetite Nanoparticle source used in the study were presented in the Table 4.1 above. Stating that the above did not follow the analysis, the one with starch had larger particle than one without starch stating that the surface modification was effective.

Table 4.2: The elemental composition analysis of the manganese Oxide (MnO) synthesized with and without starch through the sol-gel method using the X-RF.

Element	Fe_2O_3	SO_3	SnO_2	Cl	La_2O_3	MnO	Al_2O_3	SiO_2	CeO_2	K_2O
Wt(%)	0.331	0.126	1.138	4.180	0.354	88.512	0.551	1.129	1.0	0.10

(a)

Element	Fe_2O_3	SO_3	SnO_2	Cl	La_2O_3	MnO	Al_2O_3	SiO_2	CeO_2	K_2O
Wt(%)	0.493	0.140	1.126	4.453	0.240	63.457	0.792	1.540	1.0	0.132

(b)

The chemical composition (wt.%) of Manganese Oxide Nanoparticle as shown above, indicated that the MnO with starch had 88.512% which was a larger particle than that without starch which was 63.457%%.

Table 4.3: The elemental composition analysis of the Zinc Oxide (ZnO) synthesized with and without starch through the sol-gel method using the X-RF.

Element	ZnO	WO_3	SnO_2	Cl	La_2O_3	SO_3	Al_2O_3	SiO_2	CeO_2
Wt(%)	59.750	0.117	1.127	0.038	0.00	0.117	0.205	0.10	1.0

(a)

Element	ZnO	WO_3	SnO_2	Cl	La_2O_3	SO_3	Al_2O_3	SiO_2	CeO_2
Wt(%)	62.010	0.104	1.136	0.10	0.10	0.10	0.205	0.10	0.94

(b)

The chemical composition (wt.%) of Zinc Oxide Nanoparticle as shown above. This showed a modification of the ZnO+SS where the particle size was 59.750% and was smaller compared to the ZnO nanoparticle was 62.010%.

4.4 Effects of varying various Adsorption Parameters

Effects of varying adsorption parameters in adsorption processes of metal ion contaminants on both Nano material metal oxide (Fe_3O_4, MnO and ZnO) and starch modified Nano material metal oxide (Fe_3O_4-SS MnO-SS and ZnO-SS) were studied to determine the level of percentage removal of the respective metal ion contaminants from the solution.

4.4.1 The Effect of Contact Time

The effects of varying contact time of adsorption resulting to various degrees of % removal of $As^{3+,}$ $Cd^{2+,}$ $Cr^{6+,}$ Ni^{2+} and Pb^{2+} ions were carried out at time intervals of 5, 10, 15, 20 and 25 minutes and at constant adsorbent mass of 0.5grams, solution concentration of 50mg/l and temperature of 40^{o}C, Figures 4.7 and 4.8 and 4.9 below represent the effects of contact time in adsorption process of metal ion contaminants on Fe_3O_4, Fe_3O_4-SS**;** MnO, MnO-SS and ZnO, ZnO-SS respectively.

-

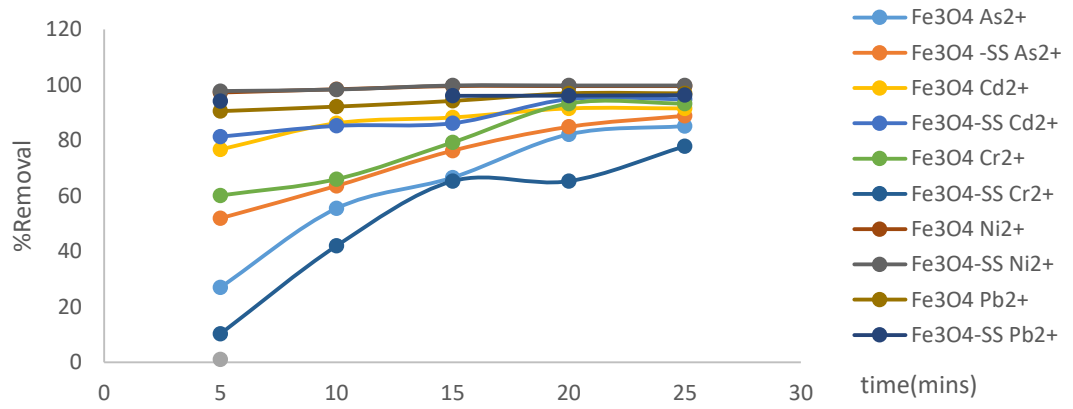

Figure 4.7; percentage removal of the contaminant ions from solution by Fe_3O_4 and Fe_3O_4 -SS

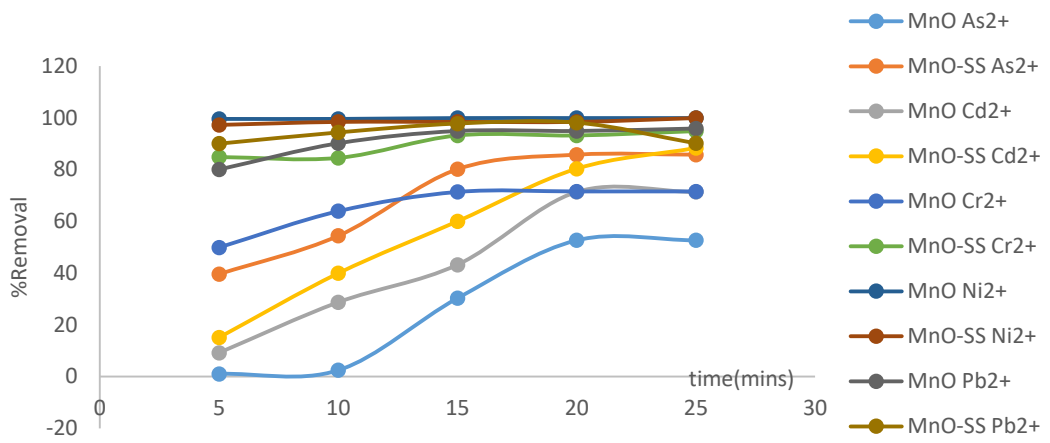

Figure 4.8; % removal of the contaminant ions with time by MnO, MnO-SS at inital conc of 50mg/l, adsorbent mass of 0.5 and temp. of 40^{o}C

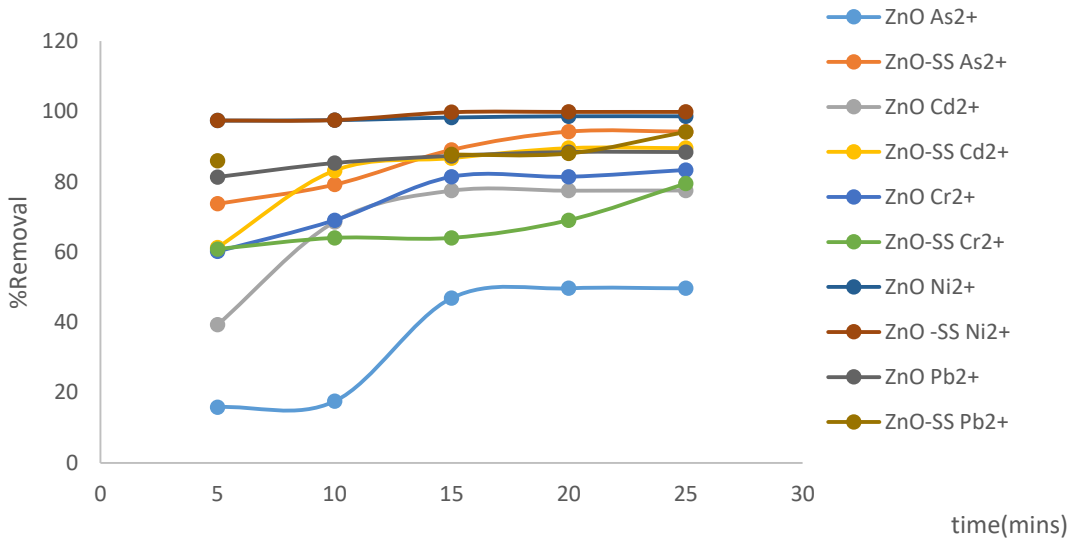

Figure 4.9; % removal of the contaminant ions with time by ZnO, ZnO-SS at inital conc of 50mg/l, adsorbent mass of 0.5 and temp. of 40^{o}C

Percentage removal of the contaminant ions responded with increase in time with a slight slow removal efficient towards the end of adsorption period was observed. The rapid initial removal efficiency observed is attributed to more metal contaminant ions interaction with the uncovered surfaces of the adsorbents as that time elapsed (Shi et al 2013) which resulted to more distributions of $As^{3+,}$ $Cd^{2+,}$ $Cr^{6+,}$ Ni^{2+} and Pb^{2+} ions on the surfaces of Fe_3O_4 ,Fe_3O_4-SS**;** MnO, MnO-SS and ZnO, ZnO-SS Nano materials. The slight decline in % removal could be as a result of Adsorption capacity equilibrium attainment of the adsorbents (Kilic et al., 2011).

From Figure 4.7 the contaminant ions removal efficiency of Fe_3O_4-SS adsorbent was higher than that of Fe_3O_4. Removal capacity of Fe_3O_4-SS was highest with Ni^{2+} contaminant % removal of 98.6 as against Fe_3O_4 with Ni^{2+} maximum % removal of 98.7%. This was followed by 89.5% and 88.7% of Pb^{2+} removal by Fe_3O_4-SS and Fe_3O_4 Nano adsorbents respectively. The least % removal values were observed at Cr^{6+} removal process with maximum values of 8.2% and 21.3% for Fe_3O_4 and Fe_3O_4-SS respectively. The apparent high and low contaminant ions % removal values could be as a result of degree of affinity of the ions to the adsorbents (Hanan *et al* 2010). The degree of affinity of the metal contaminant ions to the adsorbents took place in the following order; Ni^{2+}> Pb^{2+}>Cd^{2+}>As^{3+}>Cr^{2+}.

The highest adsorption capacities of MnO-SS and MnO Nano materials were observed at the removal processes of Ni^{2+} and Cd^{2+} with the maximum % removal of 98.7% and 99.4% (Figure 4.8). The least removal efficiencies of the Nano materials were observed in the processes of Cr^{6+} and As^{3+} removal. The maximum % removal values for the two metal ions (Cr^{6+} and As^{3+}) were observed to be at 7.3 and 29.5% respectively and the order of % removal of various contaminant metal ions was observed as; Ni^{2+}>Cd^{2+} >Pb^{2+}>As^{3+}>Cr^{6+}. Again, affinity of metal ion contaminants to the adsorbents played a huge role on the apparent % removal variations. From the result, As^{3+} and Cr^{6+} have lower degree of affinity to the

adsorbents than the other metal ions as a substantial amount of As^{3+} and Cr^{6+} was not adsorbed on the adsorbent, rather remained in solution.

Results in Figure 4.9 showed that Ni^{2+} and Pb^{2+} were mostly removed by ZnO and ZnO-SS Nano materials adsorbent with maximum % removal values at 99.2 and 94.2% respectively.

The maximum percentage removals of Cd^{2+}, As^{3+} and Cr^{6+} were observed at 93.5% 64% and 81.6% respectively. There was significant improvement on % removal of As^{3+} and Cr^{6+} by ZnO and ZnO-SS adsorbents compared with that of Fe_3O_4-SS and Fe_3O_4 and MnO-SS and MnO. The reason could be attributable to more affinity of As^{3+} and Cr^{6+} to the active groups of ZnO and ZnO-SS. The results equally showed that all the Nano materials (Fe_3O_4-SS and Fe_3O_4**;** MnO-SS and MnO and ZnO and ZnO-SS) under study have measurable adsorption capacity for Ni^{2+} followed by Pb^{2+}, Cd^{2+}, Cr^{6+} and As^{3+} in descending order. Specifically, the starched modified Nano adsorbents (Fe_3O_4-SS, MnO-SS and ZnO-SS) showed higher adsorption capacity for the removal of metal ion contaminants than the ordinary Nano adsorbents (Fe_3O_4**;** MnO and ZnO). The organic active groups and widening of active surface area due to introduction of starch accounted for the high adsorption capacity (Hanan et al., 2010).

4.4.2 Effects of Temperature.

Results of the effects of varying temperature between 40 to 80^{o}C at intervals of 10^{o}C in adsorption processes of metal ion contaminants ($As^{3+,}$ $Cd^{2+,}$ $Cr^{6+,}$ Ni^{2+} and Pb^{2+}) onto ordinary and starch modified metal oxide Nano adsorbent (Fe_3O_4-SS, Fe_3O_4**;** MnO-SS, MnO and ZnO-SS, ZnO) are presented in Figures 4.10, 4.11 and 4.12.

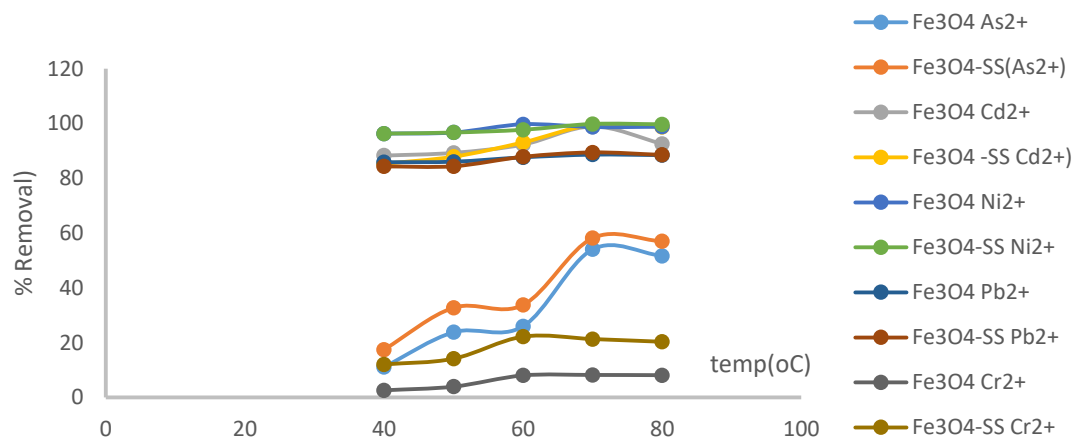

Figure 4.10; % removal of the contaminant ions with temp by Fe_3O_4 ,Fe_3O_4-SS at inital conc of 50mg/l, adsorbent mass of 0.5g at the time of 25mins

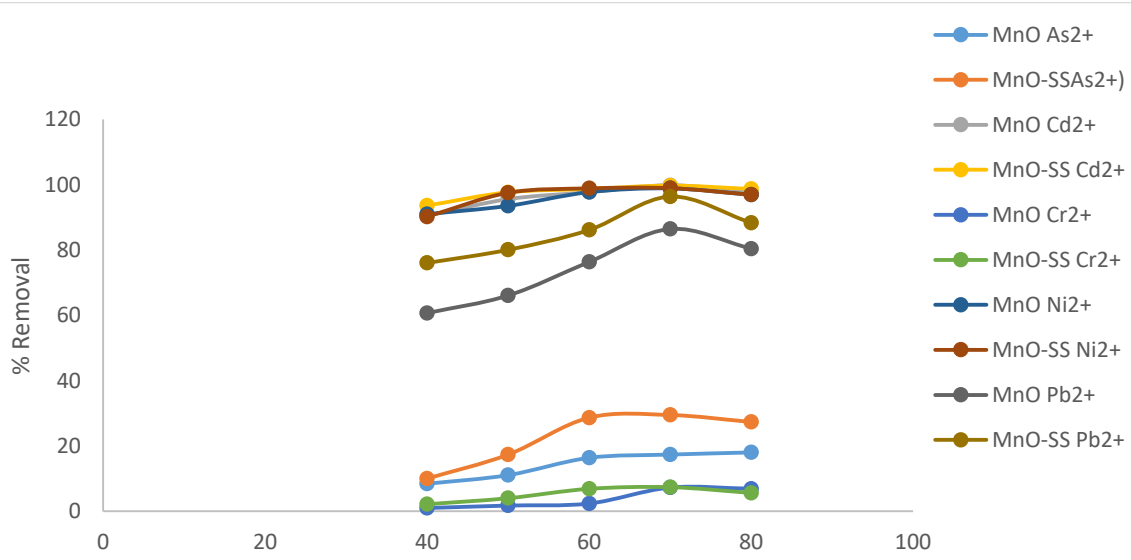

Figure 4.11; % removal of the contaminant ions with temp by MnO ,MnO-SS at inital conc of 50mg/l, adsorbent mass of 0.5g at the time of 25mins

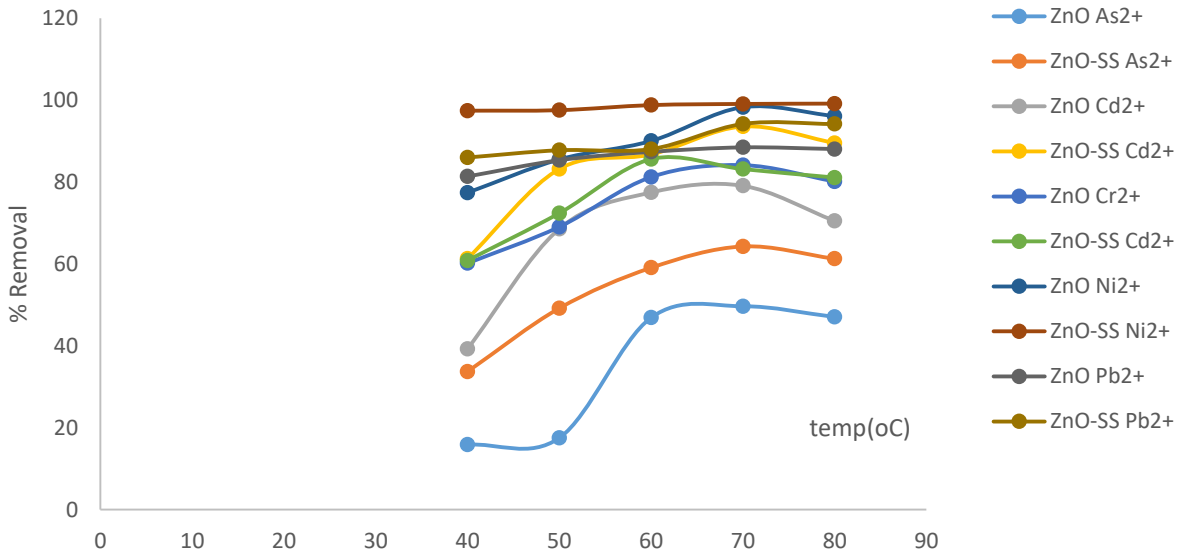

Figure 4.12; % removal of the contaminant ions with temp by ZnO ,ZnO-SS at inital conc of 50mg/l, adsorbent mass of 0.5g at the time of 25mins

The study was carried out at initial concentration of 50mg/l, adsorbent mass of 0.5g and time interval of 25 minutes. It was observed from the Figures that % removal seemed to be on the decline as the temperature approached maximum level. The prevailing scenario may be ascribed to breakage of intermolecular bonds between the contaminant ions and the metal oxide Nano materials at high temperature (Aseel et al., 2014), leading to desorption of adsorbed contaminant ions into the solution. Again, solubility of the metal ion in the solvent at high temperature might result to stronger interaction between the metal ions and solvent than between the metal ions and the adsorbents (Fe_3O_4-SS, Fe_3O_4**;** MnO-SS, MnO and ZnO-SS,ZnO). this scenario may lead to non-availability of the precipitated metal ion contaminant for adsorption (Hanan et al 2010). In fig4.10 which represents the adsorption pattern of $As^{3+,}$ $Cd^{2+,}$ $Cr^{6+,}$ Ni^{2+} and Pb^{2+} ions onto Nano materials of Fe_3O_4-SS, Fe_3O_4 with varying temperature range, the highest % removal by both adsorbents was shown to be Ni^{2+} having 99.6% and 99.8% by both Fe_3O_4- and Fe_3O_4-SS, Nano adsorbent materials respectively.

The maximum percentage removals of Cd^{2+} by Fe_3O_4- and Fe_3O_4-SS, adsorbents were 83 and 93% respectively. The lowest % removal was recorded against Cr^{2+} with 8% and 22% for Fe_3O_4 and Fe_3O_4-SS respectively. Percentage Removal of all the ions by both adsorbents (Fe_3O_4- and Fe_3O_4-SS) are arranged in descending order as follows; Ni2+>Cd^{2+}>Pb^{2+}>As^{3+}>Cr^{6+}.

Percentage removal of the contaminant metal ions as carried out by MnO**;** MnO-SS Nano absorbent and shown on Figure 4.11 produced removal pattern (Cd^{2+}>Ni^{2+}>Pb^{2+}>As^{3+}>Cr^{6+}) slightly different from that of Fe_3O_4- and Fe_3O_4-SS with lower values. Maximum % removal values for (Ni^{2+} and Cd^{2+} by MnO**;** MnO-SS were observed at 93.5% **:**96%, and 97%**:** 98% respectively. Lead ion (Pb^{2+}) % removal recorded lower values of 76.4% and 86.2% respectively by MnO and MnO-SS Nano adsorbent compared to Fe_3O_4- and Fe_3O_4-SS.

Chromium ion (Cr^{6+}) has the lowest % removal values of 7.2% and 8% for MnO and MnO-SS Nano materials after Arsenic ion (As^{3+}) with % removal values of 17.4% and 29.5%.

As shown on Figure 4.12, the maximum adsorption capacities of ZnO and ZnO-SS on % removal of Ni^{2+} (98.2% and 99.1%) are higher than that of Cd^{2+} (79% and 93%) and downward % removal trend was observed as follows; Pb^{2+}(86% and 87.8%), Cr^{6+}(84.1% and 85.6%) and As^{3+} (48.9% and 59%).

From the Figures, the maximum % removal values for metal ions took place at optimum temperature of 70^{o}C beyond which decline in percentage removal or adsorption capacities of various adsorbent Nano material was observed. This trend could be ascribed to decrease in the boundary layer thickness around the adsorbent (Shi et al., 2013). According to Kilic et al., (2011) the scenario reduces the resistance to contaminant mass transfer to the adsorbents. Also, at temperature beyond the optimum, adsorption could experience a downward trend arising from solubility of the adsorbates both in solution and the ones already adsorbed on the adsorbents (Aseel et al 2014). In the present study, the boundary layer thickness surrounding the Fe_3O_4-SS, Fe_3O_4**;** MnO-SS, MnO and ZnO-SS,ZnO Nano adsorbents seemed to have been reduced beyond 70^{o}C. Again, dissolution of the adsorbate metal ions (Ni^{2+}, $Cd^{2+,}$ $Pb^{2+,}$ As^{3+} and Cr^{6+} may have been reduced at 70^{o}C. Also, from the Figures, Starch modified Nano adsorbents (Fe_3O_4-SS, MnO-SS and ZnO-SS) showed higher capacity to adsorb the metal ion contaminants than the ordinary Nano adsorbents (Fe_3O_4, MnO and ZnO) as adsorption temperature value increased. According to Lakshmipathy and Sarada 2015, widening of internal structure of the adsorbents due to elevated adsorption temperature could increase the adsorption capacity of the adsorbents. In this case, starch modified adsorbents experienced more widening of internal structure and improvement in active sites than the non-starch modified ones resulting to higher adsorption capacity.

4.4.3 Effect of Initial Solution Concentration

The initial solution concentration of the solution significantly impacts on the heavy metal removal process.

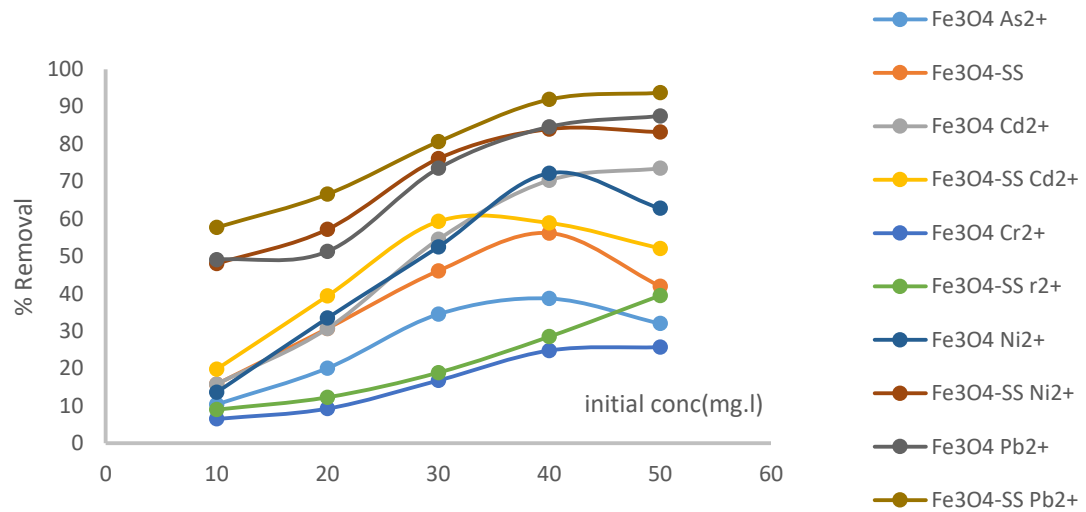

Figure 4.13; % removal of the contaminant ions with Conc by Fe_3O_4; Fe_3O_4;SS at initialTime of 25mins , adsorbent mass of 0.5g and temp. of 40°C

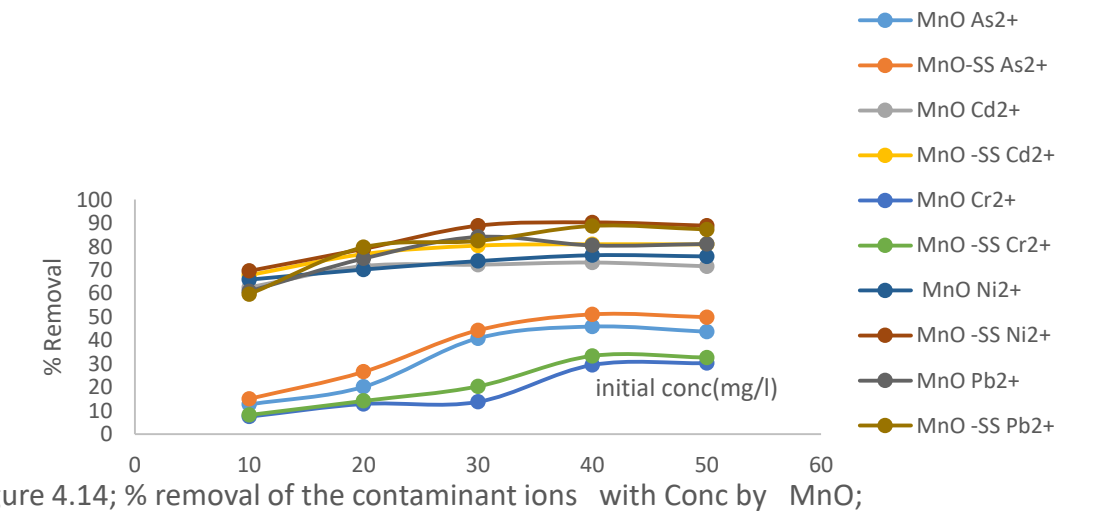

Figure 4.14; % removal of the contaminant ions with Conc by MnO; MnO-SS at initialTime of 25mins , adsorbent mass of 0.5g and temp. of 40°C

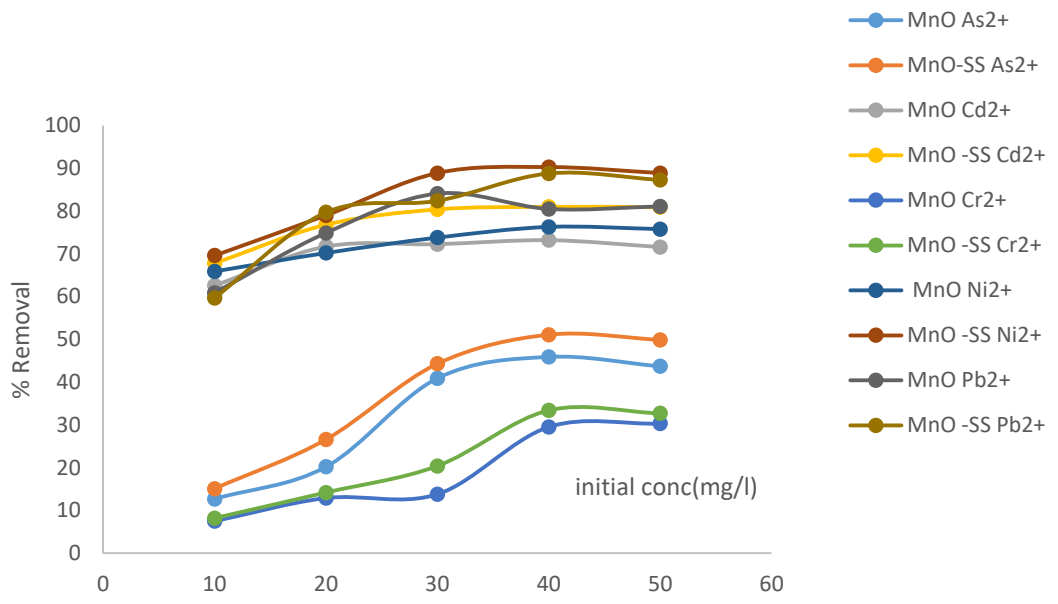

Figure 4.15; % removal of the contaminant ions with Conc by ZnO ; ZnO-SS at initialTime of 25mins , adsorbent mass of 0.5g and temp. of 40^{o}C

Several studies have reported that an increase in the initial concentration resulted in an improvement in the adsorption capacity at the initial stage and a decrease in the overall heavy metal removal efficiency due to non- availability of active sites. (Coruh & Ergun, 2009; Cabrera et al., 2005; Peric et al., 2006; Erdem et al., 2004; Oren and Kaya,2006; Akgu et al., 2006).

In this study, effects of the initial solution concentration on the adsorption process of various contaminant ions (As^{3+}, Cd^{2+}, Cr^{6+}, Ni^{2+} and Pb^{2+}) onto adsorbents (Fe_3O_4-SS, Fe_3O_4**;** MnO-SS, MnO and ZnO-SS, ZnO) surfaces by varying the initial concentrations of the ions in the range of 10, 20, 30, 40 and 50ppm, were shown on Figures 4.13,4.14 and 4.15.

From the Figures, % removal of contaminant ions progressed as the initial concentrations of various ions (As^{3+}, Cd^{2+}, Cr^{6+}, Ni^{2+} and Pb^{2+}) increased until adsorption process got to equilibrium point (which is depicted as a plateau in the curves) where percentage removal began to decline. The reason could be attributed to non- availability of active sites occasioned by the saturation of adsorbent surfaces as also observed by (Sobhy 2014, Uzoije et al., 2015 & Cabrera et al., 2005).

Adsorption of various contaminant ions (As^{3+}, Cd^{2+}, Cr^{6+}, Ni^{2+} and Pb^{2+}) onto Fe_3O_4-SS and Fe_3O_4 adsorbents got to equlilbrum at the optimum initial concentrations of between 30 and 40 mg/l. As^{3+} and $Cd^{2+}$with optimum initial concentrations of 30mg/l had the optimum % removal at 25 and 50% by Fe_3O_4 and Fe_3O_4-SS respectively Cr^{6+}, Ni^{2+} and Pb^{2+} were removed at the optimum percentage of 20%, 80% and 90% respectively. See Figure 4.13

From Figure4.14, adsorption of contaminant ions onto MnO-SS and MnO Nano adsorbents reached equilibrium at initial concentrations range of 30 to 40mg/l of the ions. Adsorptions of Pb^{2+}, Cd^{2+} and Ni^{2+} on both MnO and MnO-SS Nano adsorbents experienced equilibrium at 30mg/l concentrations of the ions. Adsorption surfaces of the MnO and MnO-SS Nano adsorbents got to saturation at the initial concentrations of 40mg/l of As^{3+} and Cr^{6+}. the trend

of % removal of the metal ion contaminants by MnO and MnO-SS Nano adsorbents is shown in this order; $Ni^{2+}>Pb^{2+}>Cd^{2+}>As^{3+}$. Figure 4.15- shows that ZnO and ZnO-SS Nano adsorbents sites got saturated with Cr^{6+} at 20mg/l initial concentration whereas ZnO-SS Nano adsorbent sites were saturated at 20mg/l of Ni^{2+}ion, ZnO Nano adsorbent sites became saturated at 40m/l initial concentration of Ni^{2+}. All other contaminant ions (As^{3+}, Cd^{2+} and Pb^{2+}) saturated the ZnO and ZnO-SS Nano adsorbent sites at initial concentration of 40mg/l at the optimum % removal of 80, 70, and 90% respectively. The apparent variation might be a clear indication of varying adsorption sites due to the presence of starch (Lakshmipathy & Saradab 2015). However, percentage removal of the contaminant ions decreased in this order; $Pb^{2+} > Ni^{2+}>Cd^{2+}>Cr^{6+}>As^{3+}$ by ZnO and ZnO-SS Nano adsorbents.

4.4.4 Effects of Adsorbent Dosage

Effects of adsorbent dosage was investigated by varying adsorbent mass of Fe_3O_4; Fe_3O_4-SS, MnO; MnO-SS and ZnO; ZnO-SS from 0.1 to 0,5g under the contaminant ion initial concentration of 50mg/l, time interval of 25mins and temperature value of 40^oC and were represented in Figures 4.16, 4.17 and 4.18.

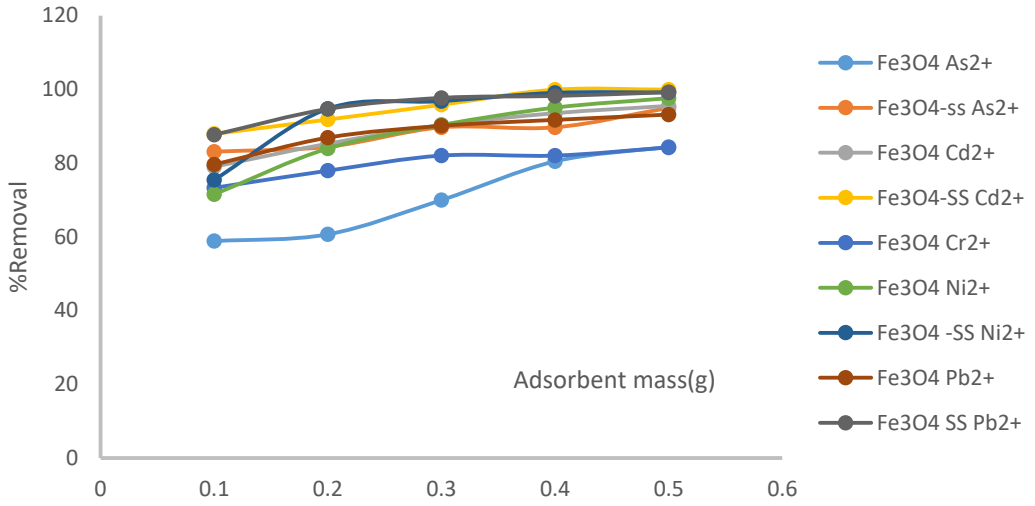

Figure 4.16; % removal of the contaminant ions with adsorbnet mass by Fe_3O_4; Fe_3O_4-SS at initialTime of 50mins , Initial conc of 50mg/l and temp. of 40^oC

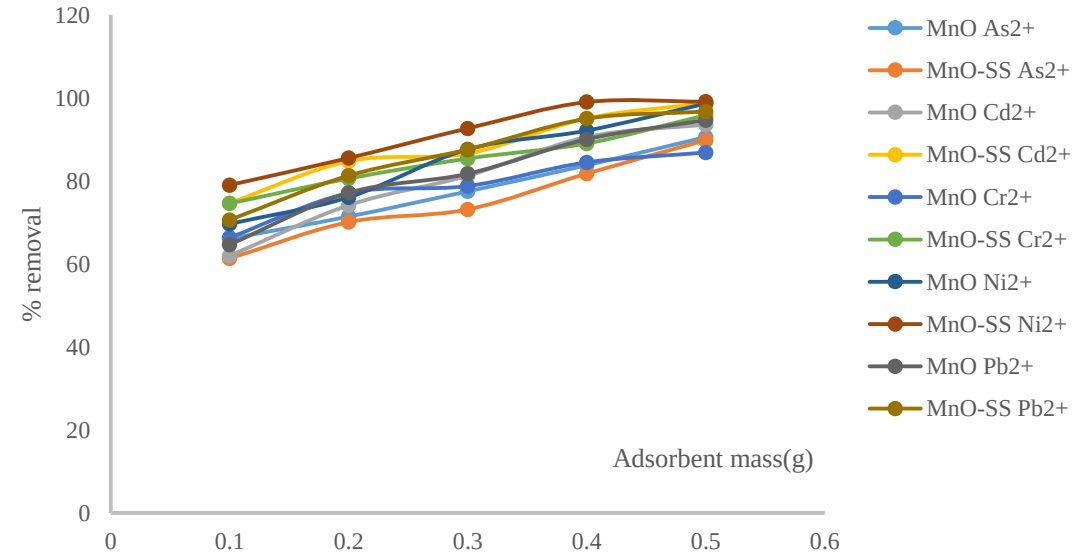

Figure 4.17; % removal of the contaminant ions with adsorbnet mass by MnO; MnO-SS at initialTime of 50mins , Initial conc of 50mg/l and temp. of 40^oC

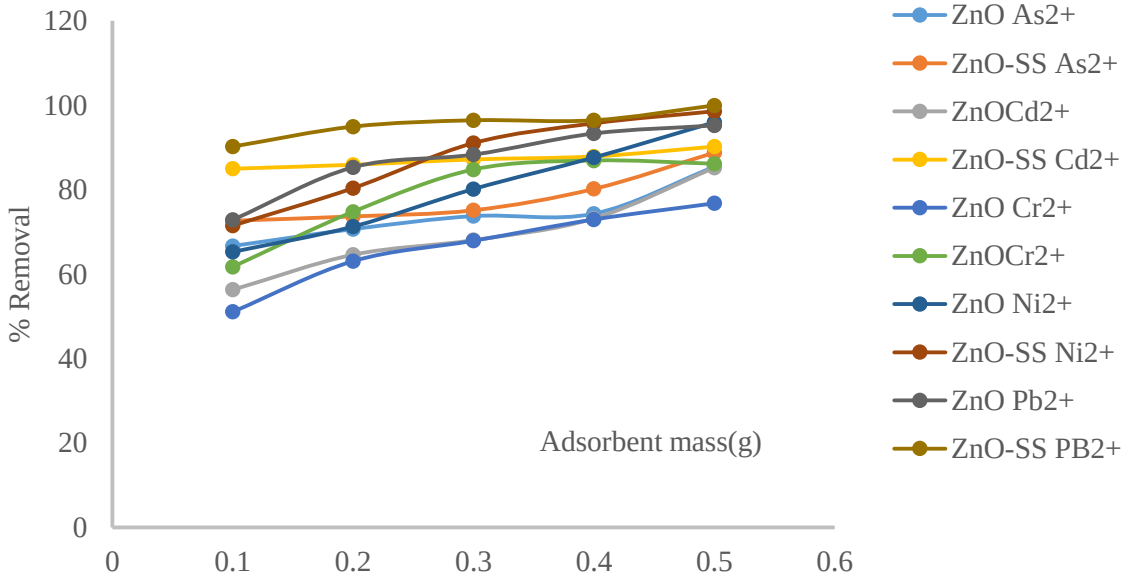

Figure 4.18; % removal of the contaminant ions with adsorbnet mass by Fe_3O_4; Fe_3O_4-SS at initialTime of 50mins , Initial conc of 50mg/l and temp. of 40^oC

There was rapid increase in % removal of metal ion contaminants (As^{3+}, Pb^{2+}, Ni^{2+}, Cd^{2+}, Cr^{6+}) with increase in adsorbent dosage from 0.1 to 0,5g. The initial rapid % removal increase lasted to a point where the onward increase became slower. Zahoora et al. (2019), Nagendran and Noor (2015) attributed the % removal pattern to availability of greater number of adsorbing sites and the apparent slow removal process to saturation of the adsorbent sites. This scenario was observed in all the Nano adsorbents. However, the slowing down of % removal was observed at adsorbent dosage mass of between 0.4 and 0.5g for Fe_3O_4; Fe_3O_4-SS and MnO; MnO-SS and between 0.3 and 0.5g for ZnO; ZnO-SS, suggesting that Fe_3O_4; Fe_3O_4-SS and MnO; MnO-SS have more readily available adsorption sites for the uptake of the metal contaminant ions.

4.5 Adsorption Isotherm Models

Langmuir, Freundlich and Temkin models were applied to simulate the adsorption capacities of Fe_3O_4; Fe_3O_4-SS, MnO; MnO-SS and ZnO; ZnO-SS Nano adsorbents to adsorb the metal ion contaminants. The linearity of the curves produced on testing the adsorption process of the contaminant ions onto various adsorbents using adsorption isotherms indicates that the adsorption sites remained available at all concentrations until equilibrium was established as also observed by Muhammad and Farhat (2018). The linearity curve pattern of the adsorption isotherm implies that partition of the metal ion contaminants (As^{3+}, Cd^{2+}, Cr^{6+}, Ni^{2+} and Pb^{2+}) between the bulk solution and the metal oxide Nano adsorbents(Fe_3O_4; Fe_3O_4-SS, MnO; MnO-SS and ZnO; ZnO-SS) existed while adsorption lasted; under this premise, strong bonds of the contaminant ions with the adsorbents was assumed to have been existed (He et al., 2010).

4.5.1 Langmuir Isotherm Model

Adsorption behaviour of metal ion contaminants (As^{3+}, Cd^{2+}, Cr^{6+}, Ni^{2+} and Pb^{2+}) onto the adsorbents prepared by Nano metal oxides of Fe_3O_4; Fe_3O_4-SS, MnO; MnO-SS and ZnO; ZnO-SS as described by langumiur isotherm model and are shown on Figures 4.19,4.20a; 4.20b - and 4.21a; 4.21 respectively. while the model parameters (K, q_m and R^2) are shown in Table 4.4.

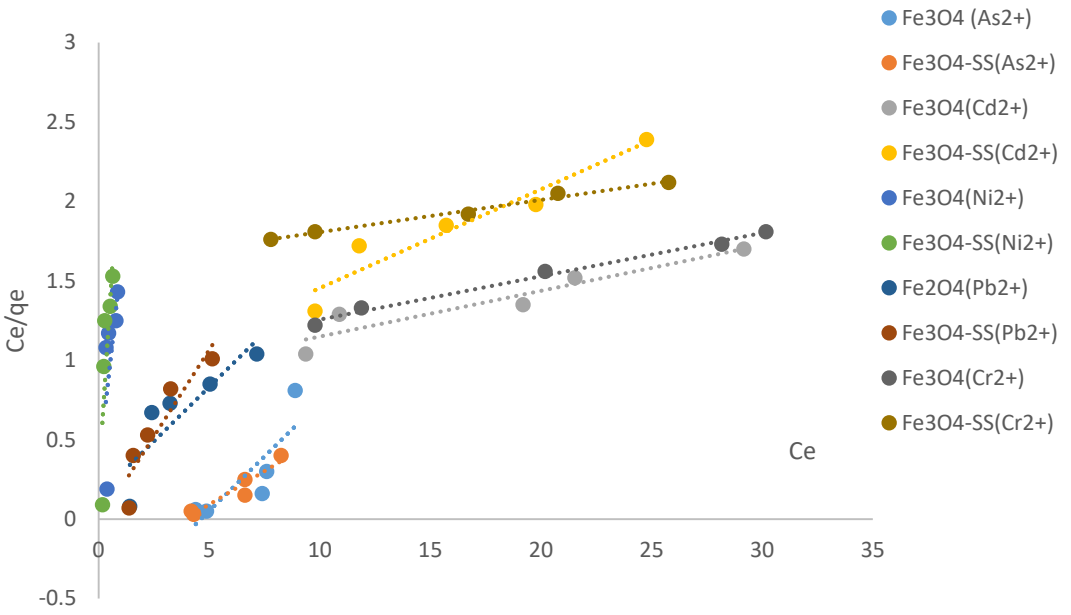

Figure 4.19; langumir isotherm for adsorptions of the contaminant ions on the Nano adsorbents prepared by Fe_3O_4 and Fe_3O_4-SS

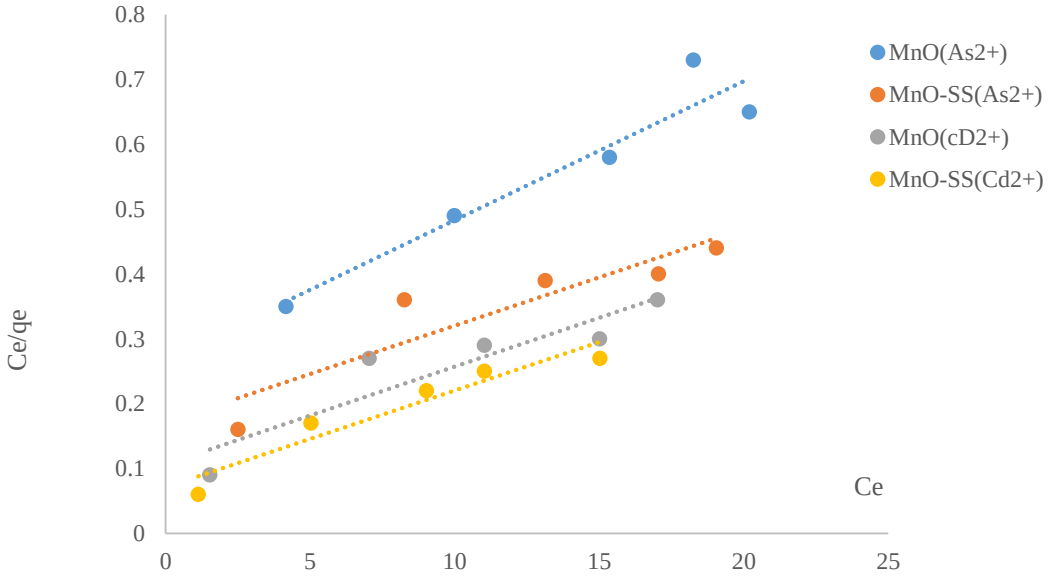

Figure 4.20 ; langmuir isotherm for adsorption of As^{3+} and Cd^{2+} ont the Nano adsorbents preaparred by MnO and MnO-SS materials,

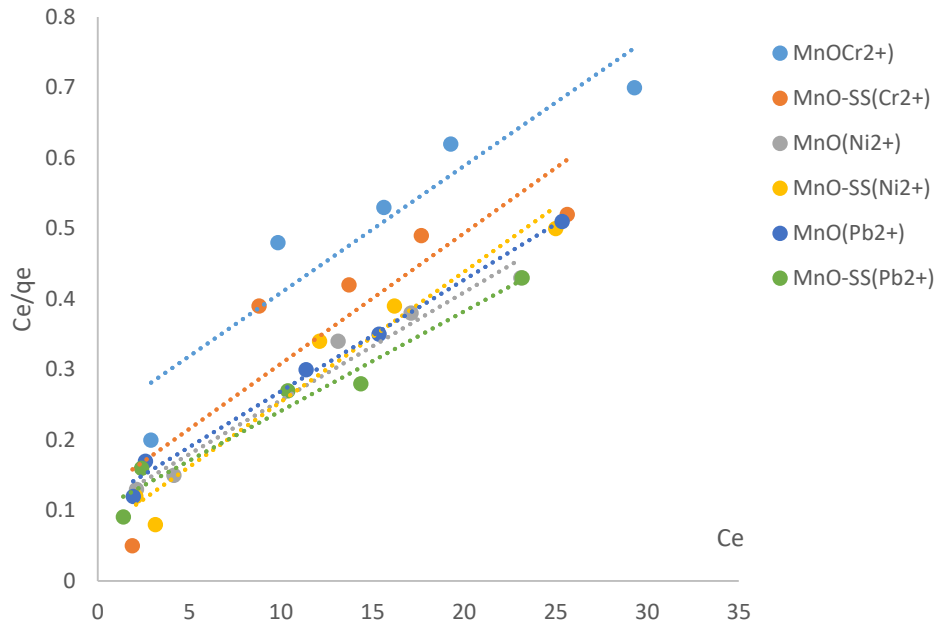

Figure 4.20b ; langmuir isotherm for adsorption of Cr^{6+}, Ni2+ and Pb^{2+} on the Nano adsorbents prepared by MnO and MnO-SS materials,

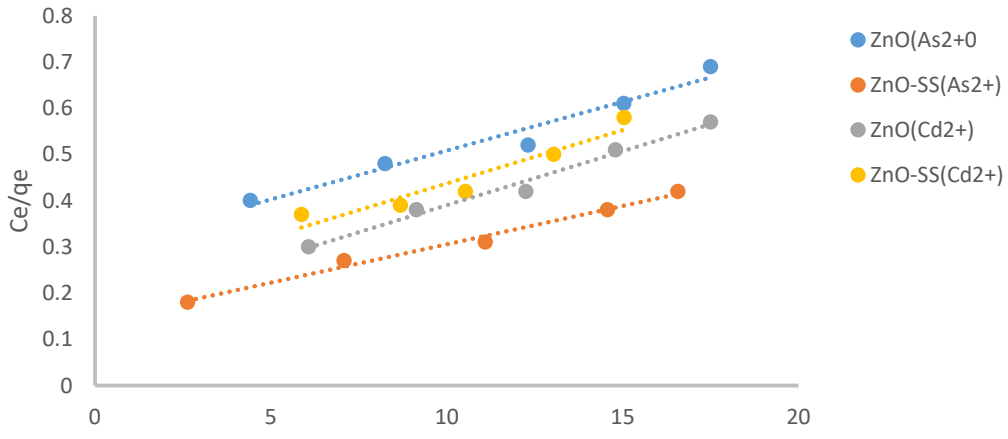

Figure 4.21 ; langmuir isotherm for adsorption of As^{3+} and Cd^{2+} ont the Nano adsorbents preaparred by ZnO and ZnO-SS materials,

Ce

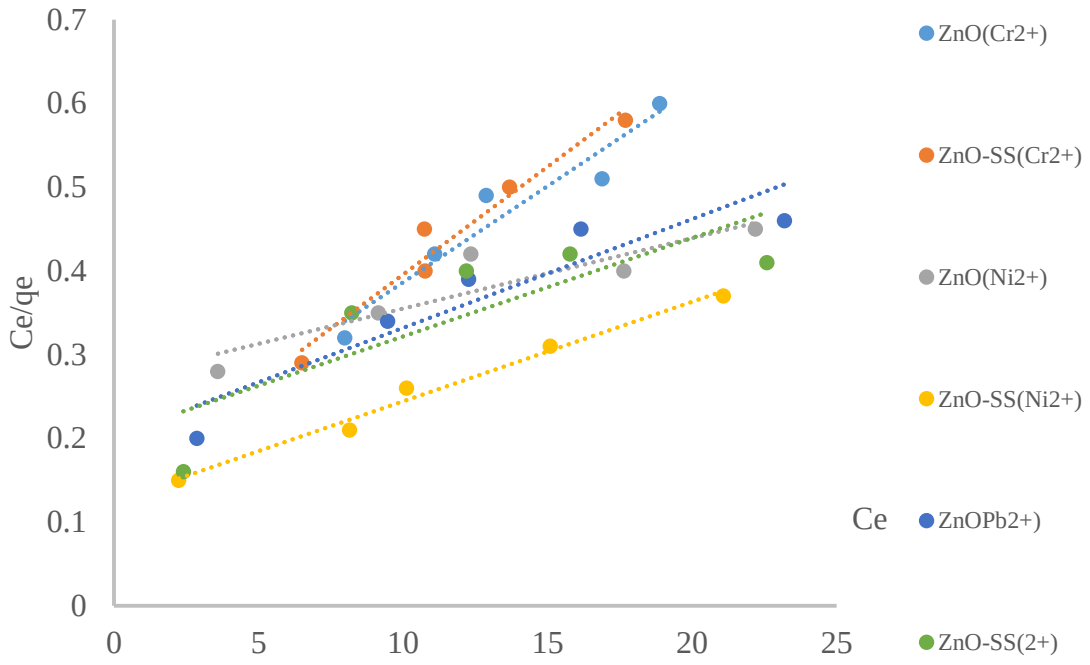

Figure 4.21b ; langmuir isotherm for adsorption of Cr^{6+}, Ni^{2+} and Pb^{2+} on the Nano adsorbents prepared by ZnO and ZnO-SS materials,

Langmuir model reasonably fitted the adsorption data well as R^2 values were observed at between 0.6 and 0.99 except adsorption of Ni^{2+}ion on Fe_3O_4-SS which showed poor correlation at 0.45. High R^2 values observed suggested the following phenomena; that the contaminant ions maintained monolayer coverage pattern on the Nano adsorbents with the exception of Ni^{2+} (Almaraz et al., 2003; Richardson & Harker, 2002), that all the contaminant ions but Ni^{2+} maintained specific adsorption sites and do not transmigrate from one site to another (Tien, 1994, Gunay et al., 2007) and that all adsorption sites are energetically identical and the energy of adsorption is constant (Motsi et al., 2009). However, Langmuir model fitted better in the contaminant ion adsorption onto ZnO; ZnO-SS adsorbents than the other adsorbents. The levels of contaminant ions uptake onto various adsorbents and capacity of various adsorbents to adsorb the contaminant ions is represented by q_m and K_L and are shown in Table 4.4.

Table 4.4 showing Langmuir model parameters of metal ion contaminant adsorption onto ordinary and starch modified metal oxide Nano adsorbent

	Langumir																	
	Fe_3O_4			Fe_3O_4-SS			MnO			MnO-SS			ZnO			ZnO-SS		
	K_L	q_m	R^2	K_L	q_m	R^2	K_L	q_m	R^2	K_L	q_m	R^2	K_L	q_m	R^2	K_L	q_m	R^2
As^{3+}	0.25	11.9	0.9	-4.2	7.23	0.7	0.08	46.73	0.9	0.09	67.11	0.8	0.07	47.39	0.95	0.12	60.24	0.98
Cd^{2+}	0.03	34.7	0.8	0.07	16.1	0.98	0.14	66.7	0.85	0.21	67.11	0.8	0.15	42.73	0.98	0.11	43.5	0.91
Cr^{6+}	0.03	37.1	0.98	0.01	49.26	0.98	0.07	55.56	0.8	0.15	54.05	0.78	0.15	43.47	0.92	0.19	38.91	0.95
Ni^{2+}	9.6	0.45	0.6	9.6	0.79	0.45	0.15	65.4	0.96	0.26	54.35	0.95	0.03	19.05	0.83	0.16	50.25	0.98
Pb^{2+}	0.91	7.30	0.75	-0.73	54.05	0.85	0.14	63.29	0.99	0.26	54.34	0.95	0.06	76.92	0.86	0.06	84.74	0.68

ZnO-SS seems to have the highest uptake capacity value of 84.74% followed by MnO-SS with Fe_3O_4-SS having the least values of 67.11% moreover, the starch modified Nano adsorbents proved to have more uptake capacity than the ordinary Nano adsorbents, corroborating the facts that more particle sizes and higher surface morphology of starch modified Nano adsorbents as observed earlier was responsible for the apparent high contaminant ion uptake. The energy of adsorption represented by K_L was highest in the adsorption of Ni^{2+} onto Fe_3O_4-SS and Fe_3O_4 with 9.6 values. K_L values for every other contaminant ion adsorption on the various adsorbents were observed at between 0,03 - 0.91.

4.5.2 Freundlich isotherm model

The adsorption data were also tested with Freundlich isotherm model and the outcome was shown on Figures 4.22a; 4.22b, 4.23a; 4.23b, 4.24a and 4.24b. Figure 4.22a, represents curves for adsorption of As^{3+}, Cd^{2+} and Ni^{2+} onto Fe_3O_4;Fe_3O_4-SS adsorbents. Adsorptions of Cr^{6+} and Pb^{2+} ions onto Fe_3O_4;Fe_3O_4-SS are shown on Figure 4.22b.

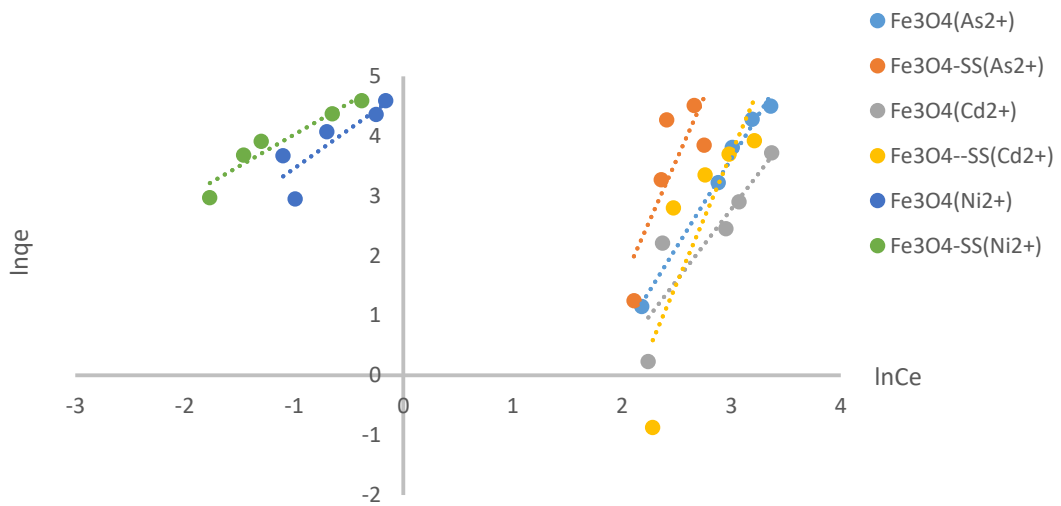

Figure 4.22a ; Freundlich isotherm for adsorption of As^{3+}, Cd^{2+} and Ni^{2+} ions on the Nano adsorbents prepared by Fe_3O_4 and Fe_3O_4-SS materials,

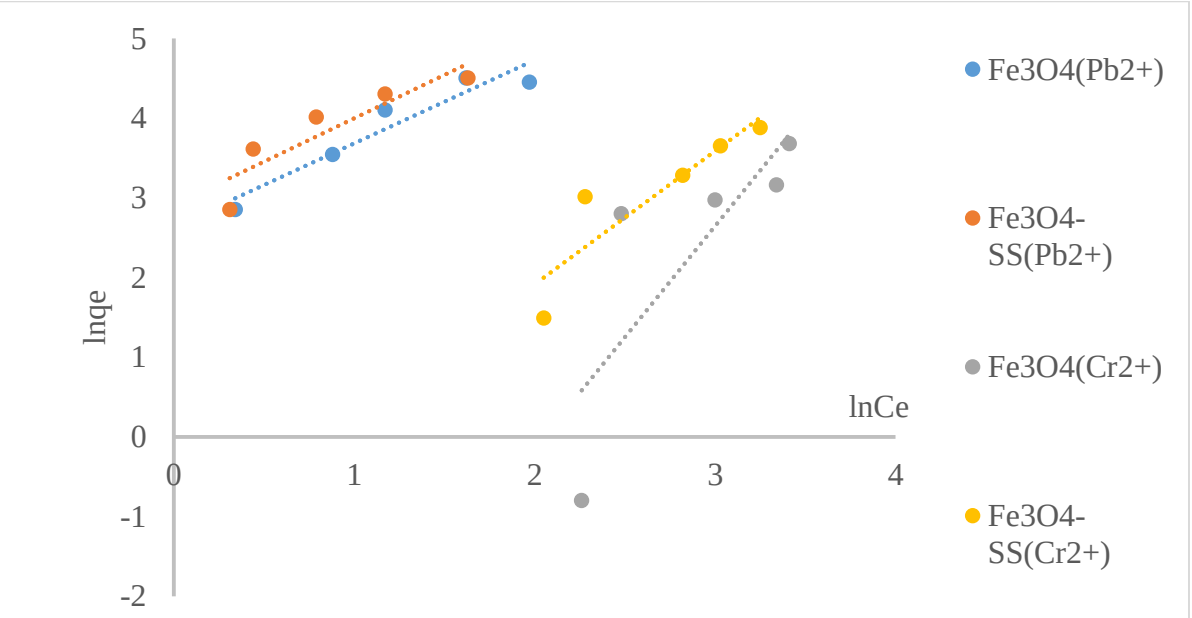

Figure 4.22b ; Freundlich isotherm for adsorption of Pb^{2+} and Cr^{6+} ions on the Nano adsorbents prepared by Fe_3O_4 and Fe_3O_4-SS materials

The Freundlich model curves representing adsorption of As^{3+}, Cd^{2+} and Cr^{6+} contaminant ions onto MnO; MnO-SS are shown on Figure4.24a, while that of Ni^{2+} and Pb^{2+} are displayed on Figure 4.24b

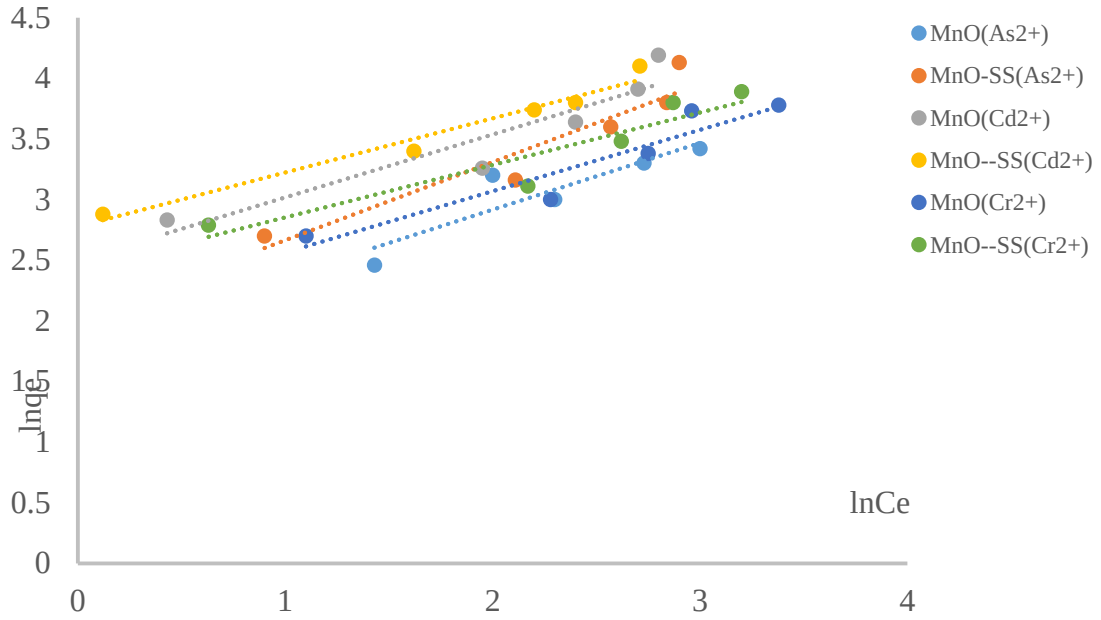

Figure 4.23a ; Freundlich isotherm for adsorption of As^{3+}, Cd^{2+} and Cr^{6+} ions on the Nano adsorbents prepared by MnO and MnO-SS materials

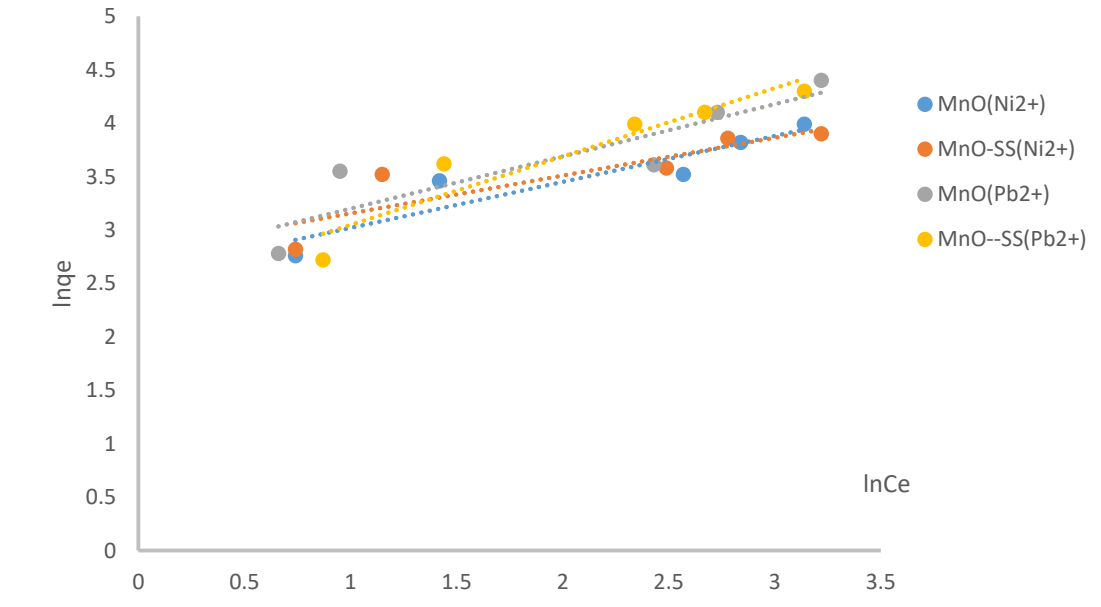

Figure 4.23b ; Freundlich isotherm for adsorption of Ni^{2+}, and Pb^{2+} ions on the Nano adsorbents prepared by MnO and MnO-SS materials

Also, Freundlich model plots showing adsorptions of As^{3+}, Cd^{2+} and Cr^{6+} contaminant ions onto ZnO; ZnO;-SS adsorbents are presented on Figure 4.25a.

Adsorption of Ni^{2+} and Pb^{2+} contaminant ions onto ZnO; ZnO;-SS are represented on Figure 4.25b

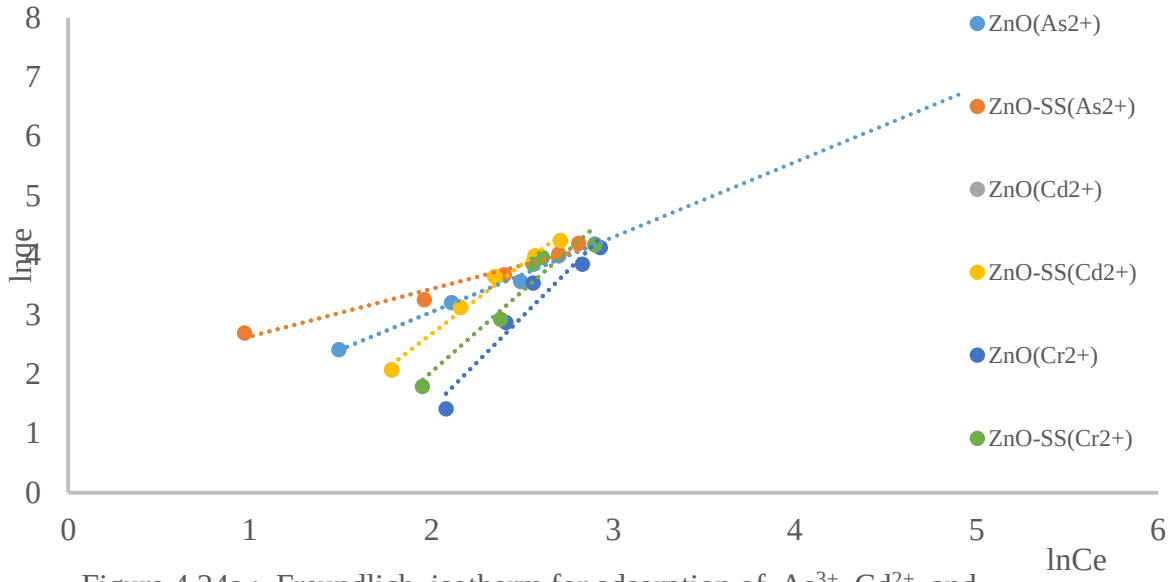

Figure 4.24a ; Freundlich isotherm for adsorption of As^{3+}, Cd^{2+}, and Cr^{6+} ions on the Nano adsorbents prepared by ZnO and ZnO-SS materials

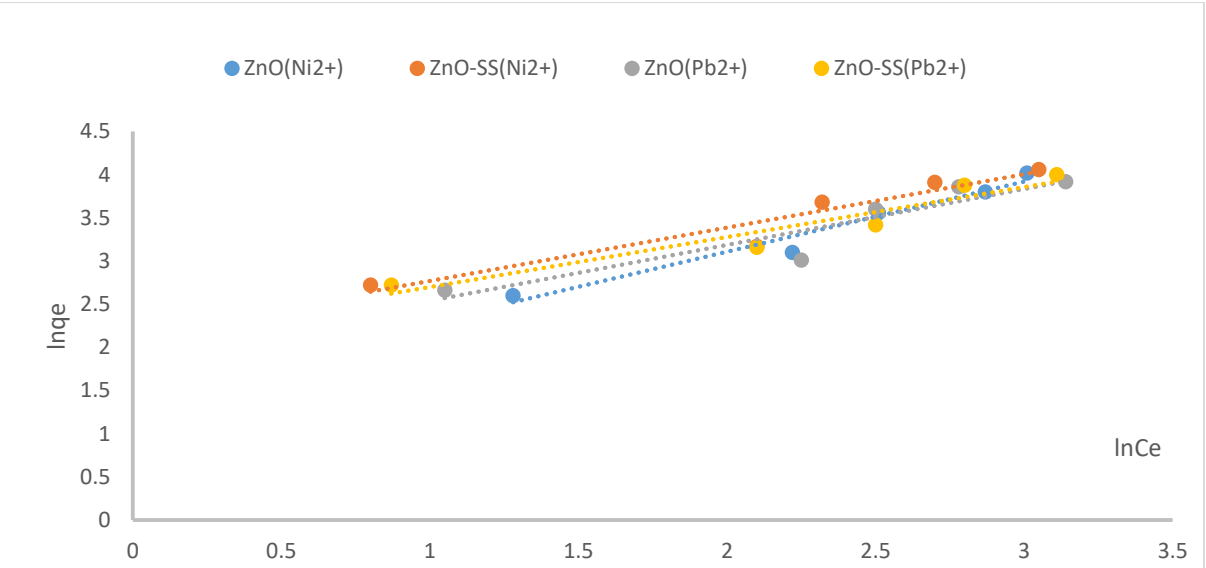

Figure 4.24b; Freundlich isotherm for adsorption of Ni^{2+} and Pb^{2+} ions on the Nano adsorbents prepared by ZnO and ZnO-SS materials

From the Figures, Freundlich adsorption isotherm model also showed a good fit with the adsorption data at appreciable coefficient of determination (R^2) values ranging from 0.5 - 0.98. However, the coefficient values were highest in adsorption of contaminant ions onto ZnO; ZnO-SS adsorbents, followed by MnO; MnO-SS with Fe_3O_4; Fe_3O_4-SS having the lowest values. This work showed conformity of Freundlich isotherm model with the contaminant ions' adsorption data which gave an indication that; adsorption of contaminant ions' onto Fe_3O_4; Fe_3O_4-SS, MnO; MnO-SS and ZnO; ZnO-SS Nano adsorbents experienced a multi-layer coverage on a heterogeneous surface. This observation is in agreement with that which was reported by Motsi et al. (2009) that nano adsorbents experience multi-layer coverage on heterogeneous surface and that no adsorption site has equal energy of adsorption, implying that energy of adsorption is irregular as reported by Prasad et al., (2008) and Gunay et al. (2007). Freundlich model paramters shown on Table 4.5 revealed that K_F and n values are highest in adsorption of contaminant ions on MnO:MnO-SS Nano adsorbents.

Table- 4.5: Freundlich parameters for adsorption of As^{3+}, Cd^{2+}, Cr^{6+}, Ni^{2+} and Pb^{2+} contaminant ions onto Nano adsorbents of ordinary and starch modified metal oxides

	Freundlich																
	Fe_3O_4			Fe_3O_4-SS			MnO			MnO-SS			ZnO			ZnO-SS	
	K_F	n	R^2	K_F	n	R^2	K_F	N	R^2	K_F	n	R^2	K_F	n	R^2	K_F	n
As^{3+}	-14.22	0.34	0.98	-18.4	0.24	0.5	5.59	1.82	0.81	5.49	1.55	0.9	1.41	0.79	0.99	4.96	1.25
Cd^{2+}	-11.91	0.42	0.78	0.87	-25.3	0.68	6.80	1.93	0.8	7.54	2.24	0.87	-1.08	0.72	0.84	-5.58	0.43
Cr^{6+}	-15.49	0.36	0.6	-3.88	0.6	0.8	5.59	1.98	0.9	6.57	2.31	0.88	-12.9	0.34	0.98	-9.25	0.37
Ni^{2+}	12.93	0.77	0.7	13.78	0.95	0.9	7.0	2.32	0.8	6.55	2.82	0.77	4.03	1.23	0.96	5.85	1.6
Pb^{2+}	6.42	0.95	0.9	7.88	0.91	0.8	7.37	2.0	0.8	6.55	1.56	0.89	5.14	1.54	0.87	5.75	1.73

Adsorption of Ni^{2+} and Pb^{2+} were highest by all the adsorbents and the level of adsorption capacity and intensity of adsorption were observed to be higher in starched modified metal oxide Nano adsorbents than the ordinary adsorbents. The scenario could be attributed to large particles sizes and surface area associated with starch modified Nano adsorbents.

4.5.3 Temkin Isotherm Model

Temkin isotherm model was also adopted to further quantify the adsorption of contaminant ions onto metal oxide Nano adsorbents of starch and non-starch constituents. Temkin model curves of contaminant ion amounts on the adsorbents at equilibrium (qe) against the natural log of the contaminant ions remaining in solution after adsorption process (lnCe) for adsorptions of As^{3+}, Cd^{2+}, Cr^{6+}, $Ni^{2+}$and Pb^{2+} contaminant ions on Fe_3O_4:Fe_3O_4-SS adsorbents are shown on Figures 4.25a and 4.25b, Temkin adsorptions curve for As^{3+} and Cd^{2+} whereas Figure 4.26b shows that of Cr^{6+}, $Ni^{2+}$and Pb^{2+}

.

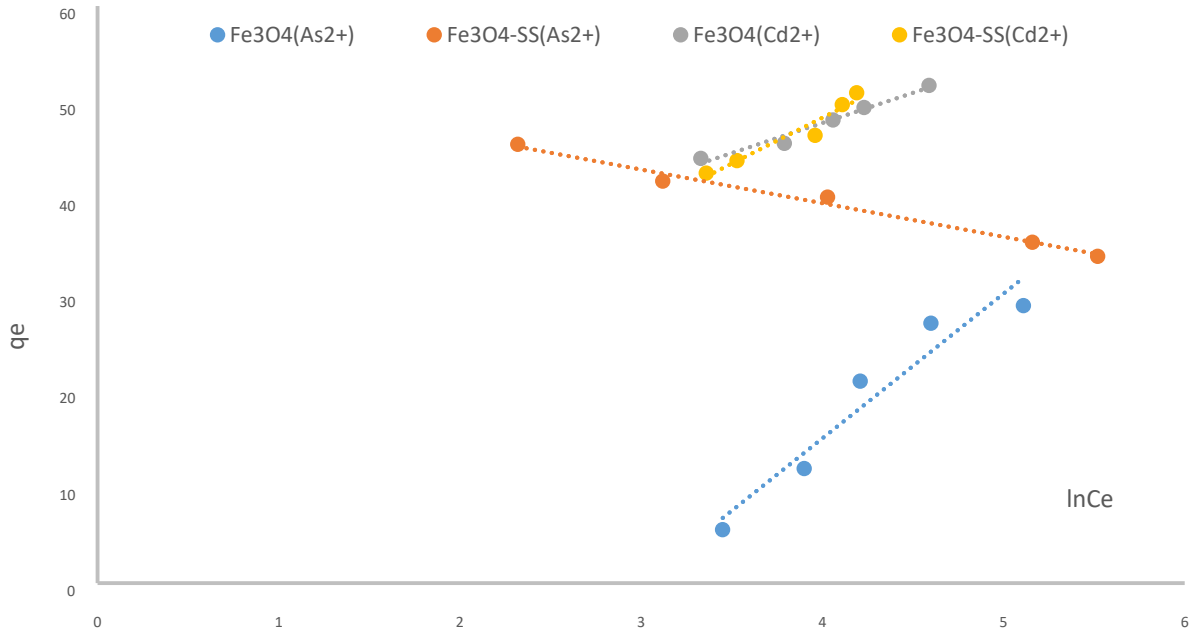

Figure 4.25a; Temkin isotherm for adsorption of As^{3+} and Cd^{2+} ions on the Nano adsorbents prepared by Fe_3O_4 and Fe_3O_4-SS materials

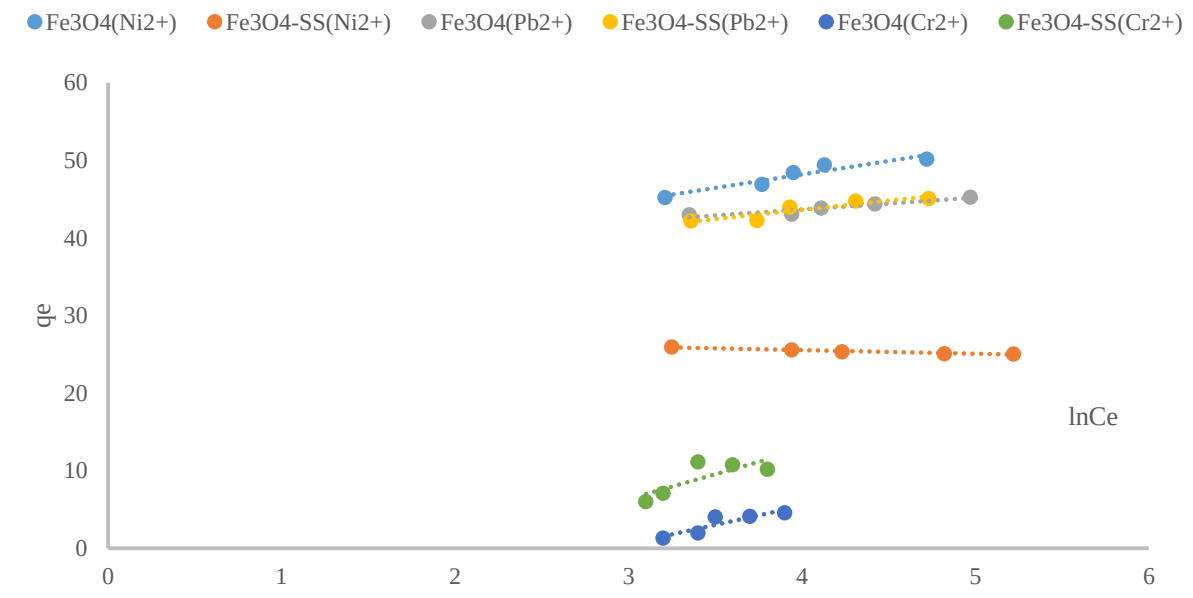

Figure 4.25b; Temkin isotherm for adsorption of Ni^{2+}, Pb^{2+} and Cr^{6+} ions on the Nano adsorbents prepared by Fe_3O_4 and Fe_3O_4 -SS materials

Results of adsorption of the contaminant ions on MnO: MnO-SS and ZnO: ZnO-SS adsorbents as also quantified by Temkin isotherm model are represented on Figure4.26a and 4.26b and Figures 4.27a and 4.27b respectively .

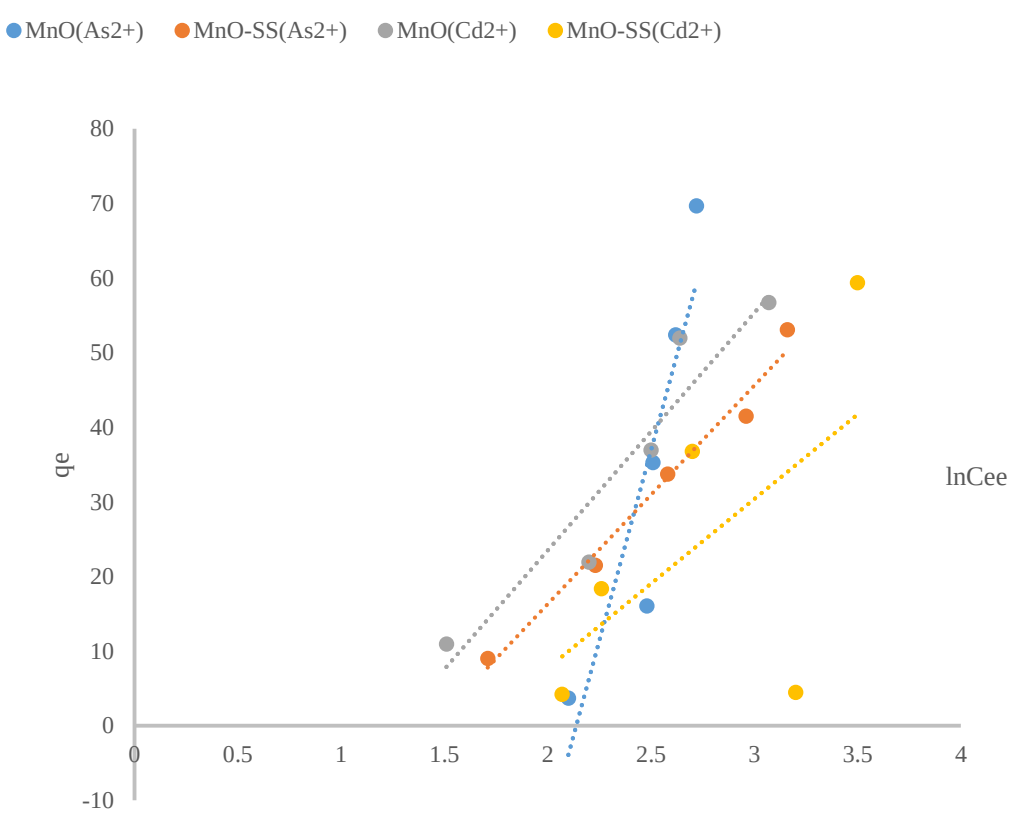

Figure 4.26a; Temkin isotherm for adsorption of As^{3+} and Cd^{2+} ions on the Nano adsorbents prepared by MnO and MnO-SS materials

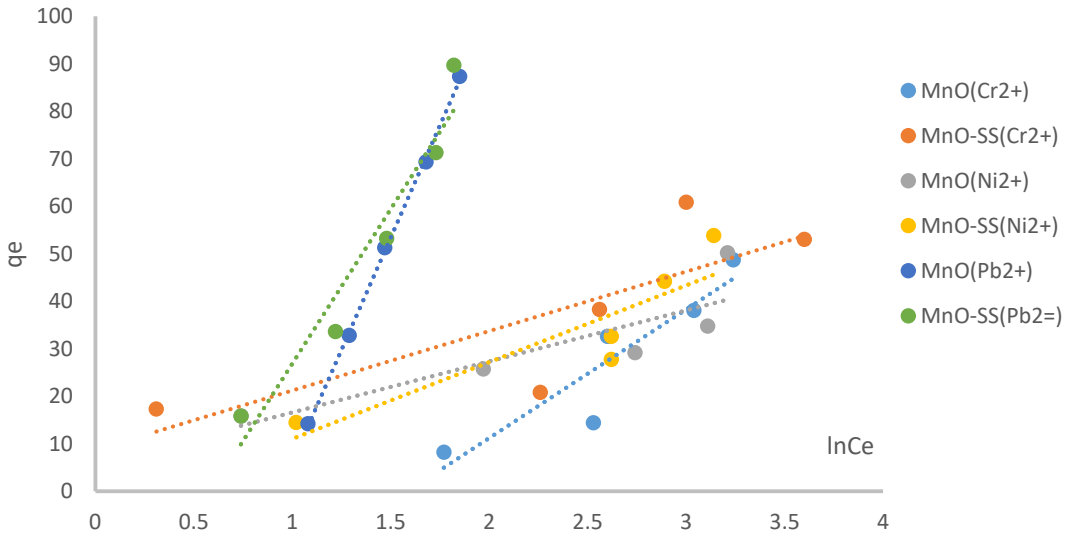

Figure 4.26b; Temkin isotherm for adsorption of Cr^{6+}, Pb^{2+} and Ni^{2+} ions on the Nano adsorbents prepared by MnO and MnO-SS materials

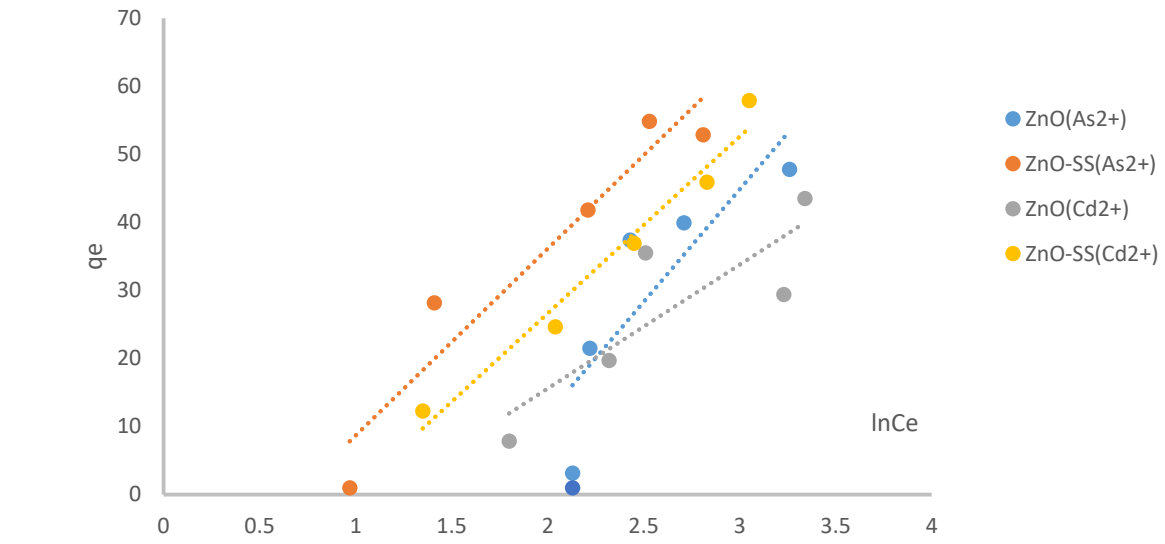

Figure 4.27a; Temkin isotherm for adsorption of As^{3+} and Cd^{2+} ions on the Nano adsorbents prepared by ZnO and ZnO-SS materials

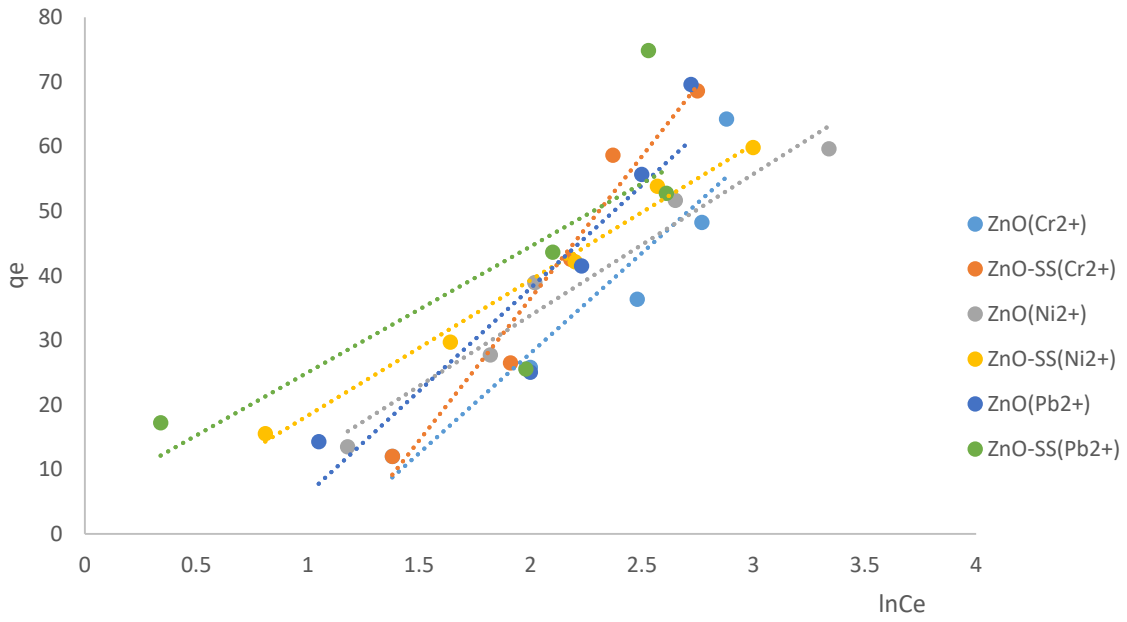

Figure 4.27b; Temkin isotherm for adsorption of Cr^{6+}, Ni^{2+} and Pb^{2+} ions on the Nano adsorbents prepared by ZnO and ZnO-SS material

Table 4.6; Showing Temkin model parameters for adsorption of the contaminant ions on various Nano adsorbents.

	Temkin																	
	Fe_3O_4			Fe_3O_4-SS			MnO			MnO-SS			ZnO			ZnO-SS		
	K_T	Bi	R2	K_T	Bi	R2	K_T	Bi	R2	K_T	Bi	R2	K_T	Bi	R2	K_T	Bi	R2
As^{3+}	27.47	5.8	0.9	74.51	26.14	0.6	593.3	101.9	0.8	115	29.3	0.9	147.77	33.07	0.72	51.02	27.44	0.92
Cd^{2+}	138.5	32.1	0.8	82.45	2.4	0.8	109.9	31.84	0.9	102	22.68	0.96	56.73	18.21	0.72	69.91	25.97	0.97
Cr^{6+}	57.27	18.72	0.68	28.13	16.3	0.8	117.1	21.15	0.84	-23.8	12.5	0.65	92.39	30.98	0.91	140.16	44.01	0.96
Ni^{2+}	106.83	29.6	0.74	70	27.0	0.8	-15.94	10.74	0.75	13.93	16.15	0.78	27.02	21.90	0.96	7.39	20.99	0.99
Pb^{2+}	87.14	31.89	0.52	-6.11	18.98	0.6	240.3	94.55	0.99	104.27	65.15	0.94	69.81	31.86	0.85	-14.90	19.51	0.62

Estimated parameters derived from Temkin model are displayed on Table 4.6. The plots show linear curves with coefficients of correlation (R^2) hovering between 0.52 to 0.99, suggesting reasonable fit of the model to the data obtained during the process of adsorption. However, temkin model fits most for ion contaminant adsorptions on ZnO-SS adsorbent which is proven by high correlation coefficient values with adsorbing contaminant ions (As^{3+}, Cd^{2+}, Cr^{6+}, Ni^{2}+, Pb^{2+}). Generally, Temkin model fits the experimental data in the following order; ZnO-SS > MnO > MnO-SS > ZnO> Fe_3O_4-SS and Fe_3O_4.

Table 4.6, Bi and KT represents the heat of adsorption and maximum binding energy respectively vary with various adsorbing contaminant ions and the adsorbents. K_T values were observed to be 593.30 which was the highest for the adsorbing contaminant ions on MnO adsorbent and decreased as follows; MnO > MnO-SS > Fe_3O_4. > ZnO > ZnO-SS > Fe_3O_4-SS. The prevailing K_T variations imply that maximum binding energies effects of the contaminant ions on various adsorbents follow the same trend. That is, the binding energies of the contaminant ions on the adsorbents decreased from MnO down to Fe_3O_4-SS adsorbent. Among the contaminant ions, As^{3+} and Pb^{2+} exhibited the highest binding force on the MnO adsorbent with K_T values of 593.3 and 240 respectively. This observation is a proof of high level of affinity of the contaminant ions to the adsorbents as was also reported in the work of Chiou & Li (2002) and that of Singh and Pant (2006). Glaring variation of Bi which indicates heat of adsorption of the contaminant ions on the adsorbents was also observed. Bi values varied almost in the same manner with K_T. This means that heat of adsorption of the contaminant ions on various adsorbents decreased as follows; MnO > MnO-SS > Fe_3O_4. > ZnO > ZnO-SS > Fe_3O_4-SS. With the Bi values of 101.9 and 95.55 for As^{2+} and Pb^{2+} respectively, heat of adsorption produced in adsorption process of the aforementioned ions onto MnO adsorbent was also high (Banerjee & Chattopadhyaya 2013). It also suggests that As^{2+} and Pb^{2+} have stronger interaction with MnO adsorbent than other adsorbents indicating

that other contaminant ions with low Bi values show weak interaction with their respective adsorbents (Lakshmipathy & Sarada 2015).

4.6 Adsorption Kinetic Modelling

Adsorption kinetics of the contaminant ions onto various nano adsorbents were investigated using pseudo first order model, second order model, Elovich model, Ritchie Model and sticking probability model. These kinetic models describe the rate of adsorption of contaminant ions (As^{3+}, Cd^{2+}, Cr^{6+}, Ni^{2+} and Pb^{2+}) on the Nano adsorbents relating with time to ascertain the physical, chemical status of the adsorption processes and conformity of the obtained data with the kinetic models.

4.6.1 Pseudo First Order Model

Results of testing the obtained data through adsorption processes of As^{3+}, Cd^{2+}, Cr^{6+}; Ni^{2+} and Pb^{2+} contaminant ions onto Fe_3O_4: Fe_3O_4-SS, MnO: MnO-SS and ZnO: ZnO-SS adsorbents with pseudo first order (PFO) model were depicted in Figures 4. 28a, -4.28b-, 4.29a-, 4.29b, 4.30a and 4.30b respectively. The results of levels of fitting of the obtained data with PFO model and other estimated parameters were shown on Table 4.7a and 4.7b. Figures 4. 29a and 4.29b show linear curves otherwise referred to as PFO model curves with various levels of conformity with the data for adsorption of As^{3+} and Cd^{2+} and Cr^{6+}, Ni^{2+} and Pb^{2+}contaminant ions respectively on Fe_3O_4: Fe_3O_4-SS adsorbents

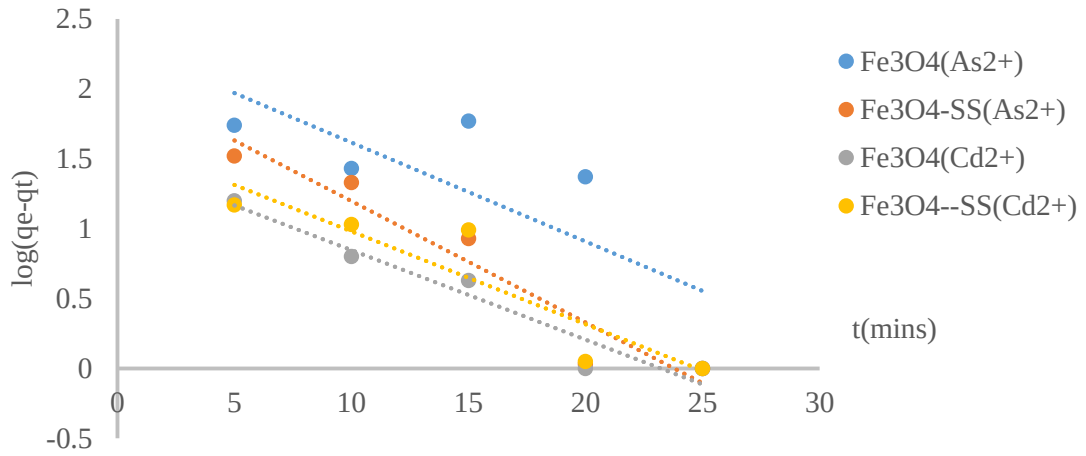

Figure 4.28a ; plot of pseudo-first order model for adsorption of As^{3+} and Cd^{2+} onto Nanoadsorbents prepared by Fe_3O_4 and Fe_3O_4 -SS maerials

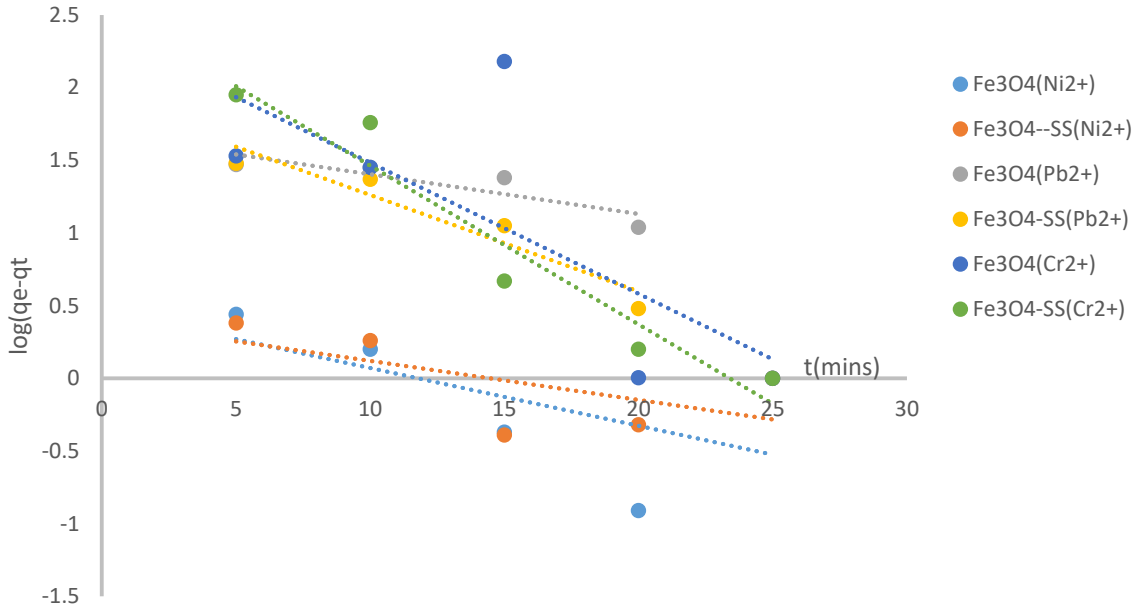

Figure 4.28b ; plot of pseudo-first order model for adsorption of Ni^{2+} , $Cr^{6+}$and Pb^{2+} onto Nanoadsorbents prepared by Fe_3O_4 and Fe_3O_4-SS maerials

Table 4.7a Pseudo-first order model parameters for adsorption of the contaminant ions onto Nano adsorbents prepared by Fe4O3 and Fe4O3-SS material

	$q_{e(exp)}$ (mg/g)	$q_{e(cal)}$ (mg/g)	K_1 (g/mgmin	R^2	$q_{e(exp)}$ (mg/g)	$q_{e(cal)}$ (mg/g)	K_1 (g/mgmin	R^2
As^{3+}	82.13	201.86	0.16	0.59	84.83	115.87	0.2	0.92
Cd^{2+}	92.50	30.62	0.15	0.93	95.95	44.01	0.15	0.84
Cr^{6+}	94.29	346.74	0.30	0.6	99.85	358.10	0.25	0.93
Ni^{2+}	99.99	0.92	0.1	0.35	100.76	2.44	0.06	0.39
Pb^{2+}	127.93	118.30	0.15	0.73	129.27	120.50	0.18	0.95

The conformity between the experimental data and the models was expressed by the correlation coefficients and agreement between experimental ($q_{e(exp)}$ and calculated ($q_{e(cal)}$) values of the contaminant ions adsorbed by various adsorbents at equilibrium. From Table 4.7a, correlation coefficient values(R^2) for adsorption of the contaminant ions on Fe_3O_4 and Fe_3O_4-SS were within the ranges of 0.35 - 0.93 and 0.39 - 0.95.

The apparent higher R^2 values of Fe_3O_4 of lead (Pb^{2+}) and closer relationships between at $q_{e(exp)}$ (127.30) and $q_{e(cal)}$ (118.30) observed imply that adsorption process of the contaminant ions on Fe_3O_4-SS complies with PFO model better than that of Fe_3O_4 adsorbent. However, the least compliance was observed at Ni^{2+} adsorption on Fe_3O_4 whereas the highest compliance was observed at adsorption of Pb^{2+} on Fe_3O_4-SS.

Results obtained from fitting the adsorbed contaminant ions on MnO and MnO-SS on the PFO model showed linear curves as depicted on Figures 4.30a - and 4.30b

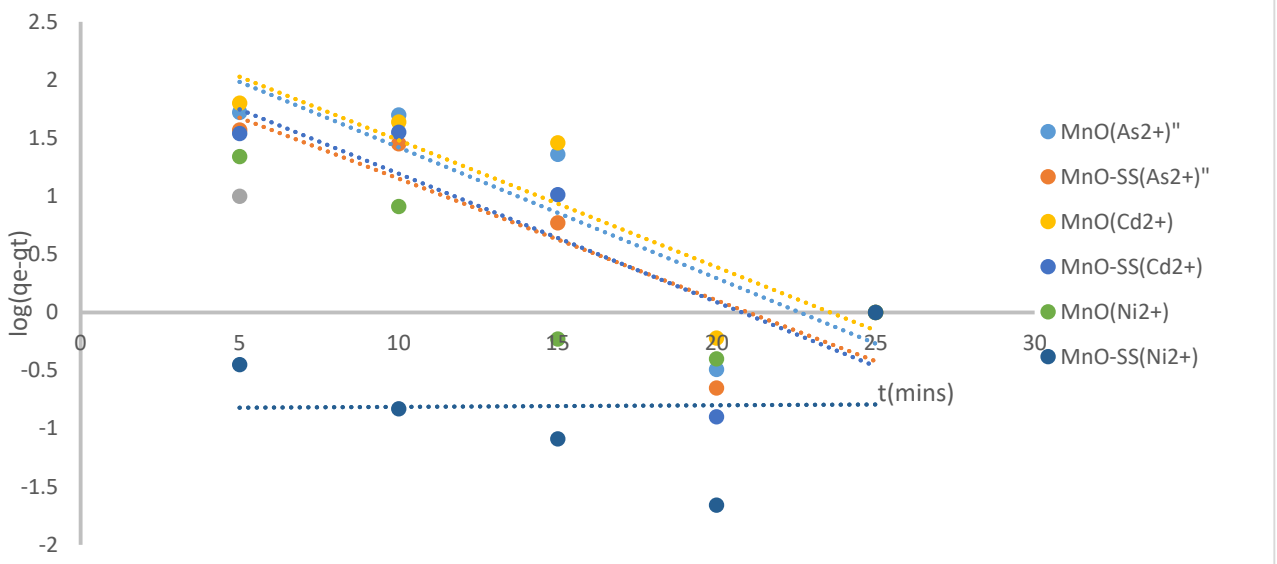

Figure 4.29a ; plot of pseudo-first order model for adsorption of As^{3+}, Cd^{2+} and Ni^{2+} onto Nanoadsorbents prepared by MnO and MnO-SS maerials

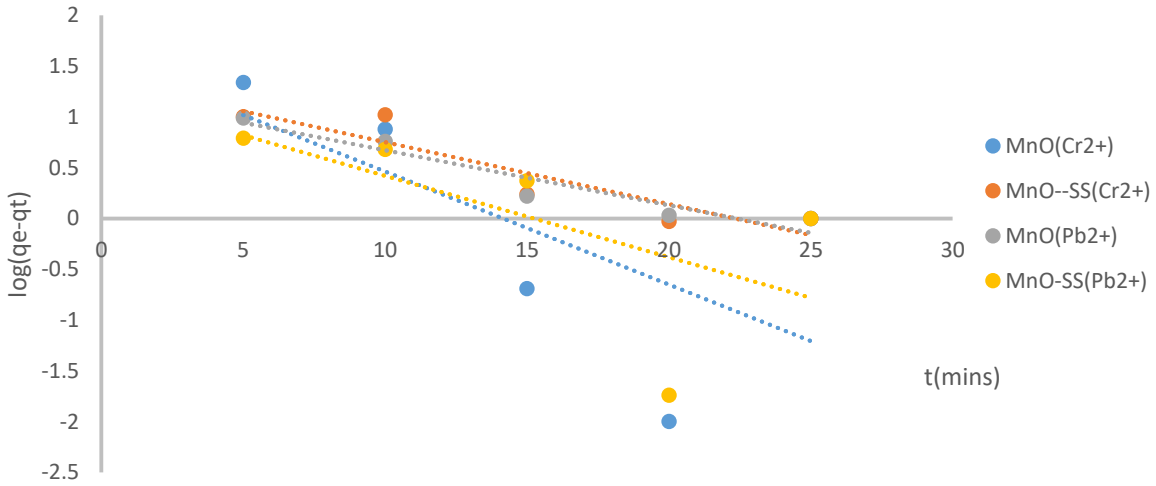

Figure 4.29b ; plot of pseudo-first order model for adsorption of Cr^{6+} and Pb^{2+} onto Nanoadsorbents prepared byMnO and MnO-SS materials

The estimated PFO model parameters are shown on Table4.7b. Slight variation was observed regarding values of correlation coefficients, experimented ($q_{e(exp}$) and calculated contaminant ions amounts at equilibrium from the model($q_{e(cal)}$), and levels of conformity with PFO model in adsorption of contaminant ions on MnO; MnO-SS.

Table 4.7b Pseudo-first order model parameters for adsorption of the contaminant ions onto Nano adsorbents prepared by MnO; MnO-SS.and ZnO; ZnO-SS materials

	MnO				MnO-SS			
	$q_{e(exp)}$ (mg/g)	$q_{e(cal)}$ (mg/g)	K_1 (g/mgmin	R^2	$q_{e(exp)}$ (mg/g)	$q_{e(cal)}$ (mg/g)	K_1 (g/mgmin	R^2
As^{3+}	85.94	352.37	0.26	0.74	52.93	158.49	0.25	0.76
Cd^{2+}	71.92	374.97	0.25	0.80	40.30	199.53	0.26	0.67
Cr^{6+}	71.52	39.81	0.26	0.44	94.83	22.91	0.14	0.84
Ni^{2+}	71.91	33.19	0.18	0.69	99.89	96.33	0.13	0.91
Pb^{2+}	95.83	9 6.33	0.13	0.91	90.11	18.62	0.18	0.39
	ZnO				ZnO-SS			
	$q_{e(exp)}$ (mg/g)	$q_{e(cal)}$ (mg/g)	K_1 (g/mgmin	R^2	$q_{e(exp)}$ (mg/g)	$q_{e(cal)}$ (mg/g)	K_1 (g/mgmin	R^2
As^{3+}	49.68	132.74	0.23	0.78	94.29	71.12	0.21	0.71
Cd^{2+}	77.53	85.90	0.20	0.85	89.58	47.53	0.17	0.87
Cr^{6+}	83.37	92,26	0.20	0.77	70.50	20.14	0.12	0.96
Ni^{2+}	99.03	15.85	0.16	0.45	99.89	7.6	0.09	0.76
Pb^{2+}	89.0	11.32	0.12	0.81	94.20	24.60	0.17	0.5

The correlation coefficients for the two aforementioned adsorbents were observed to be in the following range; 0.44 - 0.91 and 0.39 - 0.91 respectively and also observed to be smaller than that of adsorption of contaminant ions on Fe_3O_4 and Fe_3O_4-SS adsorbents. $q_{e(cal)}$ and $q_{e(exp}$ values for MnO ; MnO-SS equally showed wider gaps than the values observed for Fe_3O_4 and Fe_3O_4-SS. Likewise, description of adsorption of the contaminant ions (As^{3+} and Cd^{2+} and Cr^{6+}, Ni^{2+} and Pb^{2+}) ZnO:ZnO-SS adsorbents by PFO kinetic model produced linear curves as shown in Figures4.31a and4.31b

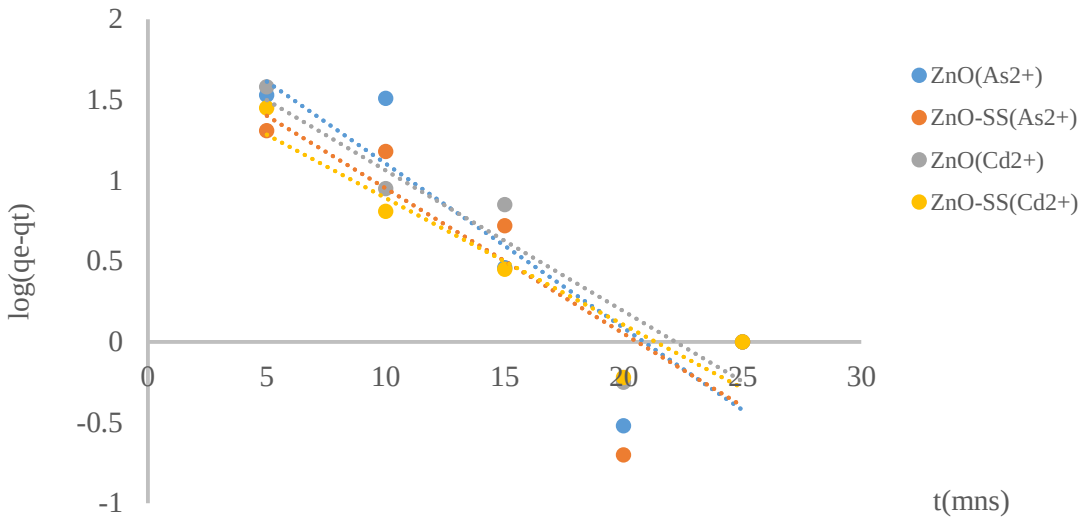

Figure 4. 30a ; plot of pseudo-first order model for adsorption of As^{3+} and Cd^{2+} onto Nanoadsorbents prepared byZnO and ZnO-SS materials

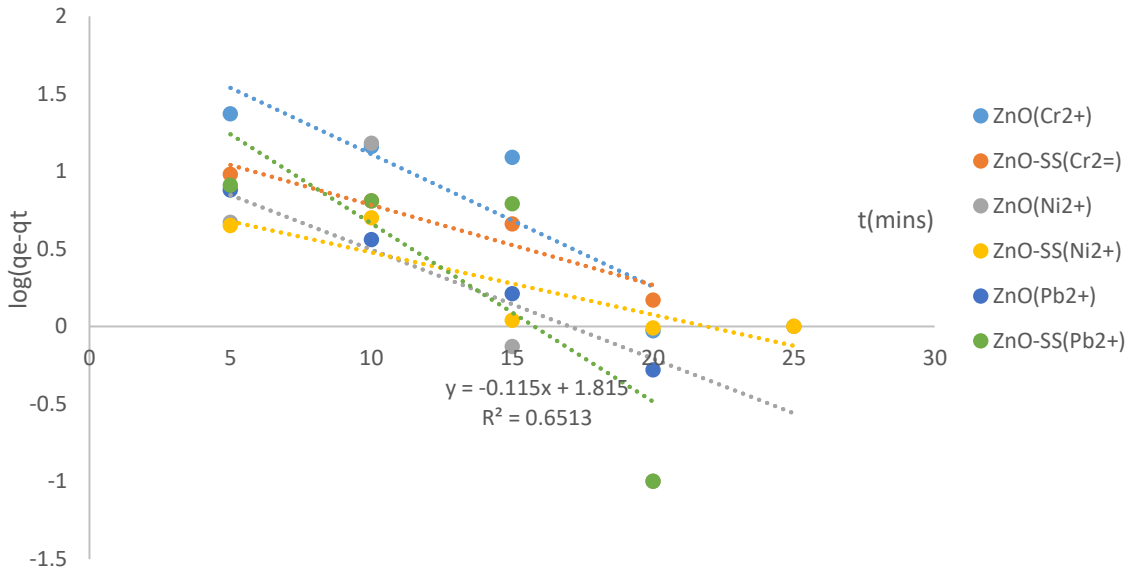

Figure 4. 30b ; plot of pseudo-first order model for adsorption of Cr^{6+}, Ni^{2+} and Pb^{2+} onto Nanoadsorbents prepared byZnO and ZnO-SS materials

The PFO model parameters which includes the correlation coefficient (R^2), rate of adsorption of various contaminant ions on ZnO; ZnO-SS adsorbents, (K_1), adsorption capacity values estimated from the model ($q_{e(cal)}$) and that obtained from experiment at equilibrium ($q_{e(exp)}$) are also represented on Table 4.7b. The fit between adsorption kinetics of contaminant ions onto ZnO; ZnO-SS and the PFO model is reasonably good with correlation coefficient (R^2) of 0.96 which was almost in the same range with the adsorption process of contaminant ions on MnO; MnO-SS adsorbents. However, higher R^2 and K_1 values and value ranges of $q_{e(cal}$ and $q_{e(exp)}$ closer in adsorption processes of the contaminant ions on ZnO-SS adsorbent than on ZnO and MnO; MnO-SS suggest that PFO model describes the adsorption processes of the ions on ZnO-SS better than the adsorption processes on ZnO and MnO; MnO-SS. Generally, data obtained from adsorption processes of contaminant ions on Fe_3O_4 and Fe_3O_4-SS adsorbents conform most with PFO kinetic model having had highest R^2 and K_1 values and highest $q_{e(cal)\ values}$ with closest value range of $q_{e(cal)}$ and $q_{e(exp)}$.

4.6.2 Pseudo Second Order (PSO) Model

Also, data obtained from adsorption processes of the contaminant ions onto the nano adsorbents of Fe_3O_4: Fe_3O_4-SS, MnO: MnO-SS and ZnO: ZnO-SS were simulated with pseudo second order (PSO) model to produce PSO kinetic model linear curves (Figures 4.31a and-4.31b, Figures 4.32a and 4.32b, and Figures 4.33a and 4.33b for Fe_3O_4:Fe_3O_4-SS, MnO: MnO-SS and ZnO: ZnO-SS adsorbents respectively) .

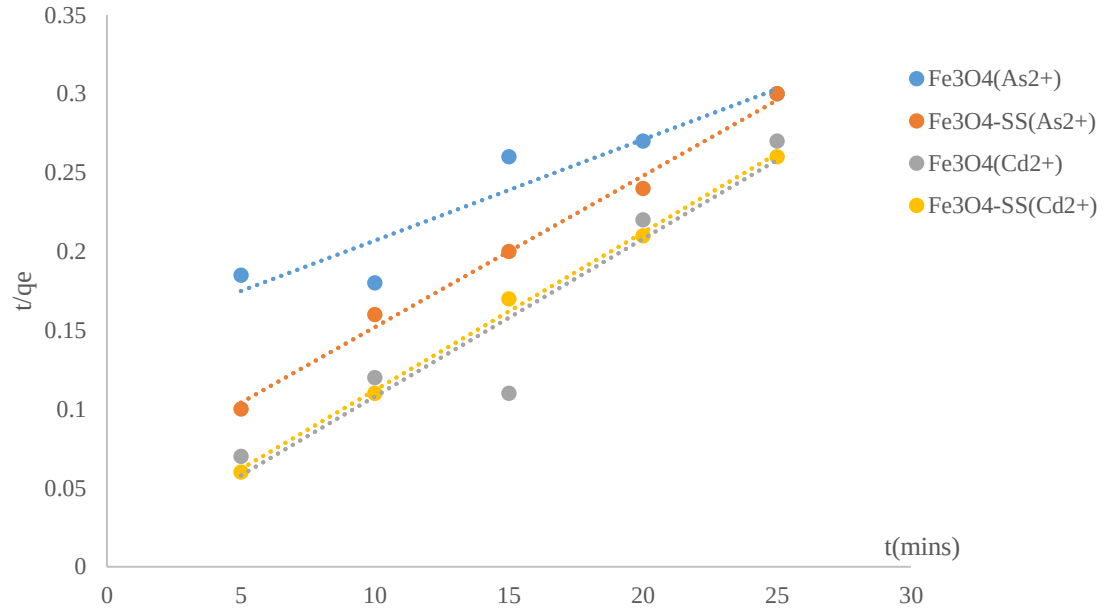

Figure 4.31a ; plot of pseudo-second t order model for adsorption of As^{3+} and Cd^{2+} onto Nanoadsorbents prepared by Fe_3O_4 and Fe_3O_4-SS maerials

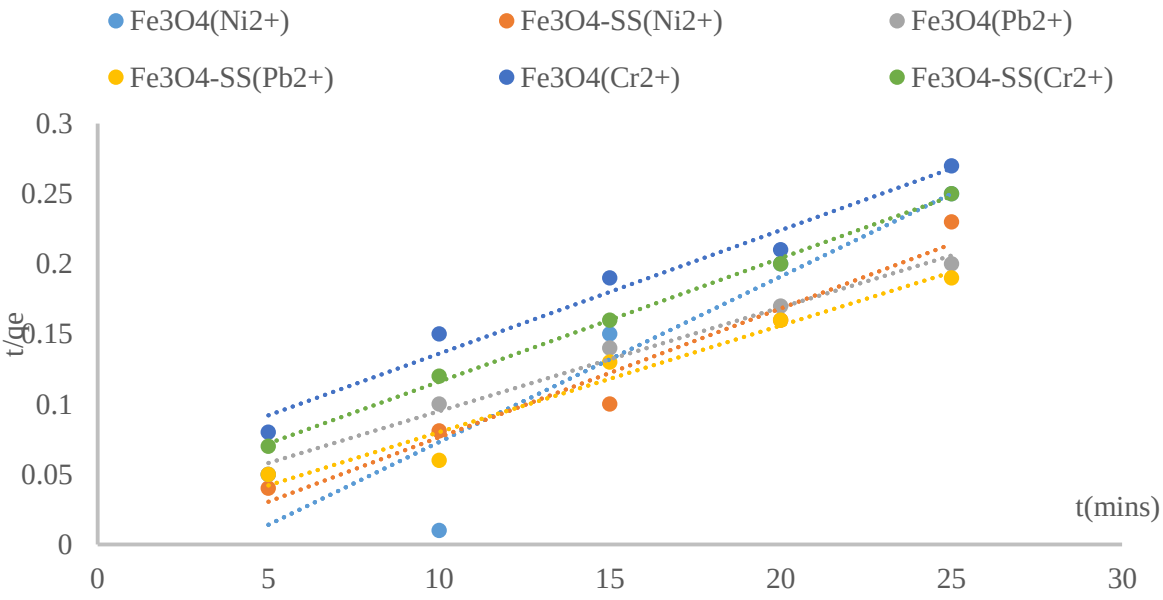

Figure 4.31b ; plot of pseudo-second t order model for adsorption of Cr^{6+}, Ni^{2+} and Pb^{2+} onto Nanoadsorbents prepared by Fe_3O_4 and Fe_3O_4-SS maerials

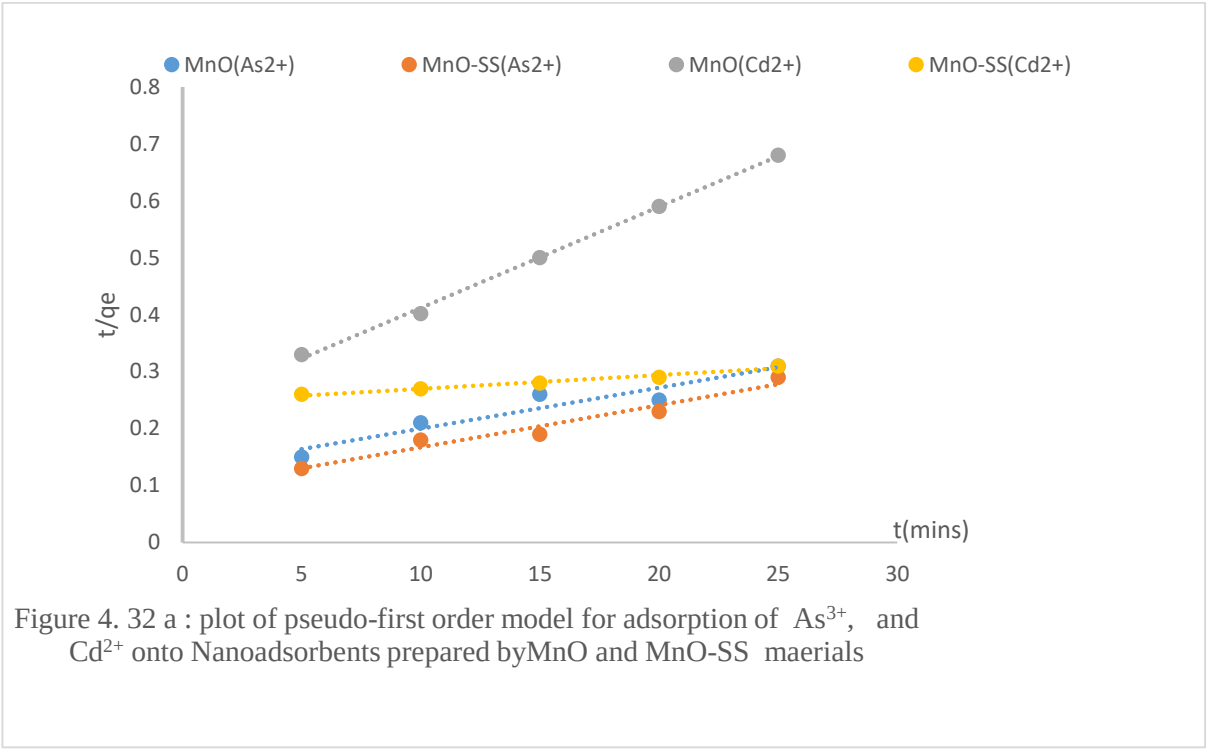

Figure 4. 32 a : plot of pseudo-first order model for adsorption of As^{3+}, and Cd^{2+} onto Nanoadsorbents prepared byMnO and MnO-SS maerials

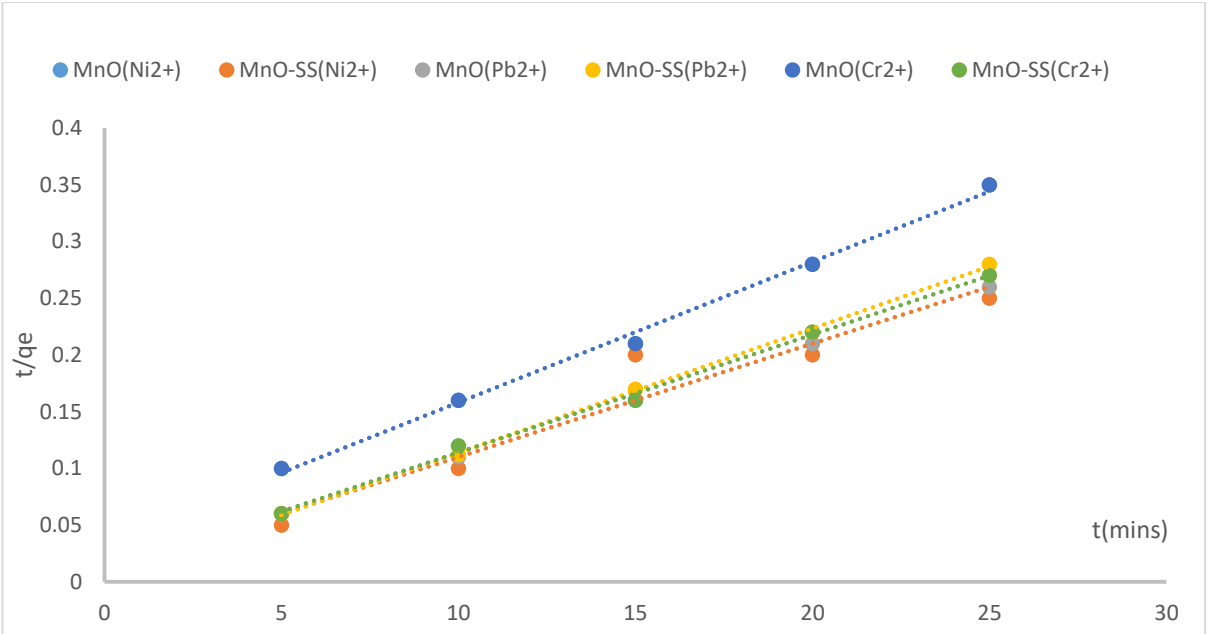

Figure 4. 32 b ; plot of pseudo-first order model for adsorption of Cr^{6+}, Pb^{2+} and Ni^{2+}onto Nanoadsorbents prepared byMnO and MnO-SS maerials

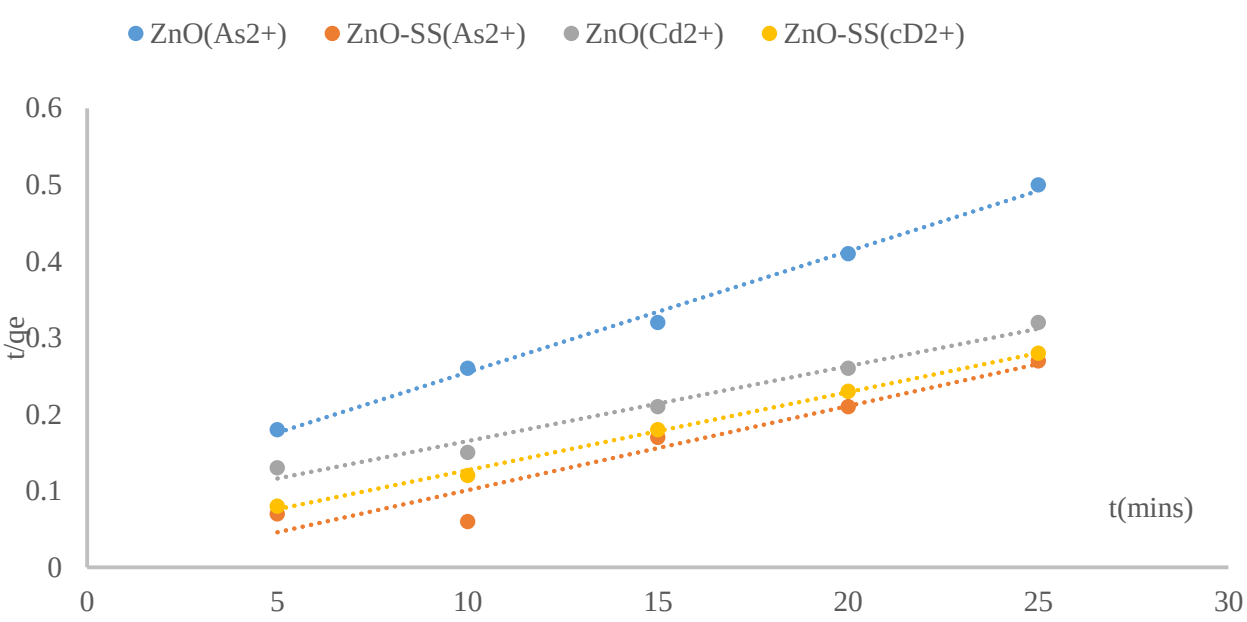

Figure 4. 33 a ; plot of pseudo-first order model for adsorption of As^{3+} and Cd^{2+} onto Nanoadsorbents prepared byZnO and ZnO-SS materials

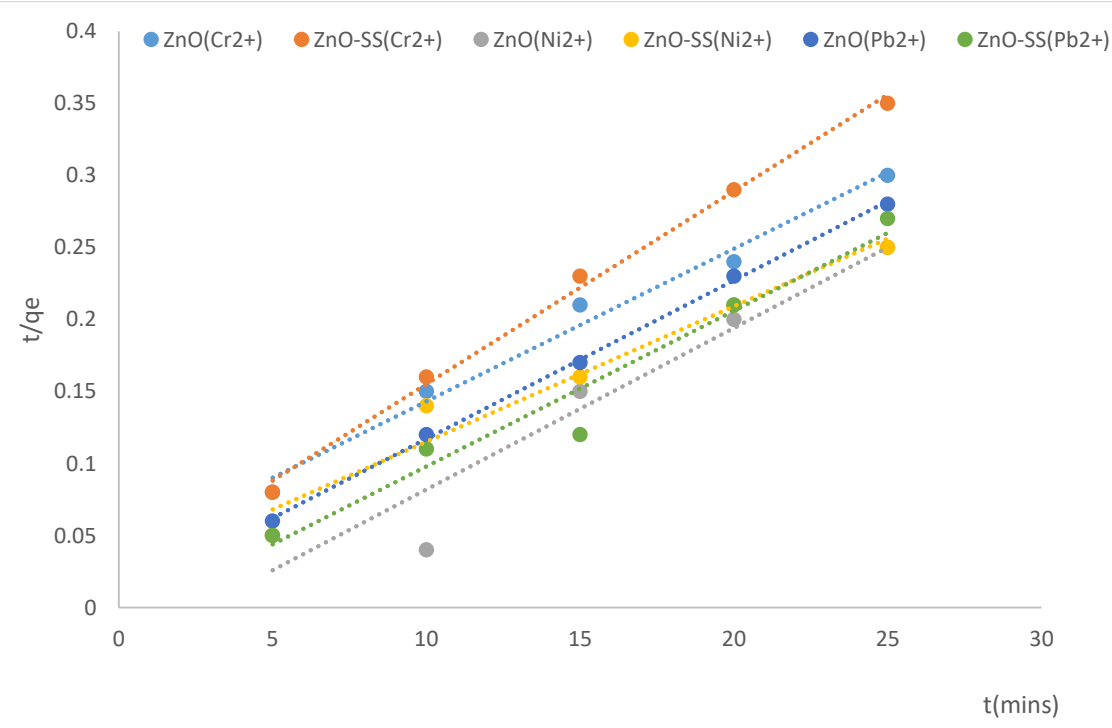

Figure 4. 33b ; plot of pseudo-first order model for adsorption of Cr^{6+} , Ni^{2+} and Pb^{2+} onto Nanoadsorbents prepared byZnO and ZnO-SS materials

Values of coefficient of correlation (R^2), adsorption rate constant (K_2), rate of initial concentrations (ho) and adsorption capacity of various contaminant ions on the respective adsorbents at equilibrium ($q_{e(cal)}$) and the equilibrium capacity obtained from the experiment ($q_{e(exp}$) are all presented on Table4.8

Table 4.8 Pseudo-first order model parameters for adsorption of the contaminant ions onto Nano adsorbents prepared by Fe_3O4:Fe_3O_4-SS, MnO; MnO-SS. and ZnO; ZnO-SS materials

	Pseudo- second order (PSO)									
	Fe_3O_4					Fe_3O_4-SS				
	qe(exp)(mg/g)	$q_{e(cal)}$ (mg/g)	h_O	R^2	K_2	qe(exp)(mg/g)	$q_{e(cal)}$ (mg/g)	h_O	R^2	K_2
As^{3+}	82.13	125	6.67	0.88	0.0002	84.83	111.11	16.39	0.99	0.001
Cd^{2+}	92.50	108.70	35.71	0.92	0.003	95.95	98.04	142.86	0.99	0.015
Cr^{6+}	94.29	125	20.83	0.98	0.001	99.85	113.63	40	0.99	0.003
Ni^{2+}	99.99	100	25	0.68	0.002	100.76	111.11	357.14	0.99	0.03
Pb^{2+}	127.93	142.96	47.61	0.98	0.002	129.27	166.67	37.03	0.98	0.001
	MnO					MnO-SS				
	qe(exp)(mg/g)	$q_{e(cal)}$ (mg/g)	h_O	R^2	K_2	qe(exp)(mg/g)	$q_{e(cal)}$ (mg/g)	h_O	R^2	K_2
As^{3+}	52.933	3.96	0.17	0.78	0.01	85.942	135.14	10.75	0.95	0.0006
Cd^{2+}	71.915	384.61	0.07	0.99	3.07	40.299	135.14	1.08	0.9	4.90006
Cr^{6+}	71.518	83.33	29.41	0.99	0.004	94.831	102.04	66.67	0.99	0.006
Ni^{2+}	71.911	80.66	29.41	0.99	0.005	99.890	100	100	0.92	0.01
Pb^{2+}	95.837	100	166.7	0.96	0.017	90.109	92.59	138.89	0.99	0.016
	ZnO					ZnO-SS				
	qe(exp)(mg/g)	$q_{e(cal)}$ (mg/g)	h_O	R^2	K_2	qe(exp)(mg/g)	$q_{e(cal)}$ (mg/g)	h_O	R^2	K_2
As^{3+}	30.675	25.13	7.63	0.94	0.012	94.278	104.16	38.46	0.99	0.004
Cd^{2+}	77.527	102.0	14.93	0.97	0.001	89.575	100	41.57	0.99	0.004
Cr^{6+}	83.368	94.36	26.88	0.98	0.003	70.499	74.62	47.62	0.99	0.008
Ni^{2+}	99.032	94.34	22.22	0.73	0.002	99.878	83.33	83.33	0.99	0.012
Pb^{2+}	88.997	84.75	1000	0.99	0.14	94.197	100	35.71	0.95	0.004

Results from the Table 4.8 indicate that the experimental data obtained from adsorption of all the contaminant ions onto various adsorbents show high coefficient of correlation values of the range (0.73-0.99) suggesting high compliance to pseudo- second order kinetic model. Moreover, amounts of contaminant ions values adsorbed on the adsorbents at equilibrium derived from the model are in close agreement with that of the experimental values. Values for the rate of initial concentration were observed to be high for adsorption of those contaminant ions with considerable high qe value of 125-384.61. Availability of vacant active adsorption sites on the adsorbents and high affinity of the adsorbing contaminant ions to the adsorbents could explain the prevailing high initial concentration sorption rate(ho) (Aseel et al., 2014, Shi et al., 2013, Kilic et al., 2011).

The apparent high initial adsorption rate values of adsorbents and high equilibrium adsorption amounts ($qe_{(cal)}$) observed also implies that adsorption process of the contaminant ions was fast with short adsorption equilibrium attainment times (Sobhy 2014). However, affinity of contaminant ions on the adsorbents is of higher degree for the starch modified adsorbents (Fe_3O_4-SS, MnO-SS and ZnO-SS) than the normal adsorbents (Fe_3O_4, MnO and ZnO). More active adsorption sites orchestrated by introduction of starch materials could explain the obvious affinity variations. Considering the suitability of data obtained from adsorption of the contaminant ions onto individual adsorbents with the pseudo second order model, the starch modified adsorbents describe the data better than the ordinary adsorbents in the following order Fe_3O_4-SS>ZnO-SS>MnO-SS whereas the order of compliance of data obtained in the adsorption processes of contaminant ions onto the ordinary adsorbents with the pseudo second order model was observed to be in this manner; MnO >ZnO>Fe_3O_4. The observed disparity in the model compliance could be alluded to the apparent variations in levels of disagreements between the values of equilibrium adsorption densities calculated from the model $qe_{(cal)}$ the equilibrium adsorption densities obtained from the experiment $qe_{(exp)}$, and variations in the initial sorption rate values (yo). All these factors were

orchestrated by the differences in the availability of vacant active adsorption sites of various adsorbents which has proven to be key to robust adsorption process (Chiou and Li 2002, Sobhy, 2014).

4.6.3 Elovich Adsorption Model

Elovich model was also employed to ascertain the suitability of the kinetic data obtained from the adsorptions of As^{3+}, Cd^{2+}, Cr^{6+}, Ni^{2+} and Pb^{2+} contaminant ions onto various adsorbents; Fe_3O_4: Fe_3O_4-SS, MnO: MnO-SS and ZnO: ZnO-SS. The description of the data obtained by the model was observed to be linear curves as represented in Figures 4,34a: 4,34b,4.35a: 4.35b, 4.36a :4.35b. The linearity of the curves is an indication of direct relationship between the contaminant ions adsorbed onto the Nano adsorbents at certain periods with the natural log of the adsorption time. Figures 4,35a and 4,35b represent adsorptions of As^{3+}, Cd^{2+} and Cr^{6+}, Ni^{2+}, Pb^{2+} respectively onto Fe_3O_4: Fe_3O_4-SS Nano adsorbents Figs 4.36a and 4.36b shows adsorptions of As^{3+}, Cd^{2+} and Cr^{6+}, Ni^{2+}, Pb^{2+} respectively onto MnO: MnO-SS Nano adsorbents whereas Figures 4.36a and 4.36b depicts As^{3+}, Cd^{2+} and Cr^{6+}, Ni^{2+}, Pb^{2+} adsorptions respectively onto ZnO: ZnO-SS adsorbents.

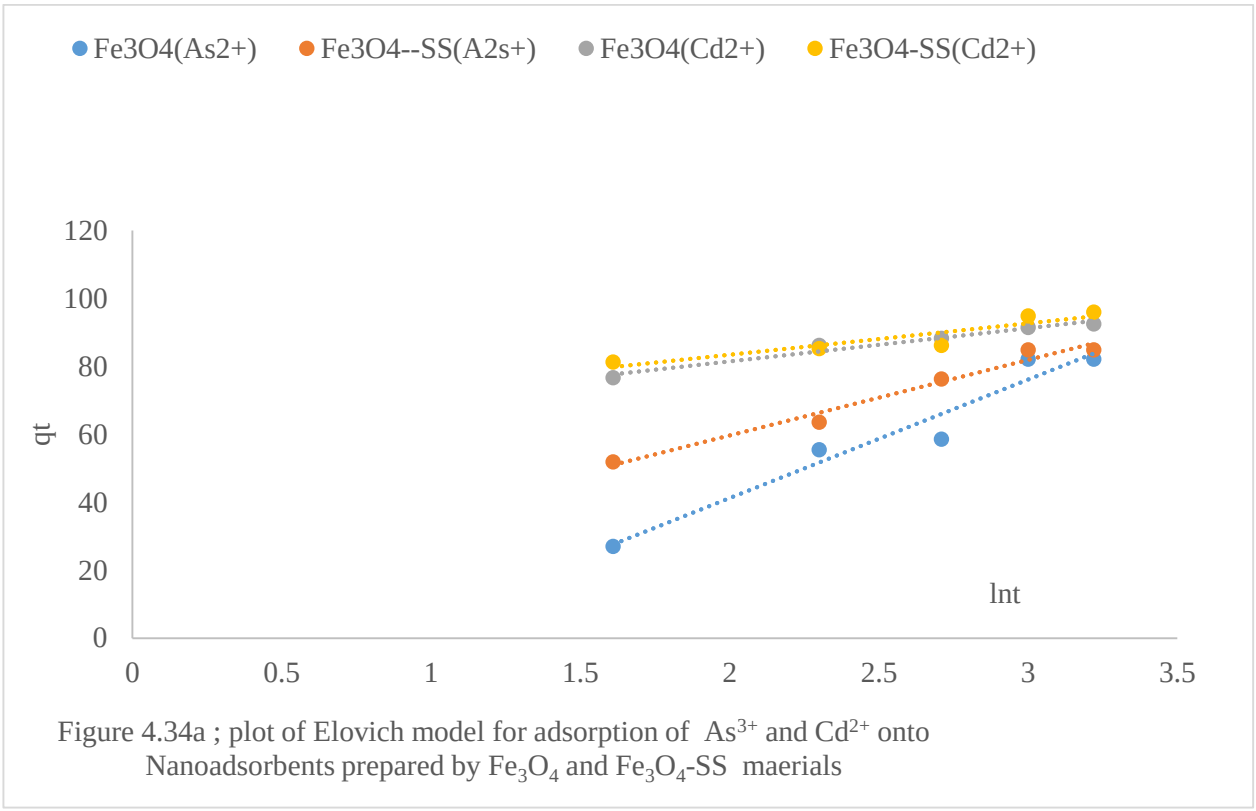

Figure 4.34a ; plot of Elovich model for adsorption of As^{3+} and Cd^{2+} onto Nanoadsorbents prepared by Fe_3O_4 and Fe_3O_4-SS maerials

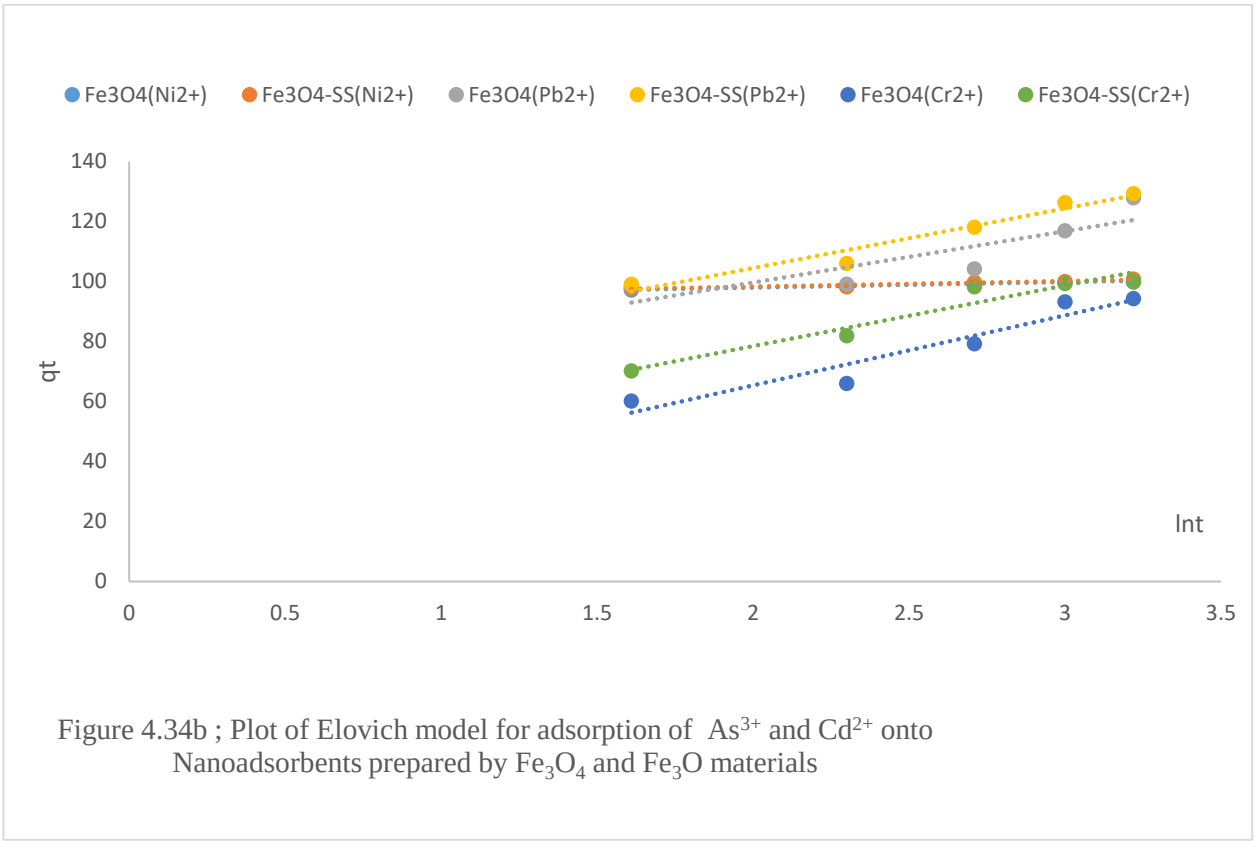

Figure 4.34b ; Plot of Elovich model for adsorption of As^{3+} and Cd^{2+} onto Nanoadsorbents prepared by Fe_3O_4 and Fe_3O materials

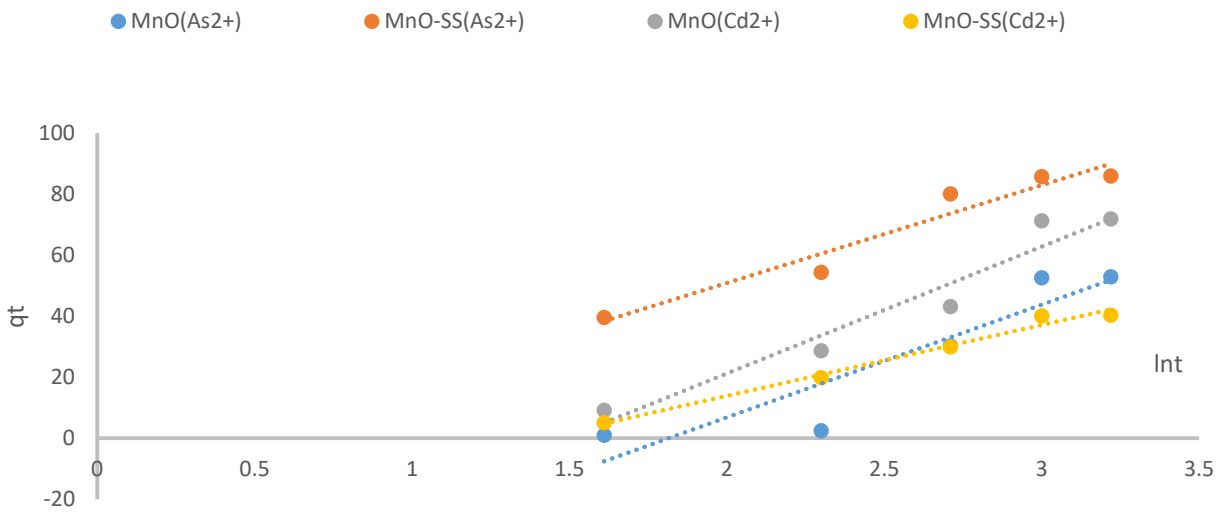

Figure 4.35a ; plot of Elovich model for adsorption of As^{3+} and Cd^{2+} onto Nanoadsorbents prepared by MnO and MnO-SS

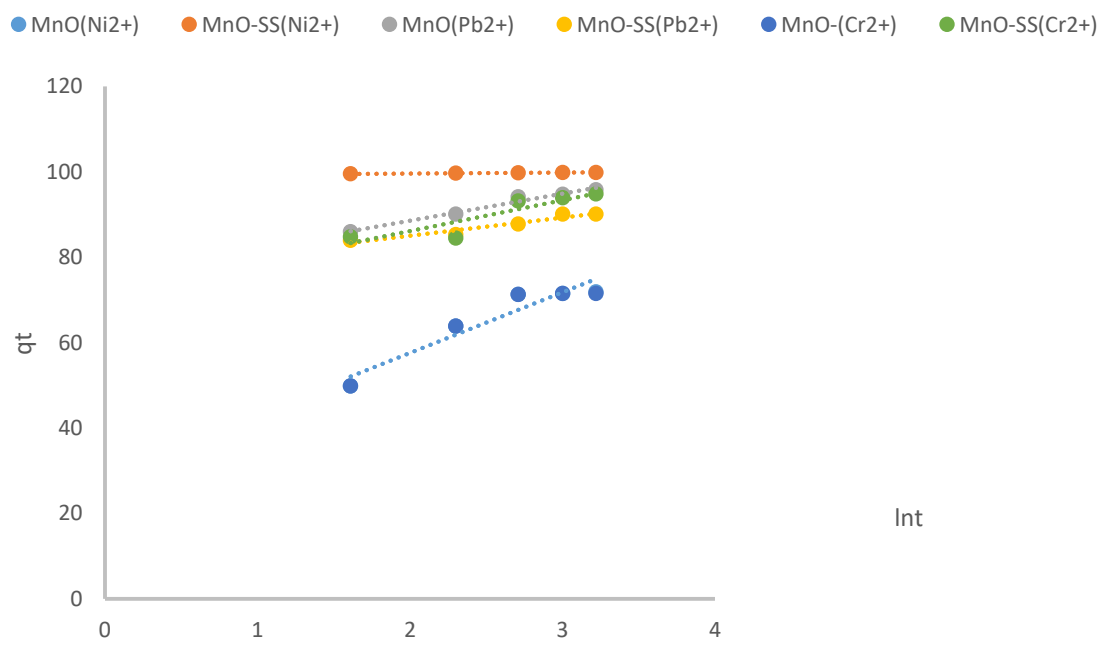

Figure 4.35b ; plot of Elovich model for adsorption of Ni^{2+}, Cr^{6+} and Pb^{2+} onto Nanoadsorbents prepared by MnO and MnO-SS materials

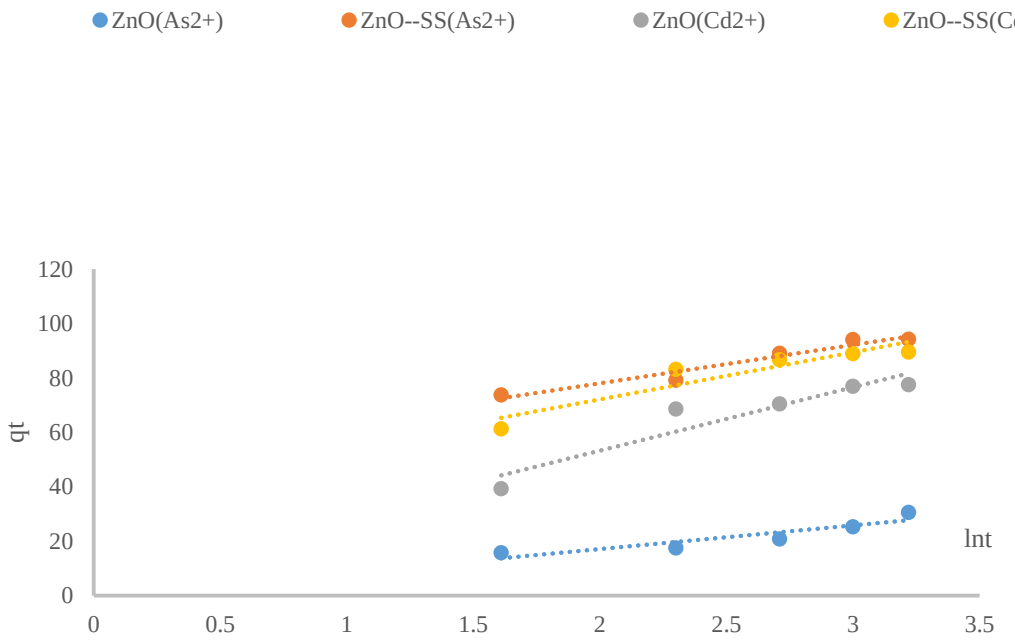

Figure 4.36a ; plot of Elovich model for adsorption of As^{3+} and Cd^{2+} onto Nanoadsorbents prepared by ZnO and ZnO-SS

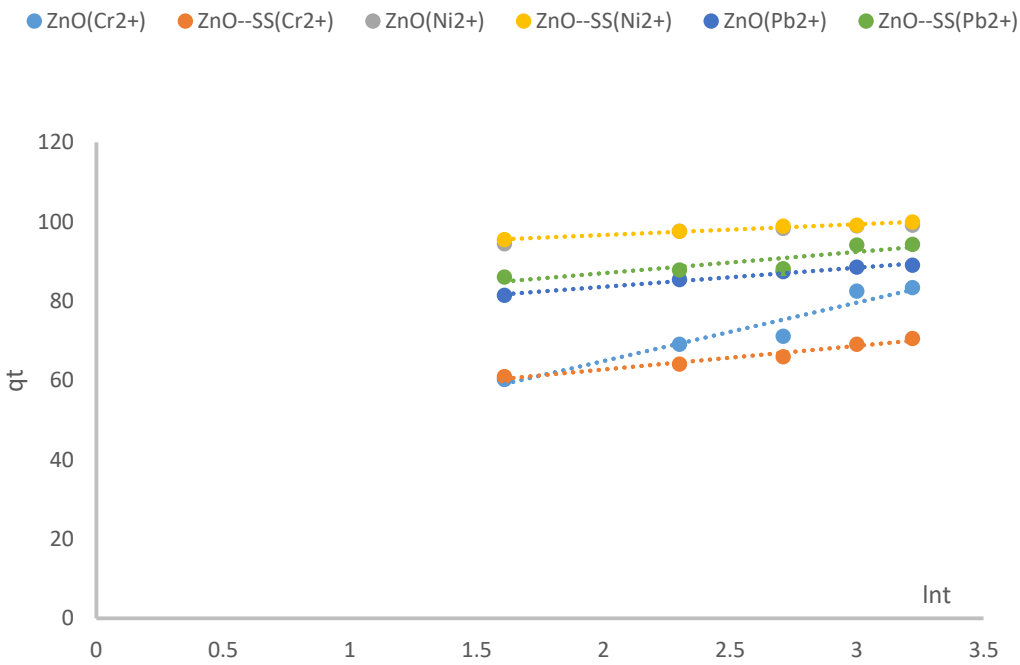

Figure 4.36b ; plot of Elovich model for adsorption of Ni^{2+}, Cr^{6+} and Pb^{2+} onto Nanoadsorbents prepared by ZnO and ZnO-SS

The correlation coefficient values (R^2), Elovich model parameters being represented by initial adsorption rate(α) and desorption constant (β) for the contaminant ions adsorption onto various adsorbents are presented on Table 4.9

Table4.9 Elovich model parameters for adsorption of the contaminant ions onto

Nano adsorbents prepared by Fe_3O_4: Fe_4O_3-SS, MnO; MnO-SS. and ZnO; ZnO-SS materials

	Elovich model parameters																	
	Fe_3O_4			Fe_3O_4-SS			MnO			MnO-SS			ZnO			ZnO-SS		
	β	α	R2	β	α	R2	β	α	R2	β	α	R2	β	α	R2	β	α	R2
As^{3+}	0.03	10.05	0.95	0.05	9.49	0.97	0.03	24.7	0.84	0.03	12.9	0.94	0.12	0.07	0.83	0.07	18.3	0.9
Cd^{2+}	0.13	22.79	0.97	0.11	23.9	0.85	0.08	5.91	0.94	0.04	11.9	0.98	0.04	2.44	0.88	0.06	13.7	0.8
Cr^{6+}	0.04	6.97	0.91	0.05	13.9	0.93	0.07	10.9	0.90	0.14	26.4	0.80	0.07	12.9	0.92	0.17	18.7	0.9
Ni^{2+}	0.55	36.69	0.97	0.53	34.8	0.93	0.08	19.7	0.91	4.59	36.5	0.97	0.35	33.2	0.93	0.37	33.6	0.9
Pb^{2+}	0.06	24.06	0.73	0.05	23.9	0.95	0.16	27.9	0.98	0.24	28.2	0.93	0.21	27.2	0.98	0.19	20.1	0.7

R^2 values which show the level of conformity between the experimental data the Elovich model predicted data were appreciable in every adsorption process. R^2 values ranged between 0.91 - 0.97, 0.85 - 0.98, 0.84 - 0.94, 0.80 - 0.98, 0.83 - 0.93 and 0.80 - 0.90. for Fe_3O_4, Fe_3O_4-SS, MnO, MnO-SS, ZnO and ZnO-SS respectively. The values show reasonable compliance of the obtained data with model. However, adsorption processes of the contaminant ions onto Fe_4O_3 Nano adsorbents complied most with Elovich model. Whereas the adsorption of contaminant ions onto ZnO-SS Nano adsorbent was observed to show the least compliance to the model. The prevailing variation could in this work could be alluded to differences in heterogeneity of the adsorbing surfaces and the chemisorption status of the process as was also observed by Sobhy (2014) and Aseel et al. (2014). Adsorption processes of the contaminant ions on the Nano adsorbents as described by Elovich kinetic model indicate that adsorbing surface of Fe_3O_4 adsorbent was most heterogeneous while that of ZnO-SS Nano adsorbent has the least heterogeneous surface which also agreed with Banerjee and Chattopadhyaya (2013). It could also be deduced from the result that chemisorption controls the adsorption process as a result of high conformity of the obtained data with Elovich model (Aseel et al., 2014). Initial adsorption rate also varies among the contaminant ions and the Nano adsorbents. Highest initial adsorption rate of contaminants ions on the Nano adsorbents was observed for Ni^{2+} ion with the lowest value recorded against As^{3+}. The implication is that substantial amount of Ni^{2+} ion was adsorbed on the Nano adsorbents within a short time from the commencement of the adsorption process leading to fast adsorption and short equilibrium time (Singh & Pant 2006). The prevailing scenario could probably be due to high affinity of the ion to the adsorbents(rf). However, initial adsorption rate of the ions on various Nano adsorbents decreased in this order; $Ni^{2+}>Pb^{2+}>Cd^{2+}>Cr^{6+}>As^{3+}$

4.6.4 Ritchie Adsorption Model

Fitness of data obtained from adsorption process of the contaminant ions (As^{3+}, Cd^{2+} and Cr^{6+}, Ni^{2+}, Pb^{2+}) onto Nano adsorbent materials of Fe_3O_4: Fe_3O_4-SS, MnO: MnO-SS and ZnO: ZnO-SS was tested with Ritchie model on the bases of level of coverage of the contaminant ions on the Nano adsorbents. The result as explained by Ritchie model produced linear curves of varying fitness with the model as presented on Figures below. Figs 4.37a and 4.37b represent adsorption of As^{3+}, Cd^{2+} and Cr^{6+}, Ni^{2+}, Pb^{2+} ion on Fe_3O_4 and Fe_3O_4-SS respectively.

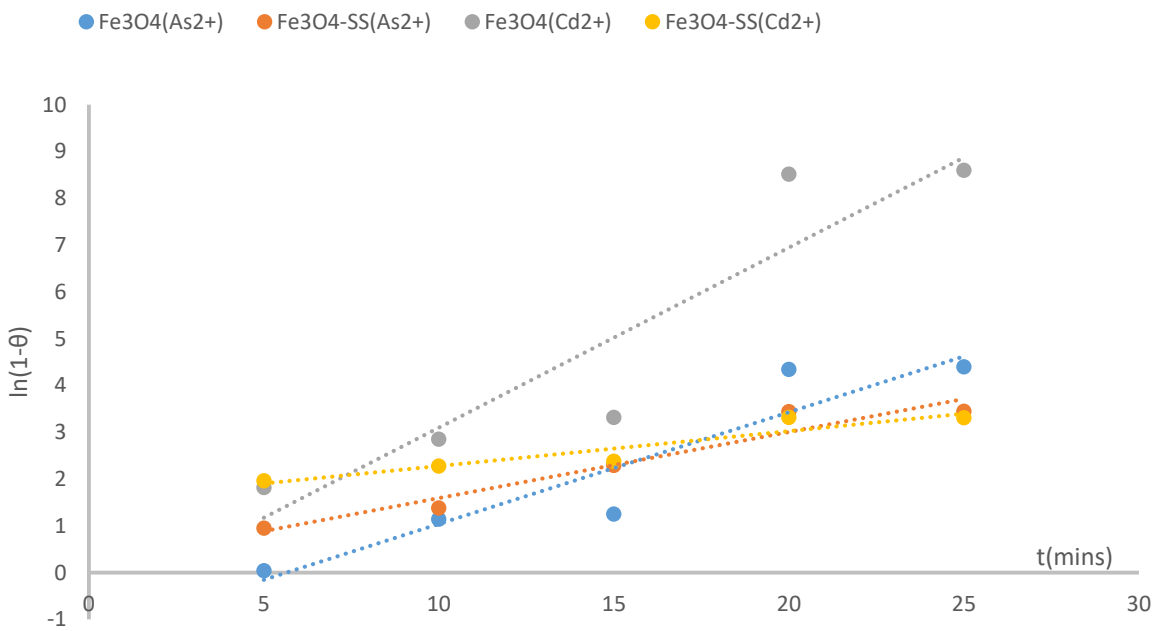

Figure 4.37a ; plot of Ritchie kinetic model for adsorption of As^{3+} and Cd^{2+} onto Nanoadsorbents prepared by Fe_3O_4 and Fe_3O_4-SS materials

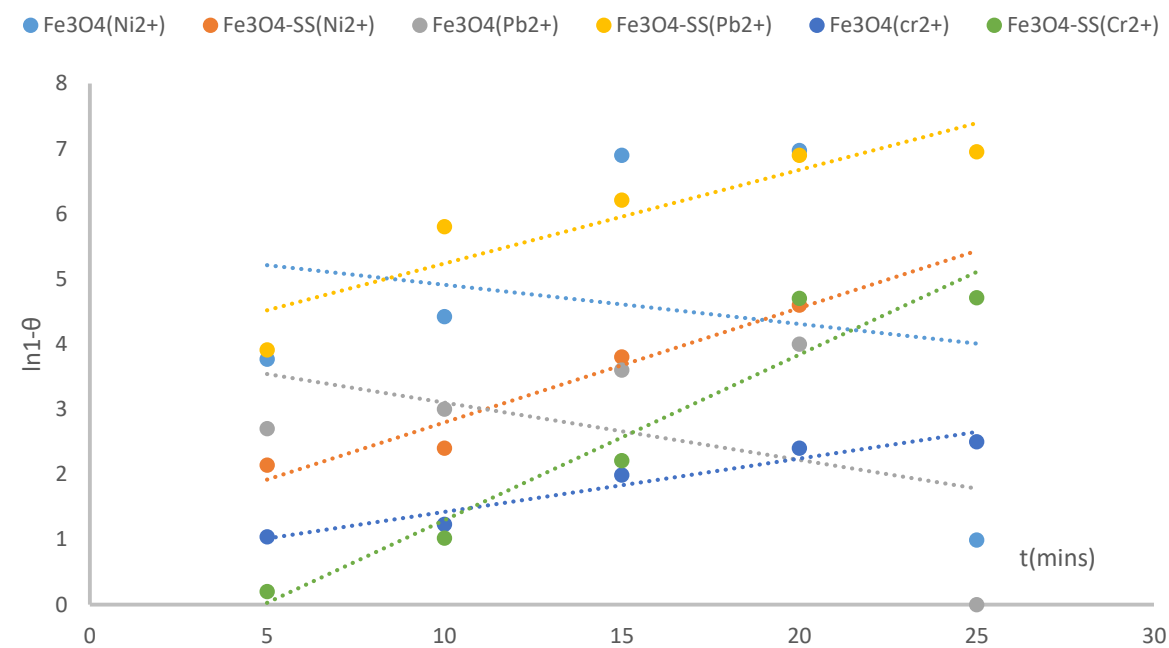

Figure 4.37b ; Plot of Ritchie kinetic model for adsorption of Ni^{2+}, Cr^{6+} and Pb^{2+} onto Nanoadsorbents prepared by Fe_3O_4 and Fe_3O_4-SS maerial

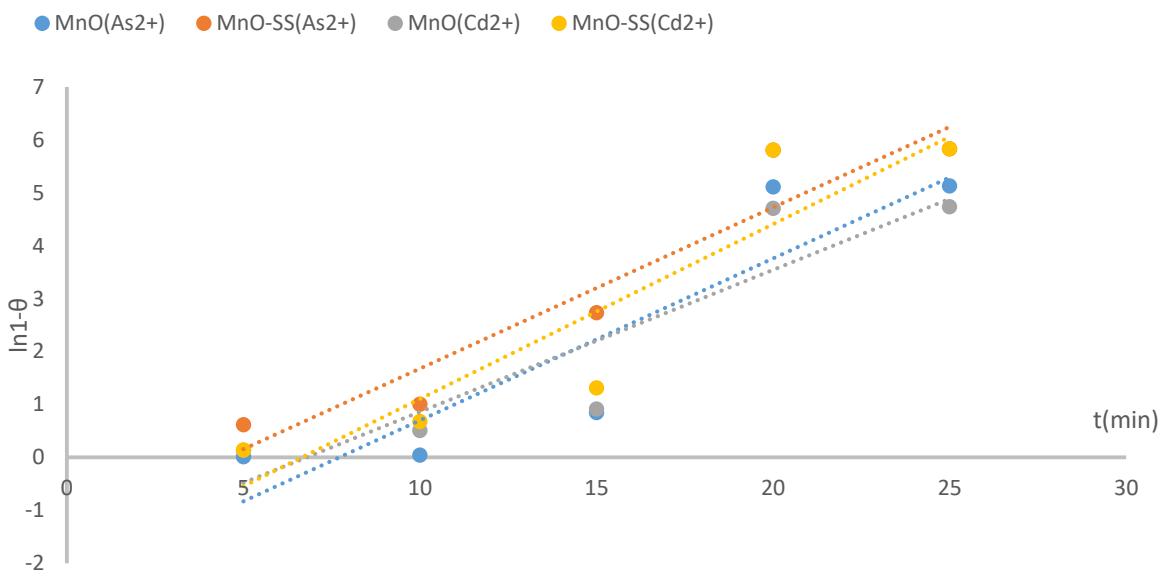

Figure 4.38a ; plot of Ritchie kinetic model for adsorption of As^{3+}, Cd^{2+} onto Nanoadsorbents prepared by MnO and MnO-SS maerials

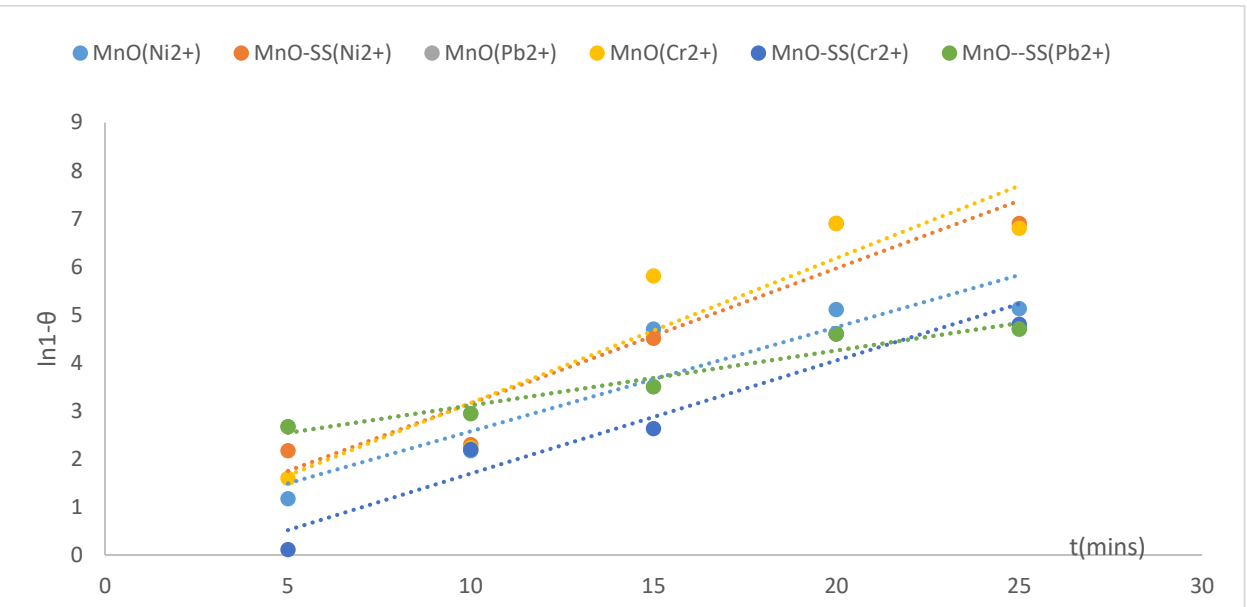

Figure 4.38b ; plot of Ritchie kinetic model for adsorption of Ni^{2+}, Cr^{6+} and Pb^{2+} onto Nanoadsorbents prepared by MnO and MnO-SS materials

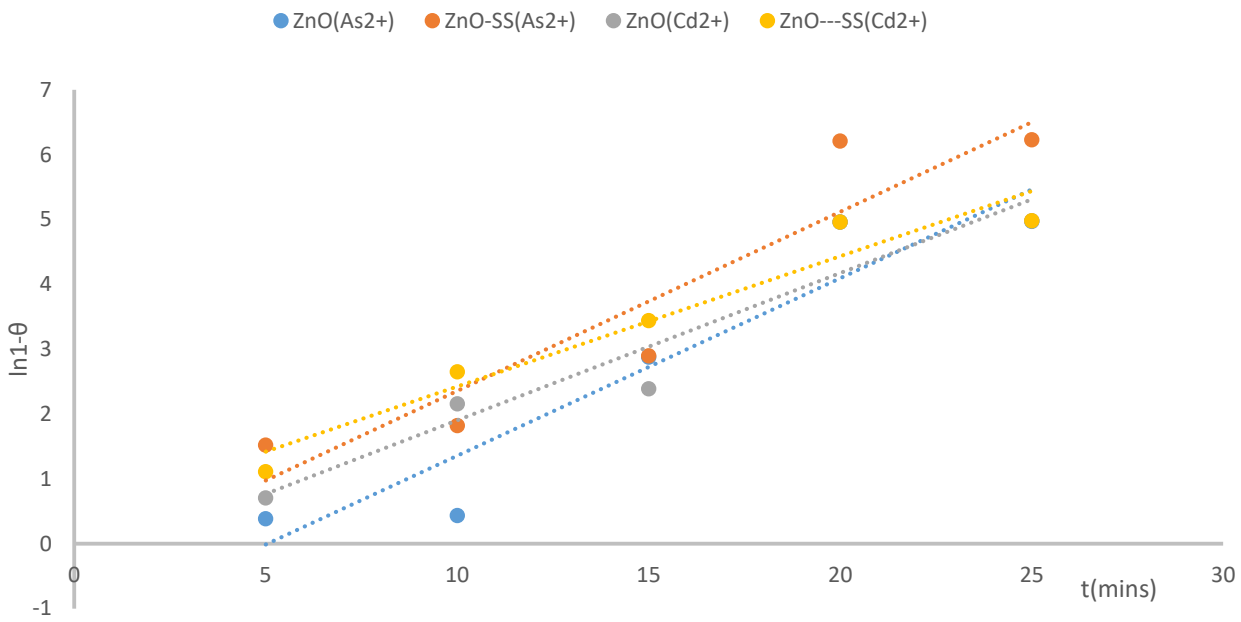

Figure 4.39a ; Plot of Ritchie kinetic model for adsorption of As^{2+}, Cd^{2+} onto Nanoadsorbents prepared by ZnO and ZnO-SS materials

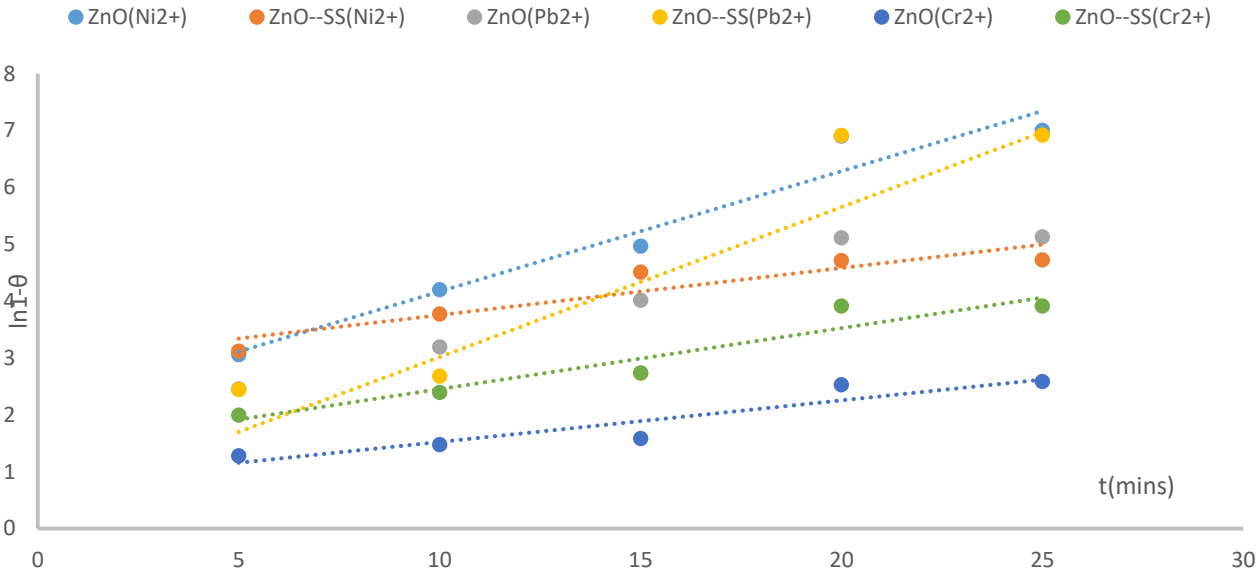

Fig 4.39b ; Plot of Ritchie kinetic model for adsorption of Ni^{2+}, Cr^{6+} and Pb^{2+} onto Nanoadsorbents prepared by ZnO and ZnO-SS materials

Adsorptions of As^{3+}, Cd^{2+} and Cr^{6+}, Ni^{2+} Pb^{2+} ion on MnO: MnO-SS Nano adsorbents are shown on Figures 4.39a- and 4.39b respectively, whereas the results of the kinetic adsorption data of As^{3+}, Cd^{2+} and Cr^{6+}, Ni^{2+}, Pb^{2+} ion on ZnO: ZnO-SS adsorbents as described by Ritchie model are shown on figs4.39a and 4.39b - respectively.

The coefficient of correlation(R^2) and the adsorption rate constant (K_1) are represented and shown on the Table4.10

Table 4.10: Ritchie Kinetic model parameters for adsorption of the contaminant ions onto Nano adsorbents prepared by Fe_4O_3:Fe_4O_3-SS, MnO; MnO-SS. and ZnO; ZnO-SS materials

	Fe_3O_4				
	As^{3+}	Cd^{2+}	Cr^{6+}	Ni^{2+}	Pb^{2+}
K_1	0.24	0.39	0.08	-0.1	0.1
R^2	0.88	0.86	0.94	0.04	0.2
		Fe_3O_4-SS			
K_1	0.14	0.1	0.25	0.18	0.14
R^2	0.94	0.89	0.93	0.95	0.84
		MnO			
K_1	0.31	0.27	0.30	0.22	0.12
R^2	0.91	0.84	0.87	0.86	0.89
		MnO-SS			
K_1	0.31	0.03	0.24	0.28	0.11
R^2	0.91	0.85	0.94	0.91	0.94
		ZnO			
K_1	0.27	1.14	0.37	0.21	0.15
R^2	0.90	0.91	0.88	0.95	0.95
		ZnO-SS			
K_1	0.28	1.01	0.11	0.08	0.26
R^2	0.88	94	0.92	0.97	0.78

From the Table, 4.10 variations of correlation coefficients(R^2) values were observed for contaminant adsorptions on various adsorbents. R^2 values ranged between 0.2 - 0.88, 0.84 - 0.94; 0.84 - 0.91, 0.85 - 0.91; 0.88 - 0.95, and 0.78 - 0.0.97 for adsorption of contaminant ions on Fe_3O_4, Fe_3O_4 --SS; MnO, MnO-SS and ZnO, ZnO-SS respectively. The model fitted the data obtained from the adsorption processes of contaminant ions onto ZnO Nano adsorbent better than others. Nevertheless Ni^{2+} adsorption with ZnO-SS Nano adsorbent complies most with Ritchie model with R^2 value of 0.97. from the prevailing observations, it could be inferred that the levels of coverage of the contaminant ions on the respective adsorbents is in consonant with the degree of agreement of the adsorption kinetic data obtained during adsorption process with Ritchie model which measure was with R^2 values (Junsheng et al., 2014).From the foregoing ,the contaminant ions showed high degree of coverage onto ZnO nano adsorbent except Ni^{2+} which was observed to show significant coverage on ZnO-SS Nano adsorbent .

4.6.5 Sticking Probability Kinetic Model

Compliance of adsorption kinetics of the contaminant ions (As^{3+}, Cd^{2+} and Cr^{6+}, Ni^{2+}, Pb^{2+}) on to various Nano adsorbents of Fe_3O_4:Fe_3O_4-SS, MnO: MnO-SS and ZnO:ZnO-SS was tested with sticking probability model in which $\ln(1-\theta)$ and $\frac{1}{T}$ were related. The relationship produced curves of varying linearity which was measured by the correlation coefficients (R^2). the linear curves produced in the adsorption kinetic data of As^{3+}; Cd^{2+} and Ni^{2+}; Cr^{6+}; Pb^{2+} ion Fe_3O_4:Fe_4O_3-SS, MnO: MnO-SS and ZnO: ZnO-SS respectively are displayed on Figures 4.40a, 4.40b, 4.41a 4.41b, 4.42a and 4.42b

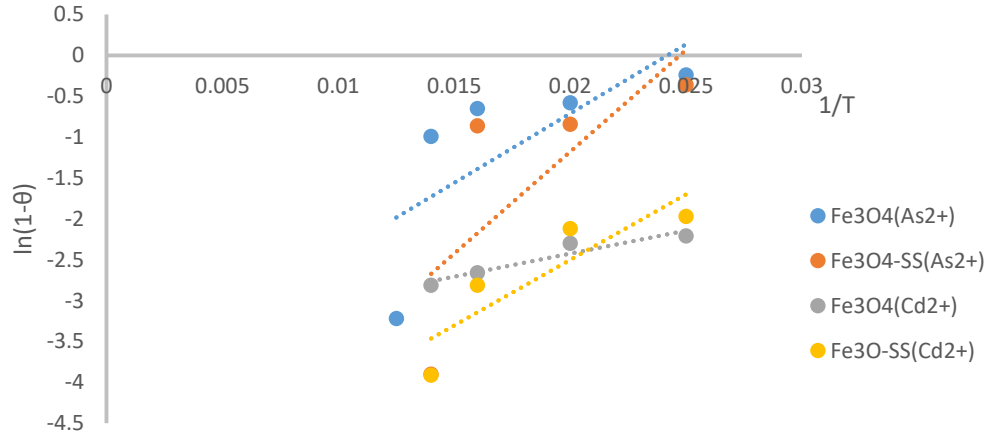

Figure 4.40a ; plot of sticking propability Kinetic modell for adsorption of As^{3+} and Cd^{2+} onto Nanoadsorbents prepared by Fe_3O_4 and Fe_3O_4 -SS maerials

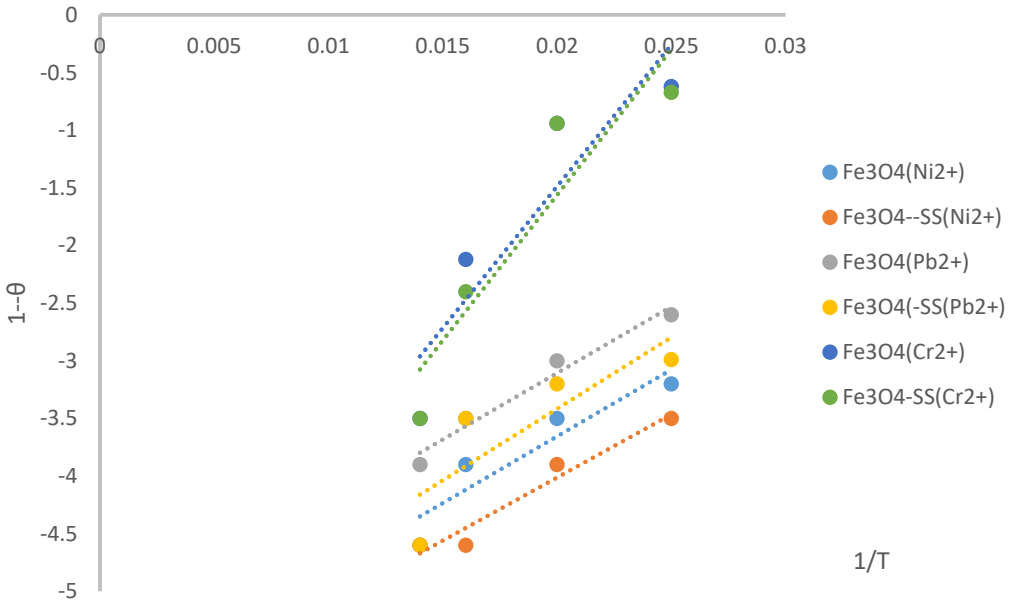

Figure 4.40b ; plot of sticking propability Kinetic modell for adsorption of Ni^{2+} , Cr^{6+} and Pb^{2+} onto Nanoadsorbents prepared by Fe_3O_4 and Fe_3O_4 -SS maerials

The parameters (Ea (J/mol/K, *S and R^2) derived from sticking probability model are shown on Table- 4.10

Table 4.11; Sticking probability model parameters for adsorption of the contaminant ions onto Nano adsorbents prepared by Fe_4O_3: Fe_4O_3-SS, MnO; MnO-SS.and ZnO; ZnO-SS materials

Fe_3O_4	As^{2+}	Cd^{2+}	Cr^{2+}	Ni^{2+}	Pb^{2+}
Ea(J/mol/K	-357.98	-733.28	3797.34	236.05	580.11
$^*S$	0.37	-3.8	-29.58	-10.56	-13.67
R^2	0.51	0.90	0.84	0.86	0.91
		Fe_3O_4-SS			
Ea	262.47	34.73	670.01	1728.98	764.31
$^*S$	-5.27	-6.56	-11.6	-21.83	-14.71
R^2	0.55	0.77	0.86	0.95	0.71
		MnO			
Ea	1989.21	37.40	1928.82	2920.46	3087.99
$^*S$	-3.3	1.44	-15.03	-32.02	-31.64
R^2	0.54	0.81	0.65	0.92	0.85
		MnO-SS			
Ea	1679.68	308.12	1673.36	-48.89	602.77
$^*S$	-3.03	-5.84	-14.02	-12.18	-13.86
R^2	0.99	0.96	0.90	0.98	0.70

	ZnO				
Ea	2133.54	1312.12	2646.92	531.27	1502.92
$^{*}S$	-17.53	-13.86	-23.65	-19.54	-19.30
R^2	0.84	0.48	0.64	0.65	0.99
		ZnO-SS			
Ea	783.15	1676.68	1057.96	450.54	-969.99
$^{*}S$	-9.60	-17.37	-17.67	-11.88	0.1
R^2	0.94	0.95	0.89	0.98	0.97

The correlation coefficient values revealed significant correlation, suggesting meaningful agreement of the data with sticking probability model. However, data obtained from adsorption of the contaminant ions (As^{3+}; Cd^{2+}; Ni^{2+}; Cr^{6+}; Pb^{2+}) onto MnO-SS and ZnO-SS adsorbents showed strongest correlation with R^2 value ranges of between 0.77 - 0.99 and 0.89 - 0.98 respectively, whereas the weakest correlation values were observed at the adsorption of contaminant ions onto Fe_3O_4-SS adsorbent with the range of 0.55 and 0.91.

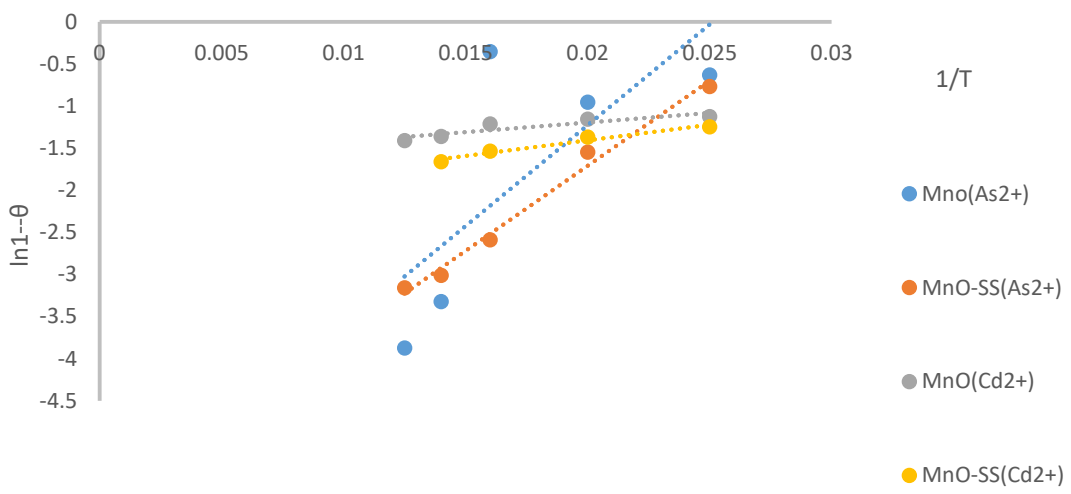

Figure 4.41a ; plot of sticking propability Kinetic modell for adsorption of As^{2+} and Cd^{2+} onto Nanoadsorbents prepared by MnO and MnO-SS maerials

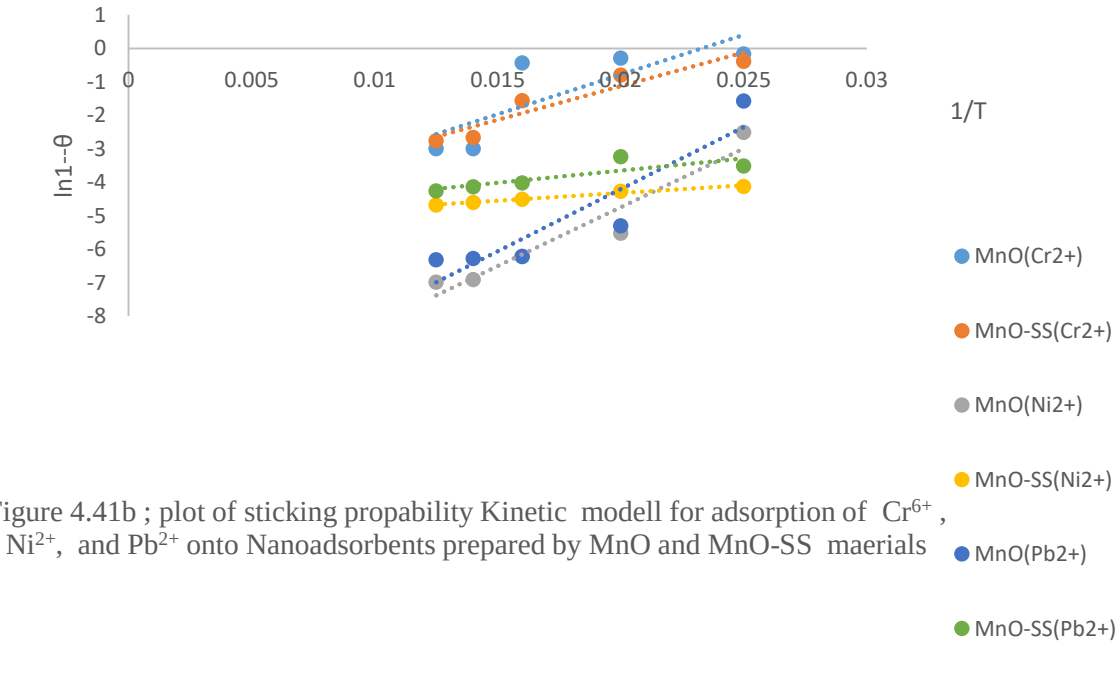

Figure 4.41b ; plot of sticking propability Kinetic modell for adsorption of Cr^{6+}, Ni^{2+}, and Pb^{2+} onto Nanoadsorbents prepared by MnO and MnO-SS maerials

Table 4.10 also revealed that the probability/sticking coefficients (S^*) are on the negative values except in the processes of adsorption of As^{3+}, Cd^{2+} and Pb^{2+} onto Fe_3O_4, MnO and ZnO-SS adsorbents respectively with respective sticking coefficients of 0.35, 1.44 and 0.1. With comparatively higher sticking coefficient values, As^{3+}, Cd^{2+} and Pb^{2+} contaminant ions are more likely to have firm bind to the aforementioned adsorbents than the other contaminant ions (Dawodu et al., 2015).

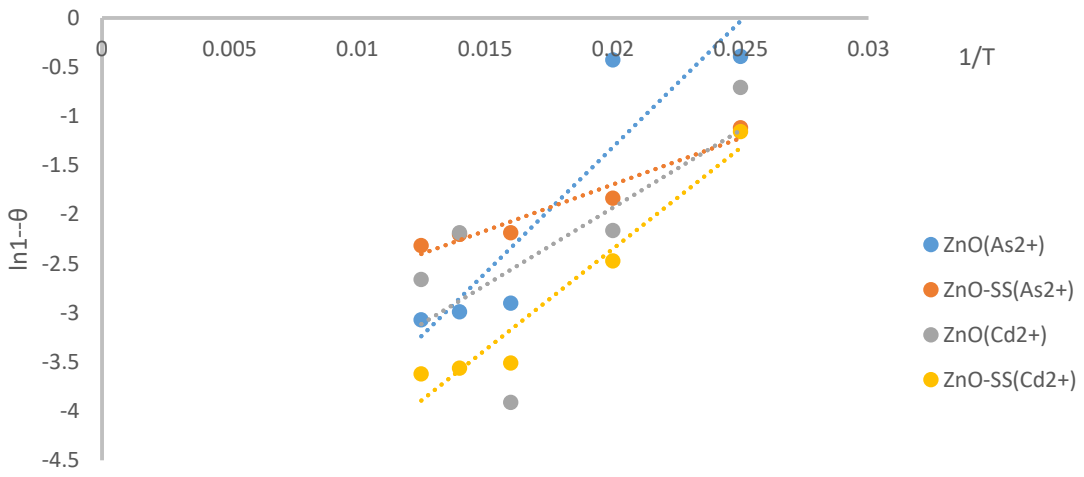

Figure 4.42a ; plot of sticking propability Kinetic modell for adsorption of As^{3+} and Cd^{2+} onto Nanoadsorbents prepared by ZnO and ZnO-SS materials

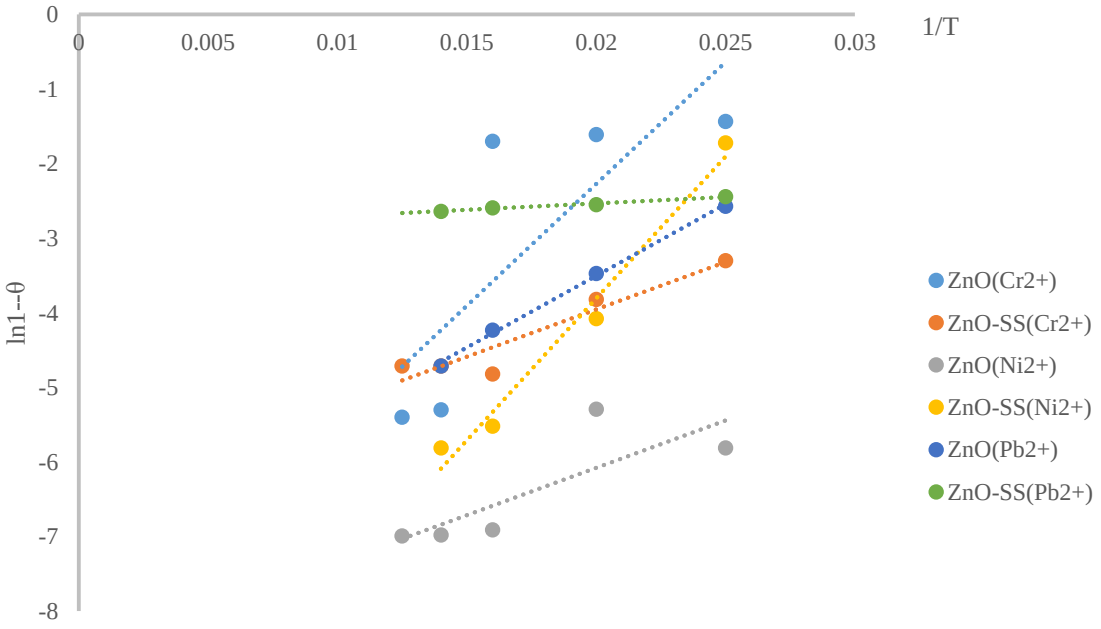

Figure 4.42b ; plot of sticking propability Kinetic modell for adsorption of Cr^{6+} , Ni^{2+}, and Pb^{2+} onto Nanoadsorbents prepared by ZnO and ZnO-SS maerials

On the other hand, the contaminant ions with negative sticking coefficient values hit the adsorbent surfaces with weak bind to the adsorbents. Yoshiki and Yuta (2007) reported that Sticking probability model evaluated the status of adsorption processes of As^{3+}; Cd^{2+}; Ni^{2+}; Cr^{6+}; Pb^{2+} ions onto various adsorbents and the result obtained by the authors also revealed that adsorption processes of virtually all the contaminant ions onto the adsorbents were controlled by physiosorption as their sticking coefficients were less than one (S^*<1). This assertion agreed with this work except adsorption process of Cd^{2+} onto MnO Nano adsorbent which sticking coefficient of 1.44 hence controlled by chemisorption process as observed by Yoshiki and Yuta (2007). The Table also showcases varying activation energy of adsorption values for each contaminant ion on various Nano adsorbents. Being the minimum energy required by the contaminant ions to initiate adsorption process as described by ref, Cd^{2+}, needed the lowest activation energy of -733.28, 34.73 and 37.40 J/mol/K to initiate adsorption process onto Fe_3O_4, Fe_3O_4--SS, MnO respectively, whereas Ni2+ ion required the lowest activation energy of -48.89 and 531.27 to hit and adsorbed on MnO-SS and ZnO Nano adsorbent surfaces. This implies that Cd^{2+} and Ni^{2+} ions were the first to hit and adsorbed on the surfaces of the aforementioned Nano adsorbents as was also recorded by Junsheng et al. (2014). Also, Pb^{2+} contaminant ion with lowest activation energy of -969.99J/mol/K was the first to hit and adsorbed on ZnO-SS Nano adsorbent surface.

4.7 Thermodynamic Study

The behavior of adsorption process of contaminant ions (As^{3+}; Cd^{2+}; Ni^{2+}; Cr^{6+}; Pb^{2+} ions) onto various Nano adsorbents (Fe_3O_4:Fe_3O_4-SS, MnO: MnO-SS and ZnO: ZnO-SS) in terms of thermodynamic process was investigated. The thermodynamic models were adopted in which linear plots of (lnK_0) versus $\left(\frac{1}{T}\right)$. at varying temperature values were obtained to determine various thermodynamic model parameters of Gibb free energy (ΔG), enthapy of adsorption (ΔH^0) and adsorption entropy (ΔS^0). The thermodynamic model

parameters for each adsorption process of contaminant ion on the respective Nano adsorbents are displayed on Table-4.11

Table 4.12: Thermodynamic model parameters for adsorption of the contaminant ions onto Nano adsorbents prepared by Fe_3O_4:Fe_3O_4-SS, MnO ; MnO-SS. and ZnO; ZnO-SS materials

	Fe_3O_4					Fe_3O_4-SS				
	As^{3+}	Cd^{2+}	Cr^{6+}	Ni^{2+}	Pb^{2+}	As^{3+}	Cd^{2+}	Cr^{6+}	Ni^{2+}	Pb^{2+}
ΔH^o	-5620	-3389	-7164	-6858	-1356	-4708	-6192	-237	-9929	-997
ΔS^o	16.05	12.898	18.16	24.87	5.92	13.6	21.57	- 3.032	34.07	4.87
	MnO					MnO-SS				
ΔH^o	-2282	-2601	-5466	-3493	-2412	-1629	-803	-2029	-6709	-837
ΔS^o	5.0096	13.69	12.90	14.6	8.17	2.4186	8.2644	2.4764	25.38	3.83
	ZnO					ZnO-SS				
ΔH^o	-520	-3790	-2780	-2560	-1320	-4996	-3930	350	-510	-2740
ΔS^o	2.386	12.176	9.464	12.04	5.8	17.002	13.41	- 0.482	5.48	10.492
Temp(K)	ΔG^o Fe_3O_4					$\Delta G^o Fe_3O_4$-SS				
	As2+	Cd2+	Cr2+	Ni2+	Pb2+	As2+	Cd2+	Cr2+	Ni2+	Pb2+
313	-5415.4	5259.21	-13017	8483.4	4702	-4033.5	4574	-9997.96	5879	4374.44
323	-3096.3	5698.47	-11819	9071.4	3427	-1914.71	5325	-10204.6	9071	4532.99
333	-2907	877.11	6725	2018.3	437.5	1860.5	604.1	9895	7374	5490
343	569.01	12829.8	-6887	12348	6171	943.91	11142	-10691.0	17718	5546.56
353	140.87	7416.33	-7082	18235	5990	827.63	11422	-11002.7	17040	6019.36
	ΔG^oMnO					ΔG^oMnO-SS				
313	-6216.9	13773.9	-11879	7674	62.46	-7661.12	14632	-10466.4	12751	3018.65
323	-5617.9	14256.8	-10801	11329	2990	-6786.06	15682	-10438	11239	3112.4
333	-4509.9	16470.1	-10240	12121	3248	-6508.89	16265	-9739.81	12486	3217.07
343	-4437.5	18946.7	-7260	11835	3365	-6427.74	17079	-9553.2	12833	4961.96
353	4449.2	17697.1	-7631	13353	3463	-6650.35	17462	-9614.54	23813	3780.08
	ΔG^oZnO					ΔG^oZnO-SS				
313	234.21	-1145	1066.9	9446.3	3825	2685.56	1197	1899.67	9681	4736.15

323	-4163.4	2094.63	2148.3	11279	4726	3598.47	4297	1369.57	11333	5290.28
333	-332.23	3433.02	4069.8	10825.	5371	5813.98	4817	1439.65	12182	5537.12
343	-37.07	3450.56	4220.5	11549	5818	7984.77	6131	1539.91	13346	8188.21
353	-117.39	3639.2	4284.9	11622	5840	8217.65	6309	1584.81	13999	8158.86

4.7.1 Enthapy Change of Adsorption (ΔH^0)

From the Table 4.12, negative values of enthalpy of adsorption of virtually all the contaminant ion onto the Nano adsorbents except Cr^{6+} adsorption on ZnO-SS Nano adsorbent were observed. The negative values of enthalpy indicated exothermic adsorption processes of the concerned contaminant ions (Uzoije et al., 2015) where energy of adsorption was given out. The release of energy on account of exothermic adsorption process might result to temperature reduction which by extension could affect adsorption efficiency of the contaminant ions (Uzoije et al., 2015; Dawodu et al., 2015). Positive ΔH^0 value for adsorption of Cr^{6+} ion onto ZnO-SS Nano adsorbent confirmed that the adsorption process was endothermic whereby substantial amount of heat was adsorbed with rise in the temperature of the system. Moreover, the rise in temperature could as well result to efficiency increase of Cr^{6+} adsorption onto ZnO-SS Nano adsorbent.

4.7.2 Entropy Change of Adsorption (ΔS^0)

On the other hand, positive values of adsorption entropy (ΔS^0) for all the contaminant ions except Cr^{6+}ion where negative values were observed in the course of Cr^{6+} adsorption onto Fe_4O_3-SS, MnO-SS and ZnO-SS Nano adsorbents. Entropy of adsorption (ΔS^0) described the degree of disorderliness or randomness of the solid/solution interface during the sorption process and negative ΔS^0 suggests decrease in the randomness and vice versa (Lakshmipathy & Sarada, 2024). In this study, degree of disorderliness of contaminant ions in solution in relation to Nano adsorbent interface increased in the following order;Pb^{2+} < Cd^{2+} < As^{3+} < Cr^{6+} < Ni^{2+} for Fe_4O_3 Nano adsorbent, Cr^{6+} < Pb^{2+} < As^{2+} < Cd^{2+} < Ni^{2+} for Fe_4O_3 --SS Nano adsorbent; As^{3+} < Pb^{2+} < Cr^{6+} < Cd^{2+} < Ni^{2+} for MnO Nano adsorbent; As^{3+} < Cr^{6+} < Pb^{2+} < Cd^{2+} < Ni^{2+} for MnO-SS Nano adsorbent ; As^{3+} < Pb^{2+} < Cr^{6+} <Ni^{2+} < Cd^{2+} for ZnO Nano adsorbent and Cr^{6+} < Ni^{2+} < Pb^{2+} < Cd^{2+} < As^{3+} for ZnO--SS Nano adsorbent. From the result, the entropy controlled adsorption process was mostly observed

in Ni^{2+} ion on all the Nano adsorbents except ZnO and ZnO-SS. Being highly at random within the adsorption system, the chances of Ni^{2+} adsorbed at a significant amount on the Nano adsorbents are high as those contaminant ions with less ability to exhibit high randomness and tendency to form precipitates during adsorption process adsorbed at lower amounts onto various Nano adsorbents. This observation is also in consonance with that reported by Hanan et al. (2010).

4.7.3 Gibb Free Energy Change of Adsorption (ΔG^o)

Gibb free energy change of adsorption (ΔG^o) was obtained with respect to varying temperature values in adsorption processes of the contaminant ions (As^{3+}. Cd^{2+}, Cr^{6+}, Ni^{2+} and Pb^{2+}) onto Nano adsorbents of Fe_3O_4, Fe_4O_3-SS; MnO, MnO-SS and ZnO, ZnO-SS. The result showed negative values for Gibbs free energy change of adsorption prcocess of Cr^{6+} ion onto Fe_4O_3, Fe_4O_3-SS and MnO, MnO-SS Nano adsorbents and As^{2+} adsorption process on Fe_3O_4, MnO and ZnO adsorbents. The negative values of ΔG^o observed at various temperature values confirmed spontaneity and high affinity for Cr^{6+} and As^{3+} ions on the above mentioned Nano adsorbents during the adsorption process as was recorded in the work of Muhammad and Farha (2018). Gibb free energy change of adsorption (ΔG^o) of virtually all the contaminant ions on various Nano adsorbents increased with rise in temperature value showing that the adsorption processes of the concerned contaminant ions and their respective Nano adsorbents were thermodynamically favourable. On the other hand, Gibb free energy change of adsorption (ΔG^o) for Cr^{6+} and As^{3+} ions on Fe_3O_4, Fe_3O_4-SS and MnO and Fe_3O_4, MnO and ZnO adsorbents. respectively was observed to decreased with increase in temperature and by implication indicate less favourable adsorption process of Cr^{6+} and As^{2+} ions on the above mentioned Nano adsorbents as was observed by other authors (Lakshmipathy & Sarada 2015; Uzoije et al., 2015).

4.8 Diffusion models

Data obtained from adsorption processes of As^{3+}. Cd^{2+}, Cr^{6+}, Ni^{2+} and Pb^{2+} contaminant ions onto Fe_3O_3, Fe_3O_4-SS; MnO, MnO-SS and ZnO, ZnO-SS. Nano adsorbents were tested with diffusion models to determine the external mass transfer and intra-particle diffusion rate controlling steps of the contaminant ions to various Nan absorbents.

4.8.1 Liquid diffusion model

A liquid diffusion model was applied to evaluate the rate of migration of the contaminant ions (external mass transfer) to the Nano adsorbents in which a plot of $\ln(1-\alpha)$ versus time produced straight curves with K_{t1} as the slope. The Figures are shown on as follows; Figures 4.43a ;4.43b, 4.44a; 4,44b, 4.45a;4.45b and 4.46a; 4.46b represent onto the rate of migration of the contaminant ions Fe_3O_4, Fe_3O_4 --SS; MnO, MnO-SS and ZnO, ZnO---SS respectively. liquid diffusion model parameter (K_{t1}) which describes adsorption capacities of various adsorbents to adsorb the contaminant ions are presented on Table 4.12.

Table 4.13 Liquid Diffusion Model Parameters for Diffusion of the Contaminant Ions onto various Nano Adsorbents

From the Figures (4.43a-4.45b) presented in this work, the direction of curves deviated from the origin suggesting that the contaminant ions diffused into the adsorbent through external particle diffusion mechanism and that diffusion of the contaminant ions through the liquid film boundary surrounding the Nano adsorbent precedes and predominate the intra-particle diffusion. This observation is in consonance with that reported by Sobhy (2014) that contaminant ions diffuse into adsorbent through diffusion and through liquid film boundary that surrounds intra-particles.

Liquid Diffusion Model Parameters

	Fe_3O_4				
	As	Cd	Cr	Ni	Pb
K_t	-0.18	-0.11	-0.4	-0.25	-0.02
R^2	0.95	0.99	0.75	0.67	0.01
		Fe_3O_4-SS			
K_t	-0.08	-0.05	-0.31	-0.08	-0.2
R^2	0.54	0.91	0.77	0.98	0.88
		MnO			
K_t	-0.31	-0.18	-0.06	0.03	0.13
R^2	0.53	0.33	0.03	0.01	0.40
		MnO-SS			
K_t	-0.11	-0.20	-0.05	0.17	0.08

R^2	0.12	0.23	0.05	0.17	0.18
		ZnO			
K_t	-0.38	-0.29	-0.22	-0.25	-0.16
R^2	0.79	0.92	0.79	0.95	0.78
		ZnO-SS			
K_t	-0.32	-0.27	-0.13	-0.12	-0.28
R^2	0.86	0.98	0.92	0.98	0.66

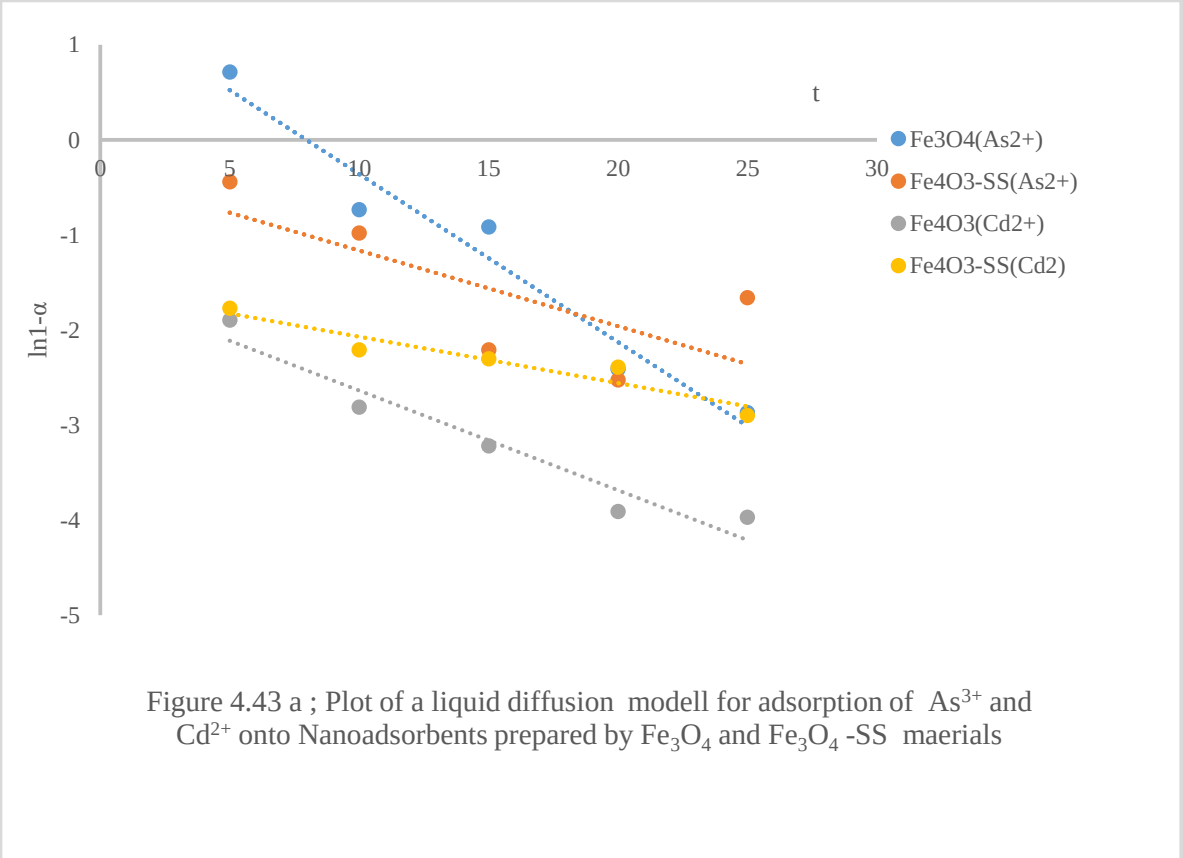

Figure 4.43 a ; Plot of a liquid diffusion modell for adsorption of As^{3+} and Cd^{2+} onto Nanoadsorbents prepared by Fe_3O_4 and Fe_3O_4 -SS maerials

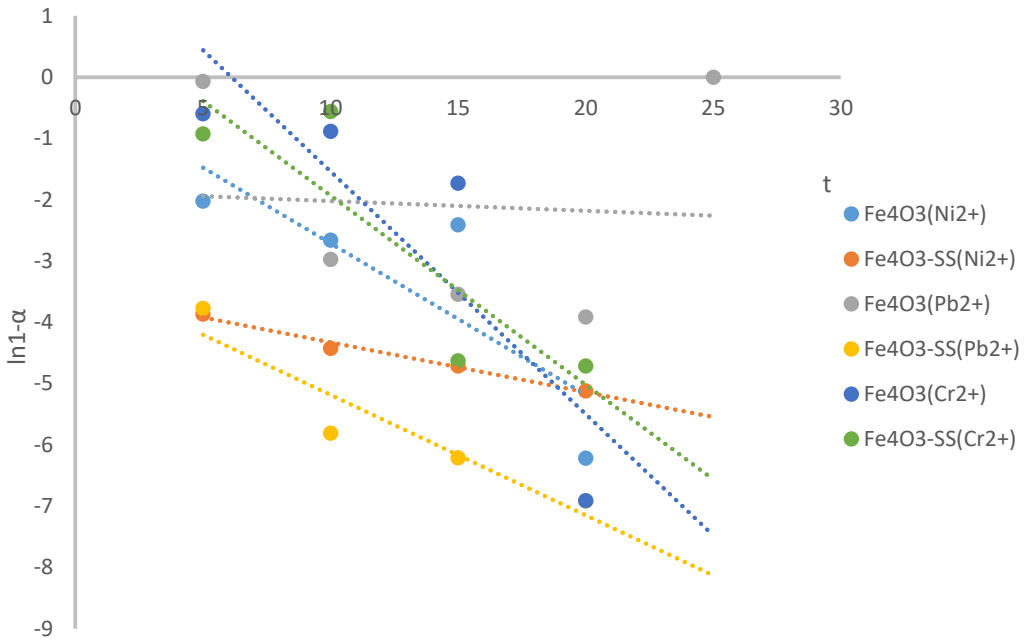

Fiureg 4.43 b ; Plot of a liquid diffusion modell for adsorption of Ni^{2+}, $Cr^{6+}$and Pb^{2+} onto Nanoadsorbents prepared by Fe_3O_4 and Fe_3O_4-SS materials

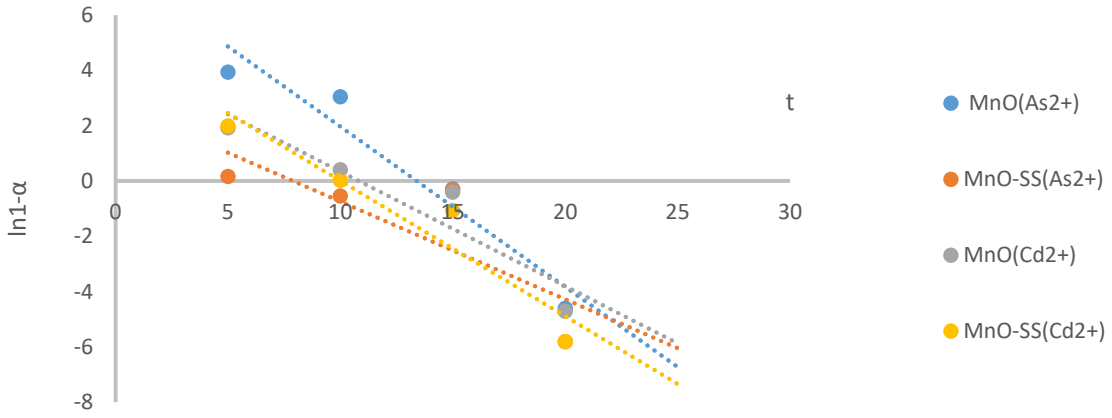

Figure 4.44 a ; Plot of a liquid diffusion modell for adsorption of As^{3+} and Cd^{2+} onto Nanoadsorbents prepared by MnO and MnO-SS materials

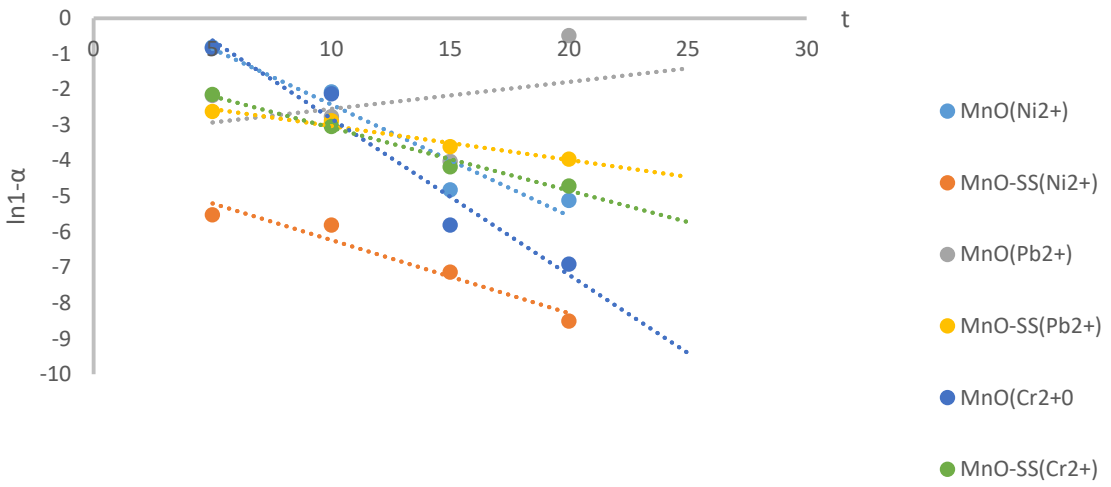

Figure 4.44 b ; Plot of a liquid diffusion modell for adsorption of Ni^{2+}, Cr^{6+} and Pb^{2+} onto Nanoadsorbents prepared by MnO and MnO-SS materials

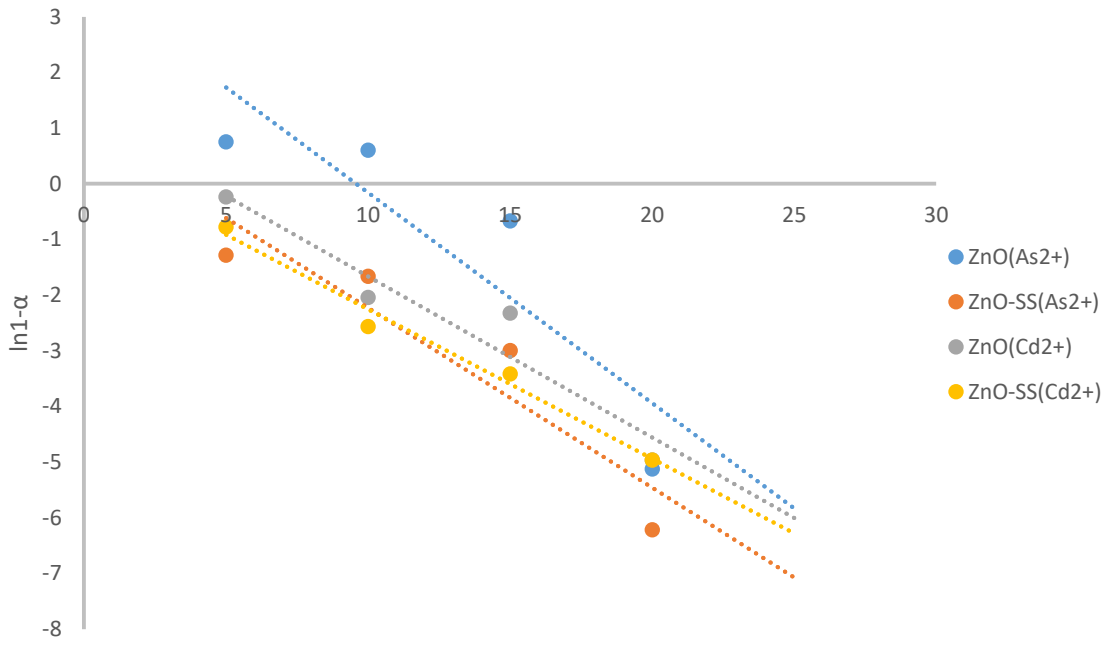

Figure 4.45 a ; Plot of a liquid diffusion modell for adsorption of As^{3+} and Cd^{2+} onto Nanoadsorbents prepared by ZnO and ZnO-SS materials

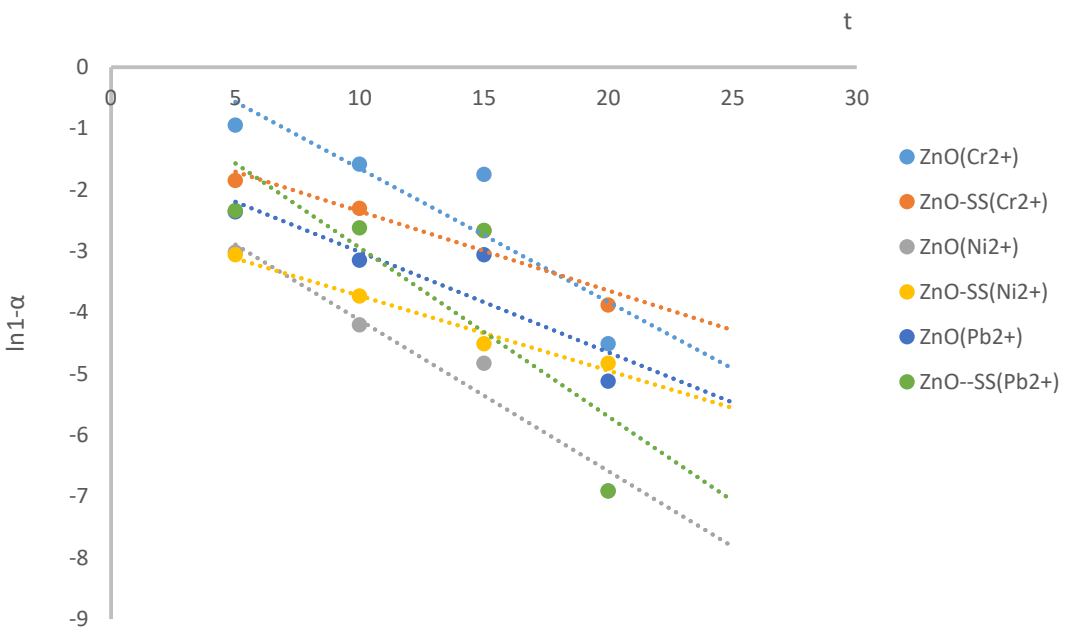

Figure 4.45 b ; Plot of liquid diffusion modell for adsorption of Ni^{2+}, $Cr^{6+}$and Pb^{2+} onto Nanoadsorbents prepared by ZnO and ZnO-SS materials

K_{t1} values as observed from Table 4.12 - are highest under the adsorption of contaminant ions onto MnO and MnO-SS Nano adsorbents, suggesting that they have the highest capacity to adsorb the contaminant ions this work agrees with (Singh and Pant 2006; Chiou and Li 2002:). however, the adsorption capacity of the Nano adsorbents as described by liquid diffusion model decreased in the following order; MnO < MnO-SS < Fe_3O_4 < Fe_3O_4--SS < ZnO < ZnO-SS

4.8.2 Intra- particle Diffusion Model

Intra- particle diffusion model was also adopted to predict the rate controlling step which measures the quantity of contaminant ions that diffused within Fe_3O_4, Fe_4O_3-SS; MnO, MnO-SS and ZnO, ZnO-SS. Nano adsorbents at a specified period of time. From the Intra-particle diffusion model as presented in equation 3.34, a plot of q_t versus $t^{0.5}$ produced a

linear curve with values of K_t as slope and C as intercepts for the contaimnant ion adsorption on various Nano adsorbents. The curves are shown on Figures 4.46a; 4.46b, 4.47a; 4.47b, 4.48a; 4.48b. Figures 4.46a and 4.46b represent the interpretation of Intra- particle diffusion model on adsorption of the contaminant ions on Fe_3O_4 and Fe_3O_4-SS Nano adsorbents, Figures 4.47a; 4.47b and 4.48a; 4.48b represent the contaminant adsorption on MnO, MnO-SS, ZnO, ZnO-SS Nano adsorbents respectively.

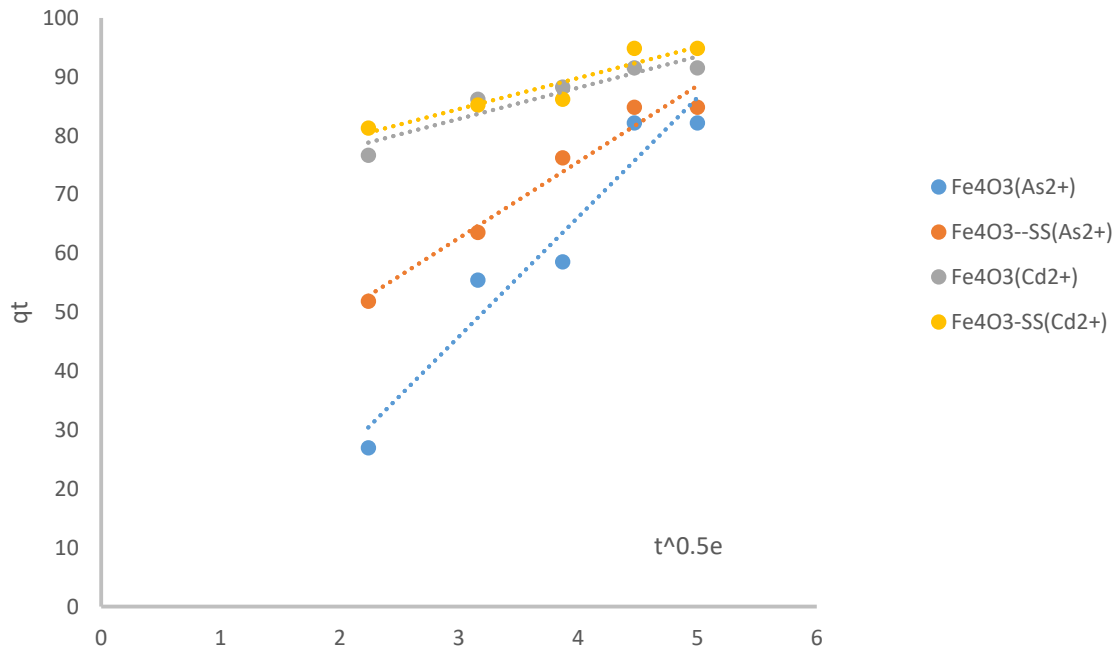

Figure 4.46 a ; Plot of intra-particle diffusion modell for adsorption of As^{3+} and Cd^{6+} onto Nanoadsorbents prepared by Fe_3O_4 and Fe_3O_4-SS materials

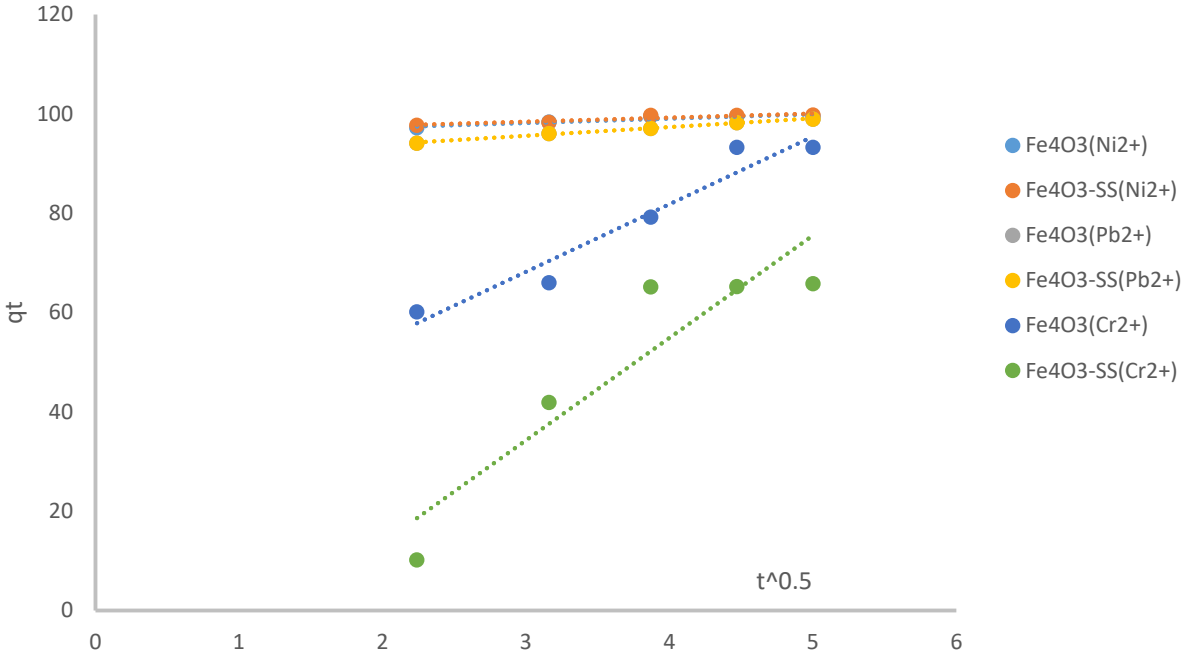

Figure 4.46 b ; Plot of intra-particle diffusion modell for adsorption of Ni^{2+}, Cr^{6+} and Pb^{2+} onto Nanoadsorbents prepared by Fe_3O_4 and Fe_3O_4-SS materials

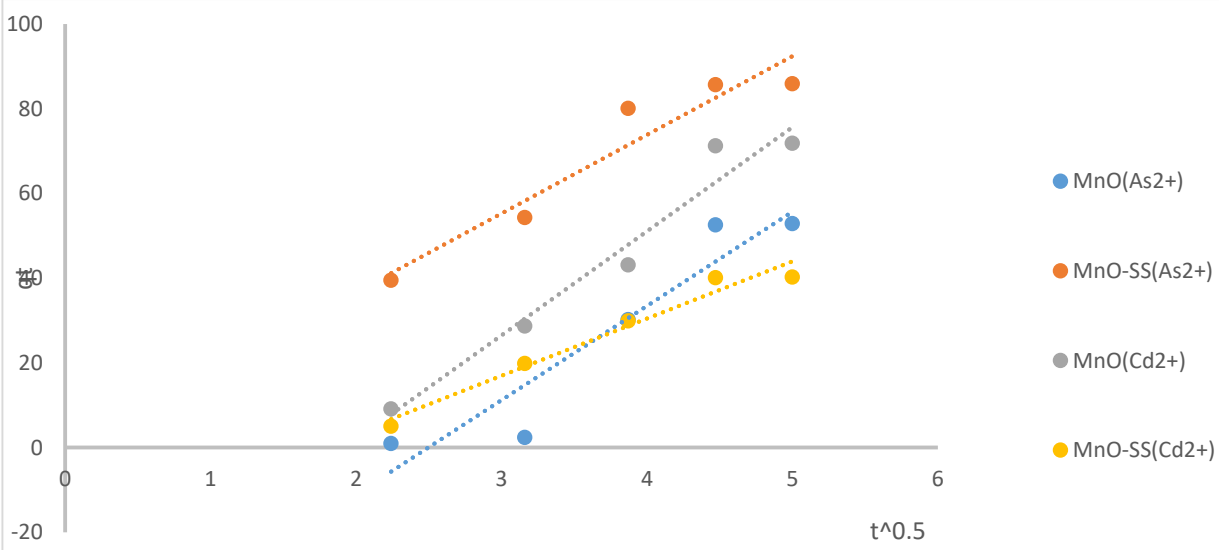

Firure 4.47a ; Plot of intra-particle diffusion modell for adsorption of As^{3+}, and Cd^{2+} onto Nanoadsorbents prepared by Fe_3O_4 and Fe_3O_4-SS materials

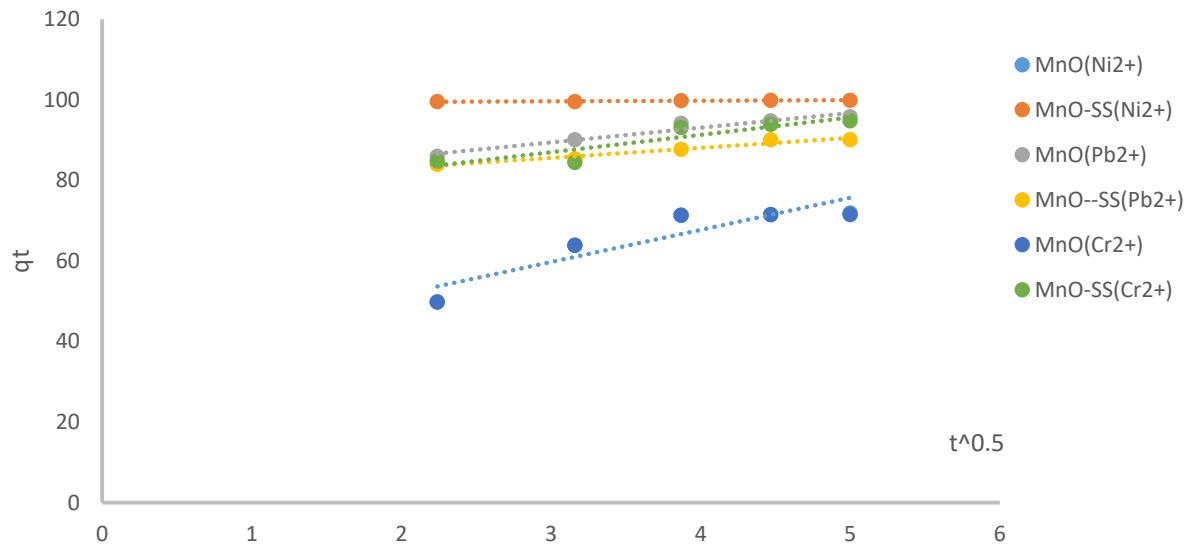

Figure 4.47 b ; Plot of intra-particle diffusion modell for adsorption of Ni^{2+}, Cr^{6+} and Pb^{2+} onto Nanoadsorbents prepared by MnO and MnO-SS materials

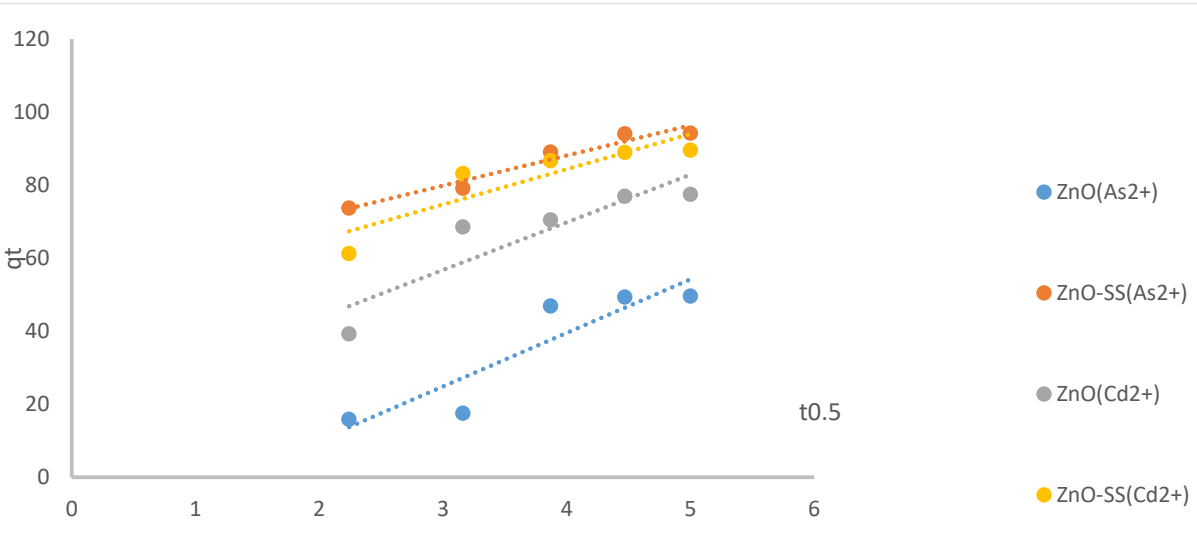

Figure 4.48a ; Plot of intra-particle diffusion modell for adsorption of As^{2+}, and Cd^{2+} onto Nanoadsorbents prepared by ZnO and ZnO-SS materials

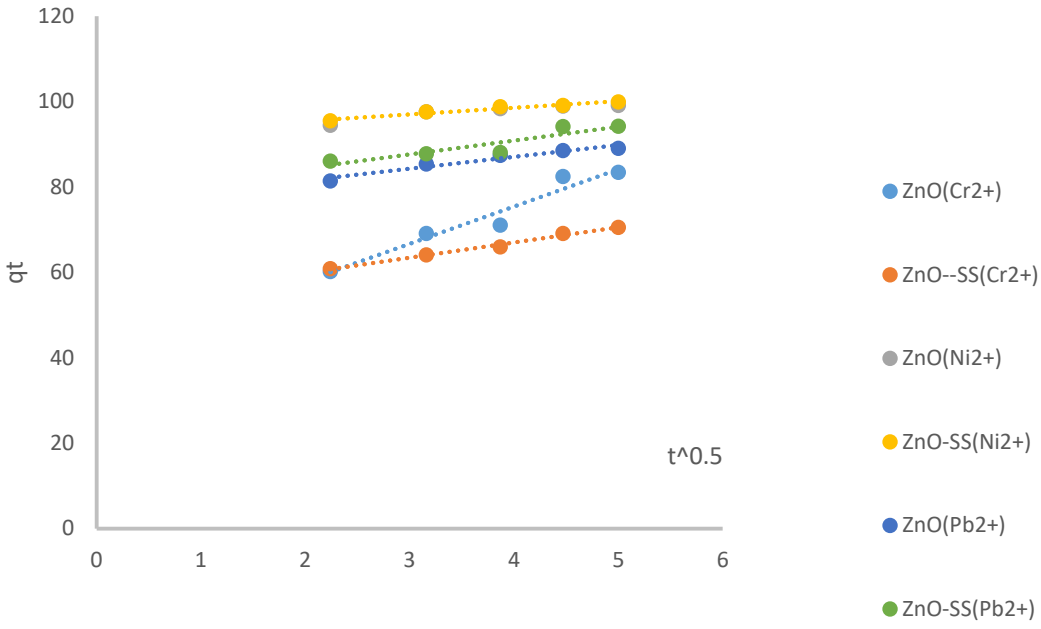

Figure 4.48b ; Plot of intra-particle diffusion modell for adsorption of Ni^{2+}, Cr^{6+} and Pb^{2+} onto Nanoadsorbents prepared by ZnO and ZnO-SS materials

The linear curves display total deviations from the origin which infers that the Intra- particle diffusion model is not the only rate determining step during adsorption of the contaminant ions on various Nano adsorbents as was also observed by Zahoor et al. (2019**)**. This implies that diffusion of the contaminant ions into the Nano adsorbents was not only facilitated by intra-particle diffusion process but liquid film boundary and external particle diffusion mechanism (Oliveira, et al., 2000).

The intra- particle diffusion model parameters, K_{t2} and C are shown on Table 4.13.

Table 4.14 Intra- particle diffusion model parameters for diffusion of the contaminant ions onto various Nano adsorbents

		Fe_3O_4			
	As^{3+}	Cd^{2+}	Cr^{2+}	Ni^{2+}	Pb^{2+}
K_{t2}	20.32	5.31	13.62	0.88	2.57
C	-15.13	66.91	27.32	95.52	84.48
R^2	0.94	0.89	0.94	0.85	0.95
		Fe_3O_4-SS			
K_{t2}	12.95	5.29	20.64	0.83	0.70
C	23.74	68.51	27.65	95.98	93.1
R^2	0.96	0.89	0.85	0.86	0.71
		MnO			
K_{t2}	22.22	24.57	7.86	7.96	3.64
C	55.47	- 47.26	36.15	35.83	78.5
R^2	0.89	0.96	0.82	0.83	0.95
		MnO-SS			

K_{t2}	18.55	13.49	4.31	0.15	3.64
C	- 0.43	- 23.50	74.08	99.17	78.51
R^2	0.92	0.96	0.82	0.8	0.94
			ZnO		
K_{t2}	14.67	13.05	8.73	1.62	2.77
C	- 19.15	17.62	0.50	91.53	75.93
R^2	0.82	0.81	0.94	0.86	0.94
			ZnO-SS		
K_{t2}	8.27	9.65	3.54	1.55	3.24
C	55.06	45.75	52.80	92.31	77.87
R^2	0.95	0.78	0.99	0.96	0.84

Results from the Table above show that the highest K_{t2} value was observed for MnO Nano adsorbents. Previous studies have directly related K_{t2} with adsorbent adsorption capacity (Zahoor et al., 2019; Aseel et al., 2014 and Kilic et al., 2011), it can then be concluded that the MnO Nano adsorbents had the highest adsorption capacity as shown on the present study. As described by the intra- particle diffusion model, the highest adsorption capacity of the Nano adsorbents decreased in this manner; MnO < MnO-SS < Fe_3O_4 < Fe_3O_4-SS < ZnO < ZnO-SS. The lowest adsorption capacity of various Nano adsorbents was observed on adsorption of Ni^{2+} and Pb^{2+} ions. Varying values of C which represent the boundary layer effect of the adsorption process were also observed against the adsorbing contaminant ions and their respective Nano adsorbents. Previous studies have revealed that high C value connotes significant influence of surface adsorption in the rate determining step of adsorption process (Kilic et al., 2011). In the present study, the highest C values were observed in adsorption processes of Ni^{2+} on all the Nano adsorbents, suggesting that surface adsorption controls the adsorption process. it equally means that a significant proportion of Ni^{2+} ion forms a layer at the boundary between the solid and liquid phase as was also recorded in

Uzoije et al. (2015). The surface adsorption control of the contaminant ions adsorption declined as follows; $Ni^{2+} < Pb^{2+} < Cr^{6+} < Cd^{2+} < As^{3+}$

CHAPTER FIVE

CONCLUSION AND RECOMMENDATIONS

5.1 Conclusions

Adsorption processes of As^{3+}, Cd^{2+}, Cr^{6+}, Cd^{2+} and Pb^{2+} contaminant ions through column experiment in which the Nano materials prepared from ordinary (Fe_4O_3, MnO and ZnO) and strach modified (Fe_4O_3-SS, MnO-SS and ZnO-SS) metal oxides as adsorbents have been evaluated. In adsorbent characterization, XRD results confirmed larger particle sizes for the starch modified Nano adsorbents of Fe_3O_4 and MnO than the ordinary Nano adsorbents except ZnO starch modified Nano adsorbent which has smaller particles size. From the Energy dispersive spectroscopy (EDS) findings, Starch modified Nano adsorbents showed more fine-like polycristallite, with larger porous and spongy surface than the ordinary Nano adsorbents. However, ZnO-SS has the largest pore sizes. Strach modified metal oxide Nano adsorbents showed higher adsorption capacity than the ordinary metal oxide Nano adsorbents. FT-IR spectra of all the Nnao adsorbents revealed the presence of O-H, =C-H and -C-H

stretching vibrations. Strach modified metal oxide Nano adsorbents showed higher adsorption capacity than the ordinary metal oxide Nano adsorbents However, ZnO and ZnO-SS showed superior adsorption capacity of the contaminant ions at the optimum adsorption temperature of 70^{o}C, optimum adsorption time of 25mins and optimum initial concentration of 40mg/l but MnO-SS and MnO showed the highest uptake capacity of the contaminant ions at the optimum adsorbent dosage of 0.5g. Langumiur, Fruadlinch and Temki isotherm models tend to fit well with the obtained data but Langumiur isotherm model fit most with all the data. kinetic behaviour of the adsorption processes tested with pseudo first order, Psuedo second order, Elovich adsorption, Ritchie adsorption and Sticking probability Kinetic models revealed reasonably fits with the data but Pseudo second order model fits the data most which suggests that chemisorption process controls the adsorption.

Values of Gibb free energy (ΔG), enthapy of adsorption (ΔH^0) and adsorption entropy (ΔS^0) obtained during the thermodynamic study showed that virtuall all adsorption processes of the contaminant ions onto the nano adsornbents were exothermic and sponteneous with high degree of randomness of the contaminant ions during the processes. Diffusion of the contaminant ions through the liquid film boundary surrounding the Nano adsorbent precedes and predominate the intra-particle diffusion and that the Intra- particle diffusion model is not the only rate determining step. From the findings it can be concluded that ordinary metal oxide Nano adsorbents; Fe_3O_4, MnO and ZnO, significantly remove the As^{3+}, Cd^{2+}, Cr^{6+}, Ni^{2+} and Pb^{2+} ions from water but the starch modified Nano adsorbents; Fe_4O_3-SS, MnO-SS and ZnO-SS proved more efficient.

5.2 Recommendations

It is recommended based upon the results obtained that .

(i) Starch should be incorporated in the synthesis of the metal oxides used as adsorbent since it improves the surface area and enhances greater adsorption.

(ii) The starch modified metal oxide Nano adsorbents (Fe_3O_4-SS MnO-SS and ZnO-SS) adopted in this research work be used at a wider scale in industries for adsorption processes of heavy metals removal.

(iii) The study of the adsorbent morphologies after adsorption and the investigation of possible intraparticle diffusion in the adsorption processes be investigated in further studies since it will help to establish the nature of bonding of the metal ions to the nanoparticles-adsorption.

5.3 Contributions to Knowledge

From the results obtained and recorded in this work, the following contributions have been added to knowledge:

i. Certain nanoparticles such as ZnO, Fe_3O_4 and MuO which were synthesized are useful in the removal of heavy metals from waste water.
ii. Higher adsorbent dose, concentration of efficient, time and pH are effective tools used in understanding the efficiency of heavy metals removal from waste water.
iii. Adsorption Kinetics are useful tools in understanding the effect of temperature, pressure, concentration, nature of adsorbent and time on the removal of the studied heavy metals from waste water.
iv. The models used in this work such as Langmuir, Freundlich and Temkin were able to interpret effectively and verified that the different adsorption Isotherms used were able to give thorough understanding of the adsorbent-adsorbate interactions during the process of removal of heavy metals from waste water.
v. The studied nanoparticles oxides are effective in the removal of heavy metals from waste water.

REFERENCES

Aamir, D. A., Masakazu, K., Thomas, M. Y., & Ian, M. K. (2013). Arsenic removal from water using flame-synthesized iron oxide nanoparticles with variable oxidation

Abhilash, M. (2010). Potential applications of Nanoparticles. International. *Journal of Pharmacy Biological Science*., 1(1).

Abia, A. A., Horsfall, M. & Didi, O. (2003). The use of chemically modified and unmodified cassava waste for removal of Cd, Cu, and Zn ions from Aqueous solution. *Bioresource Technology, 90,* 345-348.

Abolfazl, A., Rogaie R., Soodabeh D., Sang W. J., Nosratollah Z., Younes H., Mohammad S., Mohammad K., & Kazem N., (2013). Liposome: classification, preparation, and Applications. *Nanoscale Research. Letters*., 8: 102.

Adeleh, A., & Hamed, S. (2015). Application of Magnetite (Fe_3O_4) Nanoparticles in Hexavalent Chromium Adsorption from Aquatic Solutions. *Journal of Petroleum and Environmental Biotechnology.*

Ahmed, N. M., & Yousef, N. S., (2015) Synthesis and Characterization of Zinc Oxide Nano particles for the removal of Cr (VI). *International Journal of Scientific & Engineering Research*, (6):

Akgu, M., Karabakan, A., Acar, O. & Yurum, Y. (2006). Removal of silver (I) from aqueous solutions with clinoptilolite. *Microporous and Mesoporous Materials, 94,* 99– 104.

Al-Duaij, O. K. (2018). Efficient and fast removal of cadmium by nanopowder material from aqueous solution. Journal of Optoelectronics and Biomedical Materials, 10(1): 11 – 20

Almaraz, V., Trocellier, P., Da´ vila & Rangel, I. (2003). Adsorption of aqueous Zn(II) species on synthetic zeolites. *Nuclear Instruments and Methods in Physics Research Section, 210*, 424–8

Al-Saad, K. A., Amr, M. A., Hadi, D. T., Arar, R. S., AL-Sulaiti, M. M., Abdulmalik, T. A., Alsahamary, N. M. & Kwak, J. C. (2012). Iron oxide nanoparticles: applicability for heavy metal removal from contaminated water. *Arab Journal of Nuclear Sciences and Applications*, 45 (2): 335-346.

Alvarez-Ayuso, E., Garcia-Sanchez, A., & Querol, X. (2003) Purification of metal electroplating waste waters using zeolites. *Water Research, 37,* 4855-4862.

Amudha M., & Krishna K. S., (2014). Biosynthesis and characterization of silver nanoparticles using the aqueous extract of vitex negundo. linn. *World Journal of Pharmacy. Science*., 3(8): 1385 1393.

Anirudha M., Sudhir C., Garima G., & Avnika T., (2012). Dendrimers: a tool for drug delivery. *Advance in Biological. Research*., 6(4): 165 169

Anusa, R., Ravichandran, C., & Sivakumar, E.K.T., (2017). Removal of heavy metal ions from industrial wastewater by nano-ZnO in presence of electrogenerated Fenton's reagent. *International Journal of Chemical Technology Research,*10:501-508.

Aseel M. Aljeboree, Abbas N. Alshirifi, & Ayad F. (2014). Kinetics and equilibrium study for the adsorption of textile dyes on coconut shell activated carbon; *Arabian Journal of Chemistry 43*. 124-132

Azizi,S., Mahnaz Mahdavi Shahri, M.M., & Mohamad, R (2017). Green Synthesis of Zinc Oxide Nanoparticles for Enhanced Adsorption of Lead Ions from Aqueous Solutions: Equilibrium, Kinetic and Thermodynamic Studies

Babu, B. V. & Gupta, S. (2009a). Removal of Cr(vi) from waste water using activated tamarind seed as an absorbent. *Journal of Environmental Engineering and Sciences, 7*(5): 553-557.

Babu, B. V. & Gupta, S. (2009b). Adsorption of Cr(vi) Using activated neem leaves kinetic studies *Adsorption 14*(1): 85-92

Banerjee, S., & Chattopadhyaya, M.C., (2013). Adsorption characteristics for the removal of a toxic dye tartrazine from aqueous solutions by a low cost agricultural by-product. *Arabian Journal of Chemistry,*

Cabrera, C., Gabaldon, C. & Marzal, P. (2005). Sorption characteristics of heavy metal ions by a natural zeolite. *Journal of Chemical Technology and Biotechnology, 80,* 477-481

Chen, Y., Pan, B., Li, H., Zhang, W., Lv, L. & Wu, L. (2010). Selective removal of Cu (II) ions by using cation-exchange resin-supported polyethyleneimine (PEI) nanoclusters. *Environmental Science and Technology*, 44: 3508-3513.

Chiavola, A., D'Amatoa, E., Stollerb, M., Chianese, A. & Maria Rosaria Bonia, M. R. (2016). Application of Iron Based Nanoparticles as Adsorbents for Arsenic Removal from Water. *Chemical Engineering Transactions,* 47: 325-330.

Chiou M.S, & Li H.Y (2002) Equilibrium and kinetic modeling of adsorption of reactive dye on cross-linked chitosan beads. *J Hazard Mater 93*:233–248.

Cicchella, D., De Vivo, B. Lima, A., Albanese, S., McGill, R. A. R., & Parrish, R. R., (2008). Heavy metal pollution and Pb isotopes in urban soils of Napoli - Italy, Geochemistry: *Exploration, Environment, Analysis, 8,* 103 – 112

Coruh, S. & Ergun, O.N. (2009). Ni2+ removal from aqueous solutions using conditioned clinoptilolites: kinetic and isotherm studies. *Environmental Progress & Sustainable Energy, 28,* 162–172.

Daoush, W. M. (2017). Co-Precipitation and Magnetic Properties of Magnetite Nanoparticles for Potential Biomedical Applications. *Journal of Nanomedicine Research,*5.

Das, N. (2015). Recovery of precious metals through biosorption—a review. *Hydrometallurgy, 103*(1), 180-189.

Dawodu, F. A. Akpomie, G. K., & Ejikeme, P. C. N. (2015). Equilibrium, thermodynamic and kinetic studies on the adsorption of lead (ii) from solution by agbani clay. *Research Journal of Engineering Sciences, 1*(6), 9-17

Durthi, C. P., Rajulapati, S. B., Palliparambi, A. A., Kola, K. A., Shirish H. & Sonawane, H. S. (2018). Studies on removal of arsenic using cellulose acetate–zinc oxide nanoparticle mixed matrix membrane. *International Nano Letters*, 8:201–211.

Egirania, E.D., Poyi, R N., & Wessey, N. (2018). Effect of Zinc Oxide Montmorillonite Composite the Removal of Arsenite, *Journal of Chemistry* 2:(3) 24-35.

Environmental Protection Agency (EPA) (2016). Nickel compounds. Retrieved from EPA United States *Environmental Protection Agency*.

Environmental Protection Agency (EPA, USA). Washington, DC., (1990), Toxicological profile for lead, Syracuse Research Cororation Agency for ToxicSubstances and Disease Registry (ATSDR)

Erdem, E., Karapinar, N. & Donat, R. (2004). The removal of heavy metal cations by natural zeolites. *Journal of colloidal and Interface Science, 280*(2), 309 – 314.

Ghaniem, R., El-Taweil, Y.A., M. E. & Ossman, M.E. (2017). Use of Hydrous Manganese Oxides Nanopowders as a Potential Sorbent for Selective Removal of Nickel Ions from Industrial Wastewater, Kinetics and Isotherm Studies. *American Journal of Chemical Engineering, 4*(6) 170-178.

Gunay, A., Arslankaya, E. & Tosun, I. (2007) Lead removal from aqueous solution by natural and pretreated clinoptilolite: Adsorption equilibrium and kinetics. *Journal of Hazardous Materials, 146*(2), 362 – 371

Habish, A. J. (2017). Influence of synthesis parameters on the properties of the composite adsorbents based on sepiolite and nano-zerovalent iron. *Journal of Doctoral Dissertation*.

Hameed, K.S., Muthirulan, P., & Meenakshi, S.M., (2013). Adsorption of chromotrope dye onto activated carbons obtained from the seeds of various plants: Equilibrium and kinetics studies. *Arabian J. Chem,36*, 342-349

Hanan E. Osman, Reham K. Badwy, & Hanan F. A., (2010). Usage of some agricultural by-products in the removal of some heavy metals from industrial wastewater. *Journal of Phytology, 2*(3): 51–62

He, J., Zhou, T., Young, J.C., Boland, G.J., & Scott, P.M., (2010). Chemical and biological transformations for detoxification of trichothecene mycotoxins in human and animal food chains: a review. *Trend Food Sci. Technol. 21*, 67–76.

Ho, Y. S. (2006). Review of second-order models for adsorption systems. *Journal of hazardous materials, 136*(3), 681-689

Ho, Y.S. & McKay, G. (1999). The sorption of Lead (II) on peat. *Water Research, 33*, 578-584.

Holzwarth, U., & Gibson, N. (2011). The Scherrer equation versus the "Debye – Scherrer equation," (6), 21027.

Inglezakis, V.J., Loizidou, M.D. & Grigoropoulou, H.P. (2002) Equilibrium and kinetic ion exchange studies of Pb2+, Cr3+, Fe3+ and Cu2+ on natural clinoptilolite. *Water Research, 36,* 2784-2792

Isidorov, V. (1997). Introduction to Chemical Eco-toxicology. Saint-Petersburg State University, 54-58.

Jitendra M., Amla B., Abhijeet S. & Madan M. S. (2014). Phyto-fabrication of nanoparticles through plant as nanofactories. *Advance Natural Science Nanoscience Nanotechnology*., 5: 10.

Junsheng L., Linlin, W., & Xinghua, C. (2014), kinetic Model Investigation on lead 11 Adsorption using Silica-based hybrid Membrane. *Journal of Desalination and Water Treatment. 346*. 194

Kakavandi B, Esrafili, A, Mohseni-Bandpi, A., Jonidi Jafari, A., & Rezaei, K. R. (2014). Magnetic Fe_3O_4 nanoparticles as adsorbents for removal of amoxicillin from aqueous solution. *Water Science and Technology*, 69(1):147-55.

Kavitha, K.S., Syed Baker, Rakshith, D., Kavitha, H.U., Yashwantha Rao, H.C., Harini B. P. & Satish, S. (2013). Plants as green source towards synthesis of nanoparticles. International. *Research Journal of Biological. Science*., 2(6): 66 76.

Kilic, M., Apaydin-Varol, E., & Putun, E.A., (2011). Adsorptive removal of phenol from aqueous solutions on activated carbon prepared from tobacco residues: Equilibrium,

Kulkarni, S. J. & Kaware, P. J. (2013). Review on research for removal of phenol from wastewater. International *Journal of Scientific and Research Publications*, 3(4): 1-5.

Kumar, H., Manisha., & Poonam, S. (2013). Synthesis and Characterization of MnO_2 Nanoparticles using Co-precipitation Technique. *International Journal of Chemistry and Chemical Engineering*,3(3): 155-160.

Kumar, S.S. (2012). Chemical Synthesis of Zinc Oxide Nano particles by Precipitation Method. *International Journal of Engineering and Technical Research,*2012.

Lakshmipathy, R. & Sarada N.C. (2015). Metal ion free watermelon (Citrullus lanatus) rind as adsorbent for the removal of lead and copper ions from aqueous solution. *Journal of Desalination and Water Treatment*, 1–11

Langergren, S. & Svenska, B. K. (1898). Zur theorie der sogenannten adsorption geloester stoffe. Veternskapsakad Nandlingar, 24, 1-39.

Largitte, L & pasquier R, (2016), Areview of the kinetic adsorption models and their application to the adsorptiop of lead by an activated carbon. *Journal of Chemica Engineering Research and Desugen 109,* 495

Mark Asta, Susan M. Kauzlarich, Kai Liu, Alexandra Navrotsky, & Frank, E. (2007). Osterloh inorganic nanoparticles unique properties and novel applications

Mehdi V., Asma, O. M., Majid, M. & Nasrin, R. (2013). Investigation of Langmuir, Freundlich and Temkin Adsorption Isotherm of Tramadol by Multi-Wall Carbon Nanotube. *Asian Journal of Chemistry*, 25(10): 5467-5469.

Mohamadiun, M., Dahrazma, B., Saghravani, S. F., & Darban, A. K. (2018). Removal of cadmium from contaminated soil using iron (iii) oxide nanoparticles stabilized with polyacrylic acid. *Journal of Environmental Engineering and Landscape Management*, 26(2): 98–106.

Mohan, D., & Pittman, C. U., (2006). Activated carbons and low cost adsorbents for remediation of tri- and hexavalent chromium from water, *Journal of Hazardous Materials, 137*, 762 – 811

Motsi, T., Rowson, N.A. & Simmons, M.J.H. (2009) Adsorption of heavy metals from acid mine drainage by natural zeolite. *International Journal of Mineral Processing, 92*, 42–48.

Muhammad Z., & Farhat A. K (2018). Adsorption of aflatoxin B1 on magnetic carbon nanocomposites prepared from bagasse; *Arabian Journal of Chemistry 11*, 729–738

Nagavarma, B.V.N., Hemant, K.S., Yadav, Ayaz, Vasudh, L.S., & Shivakumar, H.G. (2012). Different techniques for preparation of polymeric nanoparticles Asian *Journal of Pharmaceutical. Clinical. Research.*, 5(3): 16 23.

Nagendran S. & Noor S. S. (2015). Dye adsorbent by pineapple activated carbon: H_3PO_4 and NaOH Activation; arpn *Journal of Engineering and Applied sciences. 10*(20), november, issn 1819-6608

Naja, G. M., & Volesky, B., (2009). Toxicity and sources of Pb, Cd, Hg, Cr, As,, and Radionuclides in the environment, chapter 2 in Wang, L. K., Chen, J. P., Hung, Y

Nayar, R. (2019). Removal of Toxic Cation from Aqueous E-Waste Material using ZnO as a Nanoadsorbent by Adsorption Technique. *Journal of Current Chemical and Pharmaceutical Sciences Research*, 9(1): 119

Oliveira, L.C.A., Rios, R.A., Fabris, J.D., Garg, V., Sapag, K., & Lago, R.M., (2000). Activated carbon/iron oxide magnetic composites for adsorption of contaminants in water. *Carbon 40*, 2177–2183.

Oren, A.H. & Kaya, A. (2006) Factors affecting adsorption characteristics of Zn2+ on two natural zeolites. *Journal of Hazardous Materials,13*, 59–65.

Ozacar, M. & Sengil, I.A. (2005). A kinetic study of metal complex dye sorption onto pine sawdust. *Process Biochemistry, 40*, 565-572.

Papageorgiou, K.S., Katsaros, K.F., Kouvelos, P.E., Nolan, W.J., LeDeit, H. & Kanellopoulos, K.N. (2006). Heavy metal sorption by calcium alginate beads from Laminaria digitata. *Journal of Hazardous Materials, B137*, 1765 – 1772.

Patterson, J.W. (1987). Metal Speciation Separation and Recovery, Chelsea: Lewis Publishers.

Peric, J., Trgo, M. & Medvidovic, N.V. (2006). Removal of zinc, copper and lead by natural zeolite-a comparison of adsorption isotherms. *Water Research, 38*, 1893-1899.

Prasad, M., Xu, H.Y. & Saxena, S. (2008) Multi-component sorption of Pb(II), Cu(II) and Zn(II) onto low-cost mineral adsorbent. *Journal of Hazardous Materials,154*, 221-229.

Qu, X., P., Alvarez, P. J. J., & Li, Q. (2013). Applications of nanotechnology in water and wastewater treatment. *Water Research*, 47: 3931–3946.

Rahmawati, R., Taufiq, A., Sunaryono, S., Fuad, A., Yuliarto, B., S. Suyatman,S., & Kurniadi,D. (2017) Synthesis of Magnetite (Fe_3O_4) Nanoparticles from Iron sands by Co-precipitation-Ultrasonic Irradiation Methods. *Journal of Materials and Environmental Sciences*9:155-160.

Richardson, J.F. & Harker, J.H. (2002). Coulson and Richardson's chemical Engineering, 5 th ed. Butterworth-Heinemann: Oxford.

Sabri, A. & Tuzen, M. (2008). Biosorption of cadmium(ii) from aqueous solution by red algae (*Ceramiumvirgatum*): Equilibrium, kinetic and thermodynamic studies. *Journal of Hazardous Materials*, 157: 448-454.

Sadeghi, M., Irandoust, M., Khorshidi, F., Feyzi, M., Jafari, F., Shojaeimehr, T., & Shamsipur, M., (2017). Removal of Arsenic (III) from natural contaminated water using magnetic nanocomposite: kinetics and isotherm studies,

Shakeel, A., Hasanaina, S.K., Nasia, A., & M. Nadeem (2001). Synthesis of Fe_2O_3 nanoparticles by new Sol-Gel method and their structural and magnetic characterizations

Shaoyou, L., Dingze, H., Zongyi M. & Yunguo, L. (2014). Synthesis of calcium doped TiO2 nanomaterials and their visible light degradation property. *International Conference on Material and Environmental Engineering*, 43-47.

Shi, Y., Kong, X., Zhang, C., Chen, Y., & Hua, Y., (2013). Adsorption of soy isoflavones by activated carbon: kinetics, thermodynamics and influence of soy oligosaccharides. Chem. Eng. J. 215–216, 113–121.

Shobha, G., Vinutha Moses, & Ananda, S. (2014). Biological Synthesis of Copper Nanoparticles and its impact. *International Journal of Pharmaceutical Science*. Inventions., 3(8): 6, 28, 38.

Sikder M.T., Mihara Y., Islam M.S., Saito T., Tanaka S., & Kurasaki M., (2014). Preparation and characterization of chitosan-carboxymethyl-β-cyclodextrin entrapped nanozero-valent iron composite for Cu (II) and Cr (IV) removal from wastewater. *Chemical Engineering Journal*, 236: 378-387.

Sing, K. K., Talat, M. & Hasan, S. H. (2006). Removal of lead from aqueous solutions by agricultural waste maize bran, *Bioresourse Technology, 21*, 24-2130.

Singh T.S, & Pant K.K, (2006). Kinetics and mass transfer studies on the adsorption of arsenic onto activated alumina and iron oxide impregnated activated alumina. *Water Qual Res J Can, 41*:147–156

Singh, V. K., Mohan, D., Rajputa, S. Steele, P. H., & Pittman, C. U., (2011), Modeling and evaluation of chromium remediation from water using low cost bio-char, a green adsorbent, *Journal of Hazardous Materials, 188,* 319 – 333

Sobhy M (2014), Yakout Removal of the hazardous, volatile, and organic compound benzene from aqueous solution using phosphoric acid activated carbon from rice husk Yakout. *Chemistry Central Journal 8*(52), 2 of 7

Taman R., Ossman M.E., Mansour M.S., & Farag H.A., (2015). Metal Oxide Nanoparticles as an Adsorbent for Removal of Heavy Metals. *Journal of Advanced Chemical Engineering*

Teh, C. Y., Wu, T. Y. & Juan, J. C. (2014). Potential use of rice starch in coagulation-flocculation process of Agro-industrial wastewater: Treatment performance and flocs characterization. *Ecology and Engineering*, 71: 509–519.

Temkin, M.I. & Pyzhev, V. (1940). Kinetics of ammonia synthesis on promoted iron catalyst. *Acta Physiochemical USSR, 12*. 327-356

Thackston, E. L., Wilson, D. J., Hanson, J. S. & Miller, D, L. (1980). Lead removal with adsorbing colloid floatation. *Journal Water Pollution Control Federation, 328*

Tien, C. (1994). *Adsorption calculations and modelling. Butterworth* – Heinemann: New York.

Tseng, R.L. (2006). Mesopore control of high surface area NaOH-activated carbon. *Journal of Colloid and Interface Science, 303,* 494-502

Uzoije, A. P., Pascal A. P, Njoku C., Atu Ayuk A., Justus I. & Okolie (2015). Equilibrium, Thermodynamic and Kinetic Studies on Adsorption of Zinc (II) From Solutions Using Different Low-Cost Adsorbents. *American Journal of Chemistry and Applications, 2*(6): 129-140

Wang, J. & Chen, C. (2009). Biosorbents for heavy metals removal and their future. *Biotechnology Advances,* 195–226.

Wang, J., & Chen, C. (2014). Chitosan-based biosorbents: modification and application for biosorption of heavy metals and radionuclides. *Bioresource technology, 160*, 129-141.

Wang, L., & & Wang, A. (2007). Adsorption characteristics of Congo Red onto the chitosan/montmorillonite nanocomposite. *Journal of hazardous materials, 147*(3), 979-985

Wang, S., Zhu, Z.H., Coomes, A. Haghseresht, F. & Lu, G.Q. (2005). The physical and surface chemical characteristics of activated carbons and the adsorption of Methylene blue from waste water. *Journal of Colloid and Interface Science, 284*, 440- 446.

Wasewar K.L, Mohammad A, Prasad B & Mishra I.M. (2008a) Adsorption of Zn using factory tea waste: kinetics, equilibrium and thermodynamics. CLEAN: *Soil, Water, Air; 36*(3): 320-329.

Wu, F.C. & Tseng, R.L. (2006). Preparation of highly porous carbon from fir wood by KOH etching and CO2 gasification for adsorption of dyes and phenols from water. *Journal of Colloid and Interface Science, 294*, 21-30

Yoshiki, O. & Yuta H. (2007). Calculation of the sticking probability of a water molecule to a water cluster. *Earozora kenkyu, 22*(2), 147-151

Zahoora, M., Ullaha, A & Alam, S. (2019). Removal of Enrofloxacin from Water through Magnetic Nanocomposites Prepared from Pineapple Waste Biomass Surface. *Engineering and Applied Electrochemistry, 55*(5), 536–547.

Zakiyyu, I. T., Mohd, K. M., Saliza, A., & Khairunnadim, A. S. (2019). Preparation and Characterization of Magnetite (Fe_3O_4) nanoparticles by Sol-Gel Method. *International Journal of Nano-electronics and Materials* 12: 37-46.

Zhang, X., Lin S, Lu X. Q., Cof P. F. (2011). Removal of Pb (II) from water using synthesized kaolin supported nanoscale zero-valent iron. Removal of Pb (II) from Water Using Synthesized *Kaolin Supported Nanoscale Zero-Valent Iron, 163*(3):243–8.

Zhang, M., Zhang, Y., & Helleur, R. (2016). Selective adsorption of Ag+ by ion-imprinted O-carboxymethyl chitosan beads grafted with thiourea–glutaraldehyde. *Chemical Engineering Journal, 264*, 56-65

APPENDICES

NOMENCLATURE

SYMBOL		DETAILS
As (III)	-	Trivalent Arsenic ion
Cd (II)	-	Divalent Cadmium ion
Ce	-	Final metal ion concentration in liquid phase (mg mL^{-1})
Co	-	Initial metal ion concentration in liquid phase (mg mL^{-1})
Cr (VI)	-	Hexavalent Chromium ion
E	-	Equilibrium conditions
EDS	-	Energy Dispersive Spectroscopy
Fe (III)	-	Trivalent iron ion
Fe (II)	-	Divalent iron ion
Fe_3O_4	-	Magnetite nano particles
Fe_3O_4+SS	-	Starch Stabilized Magnetite nanoparticle
FTIR	-	Fourier Transform Infra-red
K_1	-	Pseudo-first order Kinetic Constant
K_2	-	Pseudo-second order Kinetic Constant
K_f	-	Freundlich constant
L	-	Langmuir constant
MnO + SS	-	Starch Stabilized Zinc Oxide nanoparticle
MnO	-	Manganese Oxide nanoparticles
NaOH	-	sodium hydroxide
N_f	-	Heterogeneity factor
Ni (II)	-	Divalent nickel ion
O	-	Initial conditions
Pb (II)	-	Divalent lead ion
Q_e	-	Solid phase concentration of metal ion on the adsorbent (mg g^{-1})
Q_{exp}	-	Experimental Adsorption Capacity (mg g^{-1})
Qm	-	Maximum amount at metal adsorbed on the adsorbent surface (mg g^{-1})
Q_t	-	Solid phase concentration in time, t, by the adsorbent (mg g^{-1})
R^2	-	Regression correlation coefficient

R_L	-	Dimensionless equilibrium parameter
SEM	-	Scanning Electron Microscope
T	-	Evaluated at time t
V	-	Initial Volume of Metal Solution (L)
W	-	Weight of the adsorbent (g)
WHO	-	World Health Organization
XRD	-	X-Ray Diffraction